DEVELOPMENT OF HIGH RESOLUTION SYSTEM FOR STELLAR IMAGING

(Corrected Copy)

A Thesis

Submitted for the Degree of

Doctor of Philosophy (Technology)

Submitted by

SREEKANTH REDDY V

Department of Applied Optics & Photonics

University College of Technology

University of Calcutta

January 2021

To my Family,

Friends and Teachers...

List of Publications

1. Refereed Journal Articles

(a) **Measurements of atmospheric turbulence parameters at Vainu Bappu Observatory using short-exposure CCD images** - ***Sreekanth Reddy V****, Ravinder Kumar Banyal, R. Sridharan, Aishwarya Selvaraj*, Research in Astronomy and Astrophysics,vol. 19, 74-84, (2019)[1].

(b) **Development of image motion compensation system for 1.3 m telescope at Vainu Bappu Observatory** - ***Sreekanth Reddy V****, Ravinder Kumar Banyal, R. Sridharan, P.U. Kamath and Aishwarya Selvaraj*, Research in Astronomy and Astrophysics,vol. 20, 12-22 , (2020)[2].

2. Refereed Conference Proceedings

(a) **Development and performance analysis of adaptive optics system in laboratory** - ***Sreekanth Reddy V****, Ravinder Kumar Banyal, Suresh Venkata, Chinmaya V S, Sridharan R*, Proc. OSI, International conference on advances in optics and photonics, ISBN: 978-93-84871-109, 120-126, (2017).

(b) **Calibration of Phase Plate and Deformable Mirror for Adaptive Optics System** - *Venkata Suresh Narra,* ***Sreekanth Reddy V****, Ravinder Kumar Banyal, B Raghavendra Prasad*,Proc. OSI, International conference on advances in optics and photonics, ISBN: 978-93-84871-109, 212-220, (2017).

[1]Presented in Chapter 2
[2]Presented in Chapter 3,4,5

Presentations

1. **Estimation of Atmospheric Turbulence Parameters using Short Exposure Images with 1.3m Telescope at Kavalur-** ***Sreekanth Reddy V****, Ravinder Kumar Banyal, R. Sridharan, Anbazhagan* , 34th ASI Meeting,2016, University of Srinagar, India, **Poster presentation**.

2. **Optical design and performance modelling of an adaptive optics module for 1.3m JCB telescope-Sreekanth Reddy V**, Ravinder Kumar Banyal, R. Sridharan, 40th Optical Soceity of India meeting,University of Tezpur,2016, India, **Oral presentation**.

3. **Development and performance testing of tip-tilt adaptive optics -** ***Sreekanth Reddy V****, Ravinder Kumar Banyal, R. Sridharan*, International topical meeting on applied and adaptive optics,2017, Indian institute of science and technology, India, **Poster presentation**.

4. **Development and performance analysis of adaptive optics system in laboratory-** ***Sreekanth Reddy V****, Ravinder Kumar Banyal, Suresh Venkata, Chinmaya V S, Sridharan R*, 41st Optical Soceity of India meeting,2017, Guru Jambheshwar University of Science and Technology, India, **Oral presentation**.

5. **Development and on-sky testing of tip-tilt adaptive optics system-** ***Sreekanth Reddy V****, Ravinder Kumar Banyal, Sridharan R*, Network of Young Researchers in Astronomical Instrumentation (NYRIA),2018, Leiden, The Netherlands, **Oral presentation**.

6. **Development and on-sky performance analysis of tip-tilt adaptive optics system-** ***Sreekanth Reddy V****, Ravinder Kumar Banyal, Sridharan R*, 37th ASI Meeting,2019, Christ University, Bangalore India, **Oral presentation**.

Abstract

Adaptive Optics (AO) technology is a part of ground-based astronomical observatories around the world. It enables the telescopes to attain near diffraction-limited resolution. We have designed, developed and tested a tip-tilt image motion compensation system for 1.3m J.C. Bhattacharya (JCB) telescope at Kavalur. This thesis includes the measurement of turbulence parameters, design development and demonstration of a tip-tilt instrument on 1.3 m telescope at Vainu Bappu Observatory, Kavalur.

Measurement of atmospheric turbulence parameters on site of the telescope is essential prior to the development of an AO system. The atmospheric turbulence parameters namely, atmospheric seeing, the tilt-anisoplanatic angle (θ_0) and the coherence time (τ_0), were measured under various sky conditions, at Vainu Bappu Observatory in Kavalur. Bursts of short exposure images of selected stars were recorded with a high-speed, frame-transfer CCD mounted on the Cassegrain focus of a newly commissioned 1.3 m JCB telescope. The estimated median seeing is $\approx 1.85''$ at wavelength of ~ 600 nm, the image motion correlation between different pairs of stars is $\sim 44\%$ for $\theta_0 \approx 36''$ and mean τ_0 is ≈ 2.4 ms.

The optical model of the instrument was designed in ZEMAX ray-tracing software. The diffraction-limited field of view (FOV) of the instrument is $1' \times 1'$ with a wavelength range of 0.48 - 0.7 μm. A telescope interface unit was designed in *AutoCAD* and fabricated to house all the sub-components of the system. Control software with graphical user interface was developed in LabView software. In closed-loop operation the control software can operate at loop frequency up to 300 Hz. To characterize its performance, the instrument was thoroughly tested in the laboratory by simulating the image motion data obtained the telescope.

The instrument was commissioned on the telescope to analyze its performance in real-time. The tilt corrected images have shown up to $\approx 57\%$ improvement in image resolution and corresponding peak intensity increased by a factor of ≈ 2.8. A closed-loop correction bandwidth of ≈ 26 Hz has been achieved with on-sky tests and the *root mean square* motion of the star image

has been reduced by a factor of ~ 14. These results are not only consistent with theoretical and numerical predictions of image quality improvement expected from a real-time control system but also consistent with the reports of performance of similar systems elsewhere in the world.

Contents

List of Figures

List of Tables

Chapter 1

Introduction

1.1 Atmospheric turbulence

The invention of a telescope in the early 1600s marked the beginning of the modern astronomy. Galileo's original telescope was a simple plano-convex objective lens of diameter 3.7 cm. In last 400+ years the number, size and the complexity of the optical telescopes have seen a gradual increase. At the turn of the 21st century, several 8-10m class telescopes have been successfully built and operated. The objective of the large size telescopes is to improve the resolution of the image and observe fainer objects in the far flung corners of the universe. Large telescopes would help to see faint targets by collecting more light. However, the atmospheric turbulence poses a severe hindrance to the performance of the ground-based telescopes. The spatial and temporal variations in temperature of the Earths atmosphere change its density; hence, its refractive index. The small changes in the refractive index of different layers have a cumulative effect on the refractive index profile of the atmospheric column. The temperature gradient at different altitudes also randomizes wind velocities.

The light wavefront from distant astronomical objects propagates through different layers of atmosphere. The spatial and temporal changes in refrac-

tive indices in the atmosphere induce distortions in the wavefront (Roddier 1981b). The turbulence in the atmosphere, therefore, degrades the ground-based astronomical imaging. The random interference among the distorted wavefronts is also responsible for twinkling in the stars! The angle of arrival fluctuations due to the changes in the refractive index causes a random motion in the image at the focal plane of a telescope, thus impairing the image resolution.

The effect of atmospheric turbulence on astronomical observations was investigated by Fried (1965, 1966) by relating the statistics of wave distortion to optical resolution. The extensive research on the effect of atmospheric studies shows that the quality of imaging through turbulence is limited by atmospheric seeing λ/r_0, irrespective of optical system resolution λ/D, where r_0 is Fried parameter (coherence length), and D is the aperture diameter. The r_0 is a parameter that quantifies the effect of the atmospheric coherence length for astronomical imaging. The value of r_0 lies within the inertial range ($l_0 < r_0 < L_0$) of the turbulent atmosphere (Buscher et al. 1995; Quirrenbach 2006). This inertial range is the size of the eddies of the atmosphere. These eddies are characterized as small size (l_0) and large size (L_0) based on their nature and scale of energy dissipation. Typically, the inertial range lies between the few millimetres for l_0 to 10s of metres for L_0 (Conan et al. 2000; Davis et al. 1995). The statistical evidence shows that the r_0 falls well within this inertial range for ground-based astronomical observations. The wavefront within the scale of r_0 has negligible phase variations. Beyond the size of r_0, the wavefront is distorted and image quality degrades.

1.1.1 Resolving power of ground-based telescope

The resolving power of a telescope was defined as the integral of its optical transfer function (Quirrenbach 2006). The diffraction-limited resolving power (R_{Tel}) of the telescope is proportional to the square of the size (D^2) of primary aperture (Quirrenbach 2006). The larger telescopes, reduce the angular size

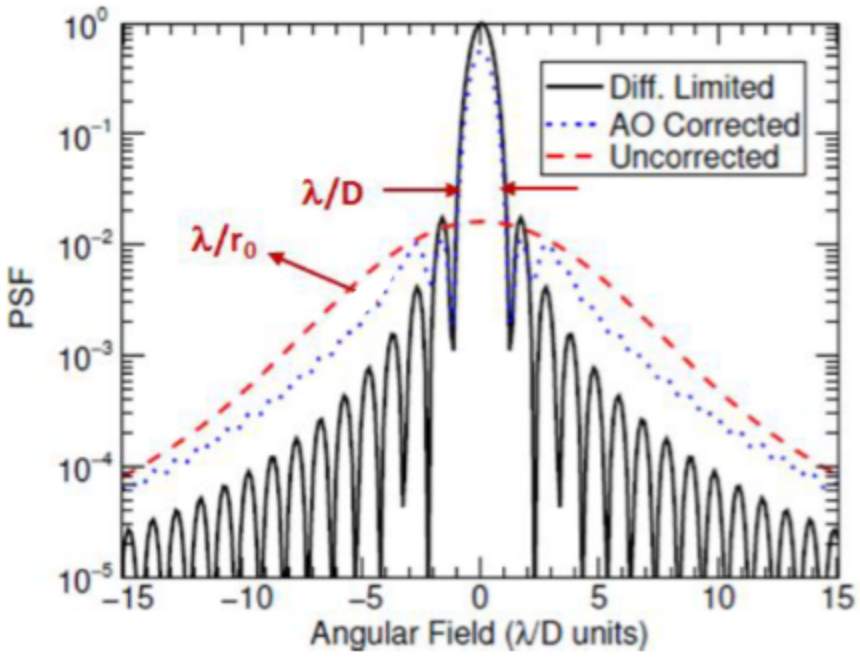

Figure 1.1: Comparison of point spread function (psf) under different observing conditions for a telescope of diameter D and seeing r_0 (Rimmele and Marino 2011).

of the image, so, the sensitivity (peak intensity) increases as D^4 (Hardy 1998; Tyson 1998). Because of atmospheric turbulence, the performance of a telescope, in terms of resolving power, is degraded by r_0^2/D^2 times and the peak intensity reduces by r_0^4/D^4. For example, with D/r_0 of two, the angular resolution of the image is degraded by twice, the resolving power of a telescope fall by four times and the peak intensity of the image falls by 16 times.

For optimal utilisation of the telescopes, the image resolution needs to be improved by correcting distorted wavefront. The adaptive optics system senses and remove the distortions in the wavefront by correcting it in real-time. Therefore, AO is a technical solution to enhance the performance of telescope for astronomical imaging.

1.2 Adaptive optics

Horace Babcock had initially conceptualized the technique of adaptive optics in the year 1953 (Babcock 1953). He described a system of wavefront sensor and a corrector for compensating for atmospheric seeing. Based on this invention, USA Navy had corrected a distorted optical wavefront by using adaptive optics technology in the early 1960s (Greenwood 1977). But, the enormous potential of AO technology was realized in the field of astronomy. In late 1980s astronomers built a 19 actuator AO system for European Southern Observatory at La Silla, Chile (Rousset et al. 1990). It created optimism for improving the efficiency of ground-based telescopes. Since then several telescopes have been equipped with AO systems, making the telescopes highly productive and serving the astronomical community better.

1.2.1 Concept of adaptive optics

The AO system corrects the distorted wavefront by reshaping it with a deformable mirror driven by hundreds of actuators. The wavefront is sensed and corrected for tens to hundreds of times per second. Figure 1.1 illustrates the shape of telescope PSF under different observing conditions. For a diffraction-limited PSF, the core has more than 85% of starlight within $\sim \lambda/D$ width and very little outside. For the seeing limited case (uncorrected) most of the light spreads outside the core to broaden the PSF to an angular size of $\sim \lambda/r_0$, where D is telescope diameter, and r_0 is seeing parameter at wavelength λ. The task of the AO system is to pull the radiative energy from the broadened PSF (wings) back to the central core to restore the diffraction-limited core. The AO corrected PSF closely resembles the PSF of an aberration-free telescope.

The conceptual layout of a typical natural guide star AO (NGSAO) system is shown in Figure 1.2. The main components of the AO system are: a) the wavefront sensor consisting of a lenslet array and a high speed imaging

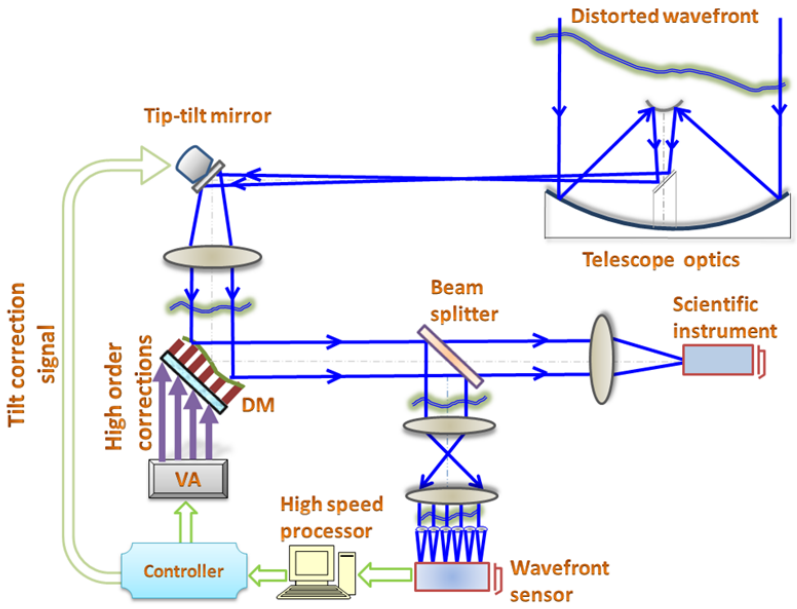

Figure 1.2: Conceptual layout of a natural guide star adaptive optics system. The telescope primary mirror collects the light from a bright star. A beam splitter divides the starlight into two beams -one for wavefront sensing and other for science. The high-speed processor measures the distortions in the wavefront. The tip-tilt mirror corrects the low order distortions, and the deformable mirror corrects high order distortions. The corrected wavefront is directed to science instrument.

camera, b) the AO controller which analyze the wavefront sensor data to compute the wavefront aberrations and c) the correcting elements, namely, the multi-actuator deformable mirror for correcting high order aberrations and two-axis tip-tilt mirror for correcting the low-order component, i.e. the image motion. The main drawback of NGSAO is limited sky coverage due to non-availability of a bright reference star close the science target. Therefore, modern observatories are equipped with more sophisticated versions of AO systems. For example, laser guide stars are used to increase the AO sky coverage, and extreme AO is for high contrast imaging, ground layer and multi-conjugate is used for AO correction over a wider sky (Beckers 1988; Fugate et al. 1994; Jovanovic et al. 2015).

In 2003, Close et al. (2003) have presented scientific results with AO in operation at Multi Mirror Telescope (MMT), Arizona. Figure 1.3 shows

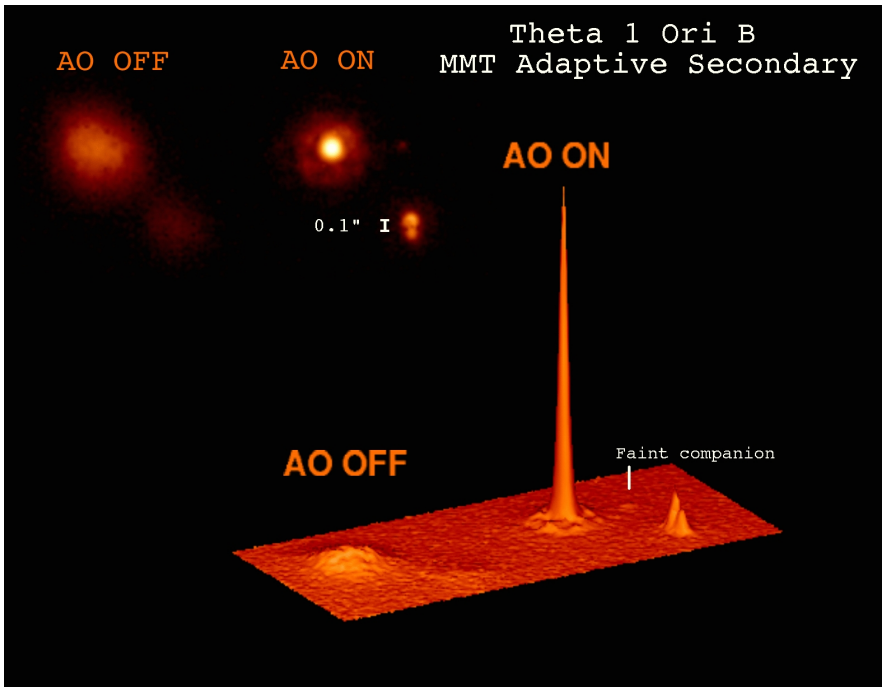

Figure 1.3: Illustration: Comparison of AO corrected and uncorrected image(Close et al. 2003) of Trapezium Ori cluster members.

the image of Trapezium Ori cluster members observed in infrared band of wavelength. It was reported that the angular resolution of the images was improved by a factor of 5.8.

1.2.2 AO for high resolution imaging

Adaptive optics system offer potential advantage for nearly all types of astronomical observations. It has a contribution in spectroscopic, photometric observations and even role in space-based telescopes (Ge et al. 1998; Jung et al. 2007). In spectrography, the starlight needs to be concentrated within a small slit width of few microns. The adaptive optics systems improve the flux density by correcting a distorted wavefront in real-time. It reduces the integration time on the spectrograph and further enables the observations of relatively fainter targets. In photometric observations, the adaptive optics reduces the angular size of an image and increases its resolution. It allows to image fainter targets, improves the detection capability of exoplanets using

coronagraphic technique (Golimowski et al. 1992; Macintosh et al. 2007). In spaced based telescopes, the problem of image degradation due to thermal variations in optics can be adequately addressed by using AO systems. Thus adaptive optics systems have tremendous applications in astronomy.

1.2.3 Image motion compensation with tip-tilt correction

The wavefront distortions are attributed to the order of aberrations which are distributed over spatial frequencies (Noll 1976). The lowest order of these distortions are the tip and tilts along two orthogonal axes. They cause global tilt in the wavefront that reflects in image shift at the focal plane. Hereafter, the *low-order* means the tilt induced aberrations; otherwise, it is *high-order*.

As shown in the Figure 1.2, the AO has a two-step operation of correction. In the first step, the system corrects the global tilt, and in the second step, it corrects the local distortions of the wavefront. The system performs the whole operation in real-time. The global tilt is dominant among the aberration profile of the wavefront. A significant amount of correction could be achieved with the correction of the global tilt.

The turbulence-induced wavefront distortions are often spread over different spatial scales. The study by Noll (1976) expressed these distortions using Zernike polynomials representing a varying degree of aberrations. These polynomials are widely used to evaluate optical system performance. The same was used by Noll (1976) to estimate the effect of atmospheric turbulence on the wavefront. From these investigations, it became clear that the effect of wavefront distortions scales with the size of the system aperture: larger the telescope, stronger the detrimental effect of the higher-order distortions. The image motion, being the lowest order aberration, is primarily caused by the global tilt in the wavefront -sometimes also called the angle of arrival fluctuations. The contribution of the lowest order distortions is about 87% of the wavefront phase variance (Dainty et al. 1998; Fried 1965). By eliminating

the image motion using a real-time tip-tilt system, the image resolution can be significantly improved -at least for small aperture diameters.

The utility of image motion compensation system is well proven with several telescopes equipped with functional tip-tilt instruments. These instruments are relatively simple to design and comparably cost-effective. Close and McCarthy (1994) have developed a secondary mirror-based tip-tilt instrument. In this case, the secondary mirror of the telescope is mounted on a tip-tilt stage to steer the light beam to correct it for an angle of arrival fluctuations. Glindemann (1997) has developed a tip-tilt instrument for CFH telescope to improve the performance of the telescope. They reported an improvement in angular resolution by a factor of 2.3. This significant improvement in the image resolution, allowed to observe relatively fainter targets by using the tip-tilt instrument on-board. Similarly, Golimowski et al. (1992) have efficiently exploited the contribution of the tip-tilt instrument by observing a two magnitude fainter objects for their coronagraphy based exoplanet detection experiment. Olivier and Gavel (1994) have noticed that a tilt compensation system alone can account for a considerable amount of performance gain (a factor of 1.5 in V band).

From these earlier experiments, it is realized that the tip-tilt system has the potential to improve the optimal utilization of the telescope. Thus, we develop a tip-tilt instrument as a first step towards achieving the objective of a full-fledged adaptive optics system for telescope.

The tip-tilt instruments have an image motion sensor or a global tilt sensor for detecting an angle of arrival fluctuations. These fluctuations are corrected by using a tip-tilt mirror mounted on a two-axis system with orthogonal orientation. The control operation continuously tracks the image motion and eliminates it by making appropriate corrections in real-time. For effective correction, this control operation functions at a far higher rate ($\sim$300-500 Hz) in a closed loop.

1.2.4 AO development in India

Apart from Indian Institute of Astrophysics (IIA), a few other institutes, e.g, Udaipur Solar observatory (Bayanna et al. 2008) and Inter-University Center for Astronomy and Astrophysics (Paul et al. 2019) have initiated programs to develop AO systems for astronomy applications. These programs are at different stages of implementation. During the initial phase, research activities focused on the acquisition of technology related to various subsystems, namely, wavefront sensors, reconstruction techniques and wavefront corrector (Roopashree et al. 2013; Vyas et al. 2010). Gradually, as the programs attain maturity, attempts are being made to go beyond the laboratory demonstrations to on-telescope realization. At IIA, low-order tip-tilt has already been successfully demonstrated for solar observatory in Kodaikanal and for stellar case in Kavalur.

1.3 Motivation and scope of the thesis

Indian Institute of Astrophysics is a premier institute in astrophysical research in India. The institute is involved in several national and international projects on development of large astronomical telescopes. It has successfully commissioned several telescopes at different field stations, e.g., Kavalur, Hanle and Kodaikanal for stellar as well as solar research. These facilities have been contributing significantly towards astronomical research in India.

While the efforts to build new and bigger facilities are underway, it has been realized that low-cost upgrades and new science instruments can significantly improve the scientific output and performance of the existing telescopes. The AO technology is one such add-on that can enhance the overall utilization and productivity of a telescope. The thesis work presented here is a first attempt towards building a functional AO system for IIA's observing facilities.

Developing a full-fledged AO is a desirable but challenging goal. The de-

sign and development of an end-to-end AO system are also complicated and time-consuming task. It requires domain-specific expertise in areas of optics, mechanics, control systems engineering and software development. Depending on the availability of funds and resources, complete AO development can take several years. In the present case, the realization of various AO capabilities in IIA is envisaged in three different stages.

In the 1st phase, the importance is given to understanding the site characteristics and estimating the turbulence parameters relevant for AO design. In the second phase, a low order tip-tilt instrument was planned for compensating the stellar image motion. The design, development and realization of higher-order AO system will be taken up in the 3rd phase. In this thesis the work done and progress made in 1st two stages is reported. Atmospheric turbulence parameters, namely, the Fried parameter, isokinetic angle and coherence time, have been measured and reported Sreekanth et al. 2019. Subsequently, the tip-tilt AO system has been designed, built and successfully tested on a telescope for stellar imaging.

The focus of this thesis is on the low order tip-tilt system that is built for 1.3m J.C. Bhattacharya Telescope (JCBT) at Vainu Bappu Observatory (VBO), India. As the telescope is user friendly for operation, has better tracking and better optical quality, it is chosen for technology demonstration of tip-tilt AO system. The tip-tilt system compensates the motion of the star image in the telescope focal plane that arises from the angle-of-arrival fluctuations caused by Earth's atmosphere. In this thesis, the design, development and on-sky testing of a tip-tilt adaptive optics system have been described.

1.4 Thesis outline

This thesis is aimed at measuring the atmospheric turbulence parameters, design and development of the optomechanical system of the tip-tilt instrument and control software, calibrating and testing the instrument in laboratory and finally on-sky performance analysis of its operation in real-time. With these

objectives in mind, the thesis is divided into the following chapters.

1.4.1 Chapter 2: Measurement of atmospheric turbulence parameters

Atmospheric turbulence is a prime contributor to the distortions in the wavefront. It is necessary to measure wavefront distortions at the telescopic site. We initially set out to measure important atmospheric parameters at the JCB telescope. Several pairs of bright stars were observed with a high-speed CCD. The fast exposure image data were analyzed to obtain atmospheric seeing r_0, tilt-isoplanatic angle (θ_0) and coherence time (τ_0). The estimation of these parameters was necessary to arrive at a good AO design. In this chapter, methodology used to measure the atmospheric seeing, tilt-isoplanatic angle and coherence time and results are presented.

1.4.2 Chapter 3: Opto-mechanical design and control software

The tip-tilt instrument is a post focal instrument attached to one of the side ports at the Cassegrain focus of the telescope. It is subjected to strict weight and dimensional constraints. The optical system was designed in ZEMAX ray-tracing software. The mechanical model of the interface unit of the instrument for the telescope is made using AutoCAD software. Control software for the closed-loop operation of the instrument is crucial for the overall performance of the instrument. The LabView based control software with a user interface was designed. The optical and mechanical design, fabrication of the complete tip-tilt instrument and control software are described in this chapter.

1.4.3 Chapter 4: Characterization of the instrument in laboratory

We have used a high-speed, piezo-driven tip-tilt actuator to correct the image motion. A series of experiments were carried out to map the angular deflection of the tip-tilt stage as a function of piezo voltage. These experiments were performed in the lab with an optical setup that has the same focal ratio (F/8) as the telescope. A laser beam passing through a rotating glass wedge and a hot air blown into the beam path was used to mimic the star motion in the lab. In the laboratory, the image motion was simulated by data obtained on the telescope. The induced image motion was corrected using the tip-tilt control operation. In this chapter, the details of the laboratory experiments and tip-tilt calibration and testing are presented.

1.4.4 Chapter 5: On-sky performance analysis

The instrument was commissioned on the telescope in early 2018 and various alignment and tests were carried out. Since then, several observations were made to evaluate the tip-tilt performance of the instrument. It was tested on several pairs of stars to quantify the improvement in angular resolution of the tilt corrected images. The instrument was also tested for different conditions of closed-loop operation and impact of loop frequency and speed was examined. On-sky testing and key results are presented in this chapter.

1.4.5 Chapter 6: Conclusion and future work

As a first step towards the development of the AO system at IIA, the tip-tilt instrument was developed and successfully tested on the telescope. In the next stage of this project, a full-fledged adaptive optics system along with tip-tilt operating in the close loop will be developed, and its performance will be demonstrated on the telescope. Once, the technology is demonstrated, AO systems can be gradually incorporated with regular observations. Finally,

conclusions and future plans are discussed in this chapter.

In the opening chapter, the effect of atmospheric turbulence, the need for adaptive optics, the importance of tip-tilt adaptive optics, AO program at IIA, are discussed. The main objective and scope of this thesis are outlined.

Chapter 2

Measurement of atmospheric turbulence parameters

Sreekanth Reddy V, Ravinder Kumar Banyal, et al., RAA,vol. 19, 74-84, (2019)

Atmospheric turbulence parameters namely, atmospheric seeing, the tilt-anisoplanatic angle (θ_0) and the coherence time (τ_0), randomly change spatially and temporally. These parameters are site-dependent. They determine the specifications of AO systems designed for a telescope. Thus, an adaptive optics design should take into considerations atmospheric conditions measured at observatory site. In this chapter, the methodology used to measure the turbulence parameters at VBO and results obtained are discussed and the importance of these parameters in the design and development of an AO system is described.

2.1 Introduction

The wavefront of light beam arriving from distant astronomical source is aberrated after passing through the turbulent layers of the Earth's atmo-

sphere. The spatial and temporal inhomogeneities in the refractive-index of the air along the beam path produce random phase perturbations, impairing the performance of ground-based telescopes. The influence of wavefront distortion on optical system was investigated by Fried (1965, 1966) using Kolmogorov's model of turbulence. The impact of spatial structure of atmospheric turbulence is described by Fried's parameter r_0, a standard measure of atmospheric seeing.

The wavefront aberrations across the entrance pupil of a telescope are distributed over large range of spatial frequencies. The lowest order aberration is the wavefront tilt which leads to overall angle-of-arrival fluctuations at the aperture plane. This time-varying tilt is responsible for short-exposure image motion (hereafter '*image motion*' means the motion of the centroid of star image) at the detector plane. Fried (1975) had derived the Equation B.1 for the mean-square difference in angle-of-arrival of light seen by two small sub-apertures separated by certain distance that sample the wavefront of a single star as shown in Figure 2.1. This forms the basis for most contemporary seeing measurements carried out with differential image motion monitors (Sarazin and Roddier 1990; Tokovinin 2002; Wilson et al. 1999).

$$\langle \alpha^2 \rangle \approx (1.72/\pi^2)(\lambda/D)^{1/3}(\lambda/r_0)^{5/3}, \tag{2.1}$$

Where, $\langle \alpha^2 \rangle$ is mean angle of arrival fluctuations, D is diameter of the aperture, λ is wavelength of observation.

Full potential of a ground-based telescope is realized by an adaptive optics system which measures the wavefront errors and applies corrections to compensate the tip-tilt as well as the high-order aberrations which cause the blurring.

The wavefront sensing is done either on a bright science target or with a guide star –a natural bright star or a laser beacon created in the close vicinity of faint science target. The wavefront aberrations can differ significantly as the light from guide star and science object take slightly different paths along

the atmosphere. The decorrelation in wavefront errors along two propagation paths is a measure of anisoplanatism. The high order aberrations usually correlate well only over a small angular field ($\lesssim 10''$), while the correlation for lowest order tip-tilt typically extends beyond several 10s of arc seconds. The degree of correlation is again determined by the atmospheric seeing and angular separation (McClure et al. 1991). The variance of wavefront tilt difference from two stars across a common telescope aperture, as illustrated in Figure 2.1, is generally referred to as *tilt-anisoplanatism*.

Previous attempts to measure tilt-anisoplanatism used binary stars at various angular separations. Those observations suffered from restricted bandwidth limitations and lack of bright star pairs at specific angular separations. An early measurement of tilt-anisoplanatism was reported by Barakat and Nisenson (1981); Teoste et al. (1988) with 1.2 m Firepond facility at Lincoln Laboratory. In that experiment two quad trackers measured the differential tilt between three binary star pairs with separation varying from $10''$ to $22''$.

Subsequently, Sivaramakrishnan et al. (1995) used fast readout CCD to capture multiple stars inside a single frame. A linear rise in standard deviation of differential tilt was observed for star separation varying from $10''-58''$. In another experiment images of the moon's edge were used to obtain statistical estimate of tilt angular correlation and tilt averaging functions over a wide range of angular separations (Belen'kii et al. 1997).

The turbulence also produces temporal phase fluctuations along with spatial distortions in wavefront. These fluctuations are characterized by atmospheric coherence time (τ_0). Within this time limit the phase fluctuations are negligible. In AO systems, time interval between wavefront sensing and correction should be constrained within unit τ_0. Thus, it requires a temporal closed loop bandwidth (BW) $>> 1/2\pi\tau_0$. The closed loop bandwidth of a system is the frequency band of operation of a closed loop control system.

As τ_0 is dependent on r_0 and wind velocity, its measurement using short exposure images is influenced by data sampling time (Hardy 1998). Because of this, different definitions of coherence time of phase fluctuations given

by Breckinridge (1994), differ by a factor as large as 7. Based on these approximations, Davis and Tango (1996) have explained the effect of data sampling time on the measurement of turbulence. These earlier analysis have mentioned the optimum sampling time of the order of few milli seconds.

These experiments emphasize the usefulness of fast, short exposure images of a star in determining crucial atmospheric turbulence parameters such as seeing (λ/r_0) and atmospheric time constant (τ_0) and several pairs of stars can be used to measure tilt-anisoplanatic angle (θ_0) (Davis and Tango 1996; Kellerer and Tokovinin 2007; Martin 1987).

Short exposure images were used for the estimation of the atmospheric turbulence parameters, obtained with 1.3 m telescope at Vainu Bappu Observatory. Short exposure images of selected stars were taken with a high-speed CCD camera.

The ability to define multiple region of interest (MROI) was exploited within the CCD frame to record simultaneous position measurements of stellar images with large angular separation up to $\approx 212''$, at the image plane for measurement of θ_0.

The remaining material in the chapter is organized as follows. The details of the high speed imaging camera, target selection criteria, observation methodology and data analysis are described in Section 2.2. In Section 2.3, the seeing measured from the rms image motion is described and compared with that measured from other methods. In Section 2.4, the measurement of tilt-anisoplanatic angle and, in Section 2.5, the estimation of the atmospheric coherence time τ_0 are described. Finally, in section 2.6, the relevance of these parameters in designing an AO system for the telescope is reported. In Section 2.7 we summarize the results.

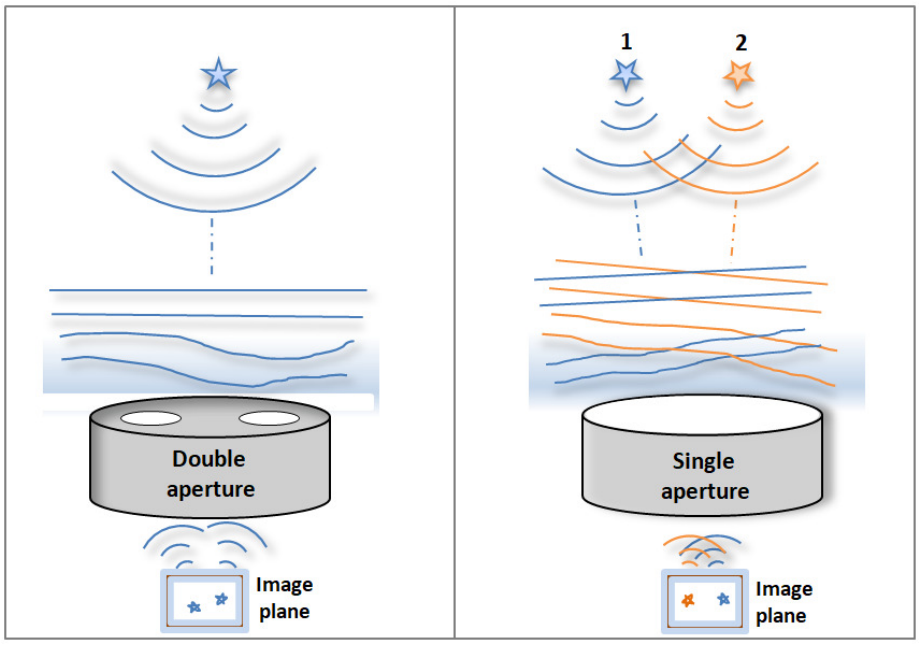

Figure 2.1: Illustration of measuring differential tilt of a stellar wavefront sampled at different locations by two sub-aperture (left-hand panel) and differential tilt between a pair of stars within the field of a mono-pupil telescope (right-hand panel).

2.2 Target selection and observational methodology

The 1.3 m telescope at Vainu Bappu Observatory (VBO), Kavalur, is newly commissioned in the year 2014. It is a Ritchey-Chretien telescope with hyperbolic primary and secondary mirrors. The telescope is located at an elevation of 750 m above the mean sea level at Javadi hills in southern India at $78°50'E$ and $12°34'N$. Prior to the development of an AO system, on-site estimation of turbulence parameters could provide crucial information for the design of such system. Thus, a study of turbulence parameters is started on-site of 1.3 m telescope during the 1st quarter of 2016. The relevant specifications of the telescope are given in Table 2.1.

2.2.1 High speed CCD camera

The rapid imaging requires a high speed CCD. It is desired to have continuous exposure with minimum time lag between two successive frames. For

Table 2.1: Specifications of J. C .Bhattacharya telescope and CCD

Property	Value
Primary aperture diameter	1.3 m
Focal length	10.4 m
F ratio	8
Central obscuration	42 cm
Mount type	equatorial
Camera	Princeton Instruments ProEM xEcelon
Detector size	1024 x 1024
Pixel size	13μm
Pixel scale	0.26$''$
FOV	$\approx 4' \times 4'$
Gain	1.37 e^-/ADU
Read Noise	10.35 e^-
Bit depth	16 bit/pixel
Readout type	Frame transfer
Readout rate	10 MHz

tilt isoplanatic angle measurements two or more objects need to be observed simultaneously in a given field. The lower and upper limit of angular separation between two objects is set by the resolvability between the two objects and the CCD size respectively. The large separation between the objects occupies larger frame size and thus requires more readout time. To avoid reading unnecessary pixels, new technology also permits the selection of multiple ROIs on CCD. This useful functionality can further reduce the readout time.

We used Princeton Instruments ProEm eXcelon (1024×1024, pixel size $= 13\mu$m) EMCCD for our observations. The CCD used frame transfer mode for continuous exposure and simultaneous readout. In this mode, the detector has active and masked areas. After the exposure, the data is vertically (parallel) shifted from active area to masked area. This shift occures within few micro seconds. Thus, the active area is immediately available for next exposure while the image is read out from the masked section[1]. The time lag between two successive frames is 0.8μsec. The current version of the CCD can readout the data with 10 MHz clock speed. It has quantum efficiency (QE) $\approx 90\%$ for visible band of wavelength[2]. The full frame of the CCD cover $\approx 4' \times 4'$ on-sky Field of View (FoV) with plate scale of $0.26''$/pixel. The CCD has an option to capture multiple ROIs within a single frame with user defined window size for each. The CCD specifications are given in Table 2.1.

2.2.2 Observation methodology

The telescope is used for intensive observations in rapid imaging mode. For the operation, target selection with respect to their magnitude, hour angle and declination is crucial. These variables influence the estimation of turbulence parameters.

A list of target was chosen that satisfy the following criteria. The targets

[1] ftp://ftp.piacton.com/Public/Manuals/Princeton%20Instruments/ProEM%20System%20Manual.pdf

[2] https://www.princetoninstruments.com/userfiles/files/assetLibrary/Datasheets/ProEM-HS-1024BX3-and-1KBX3-10um-datasheet-P4-5-16-17.pdf

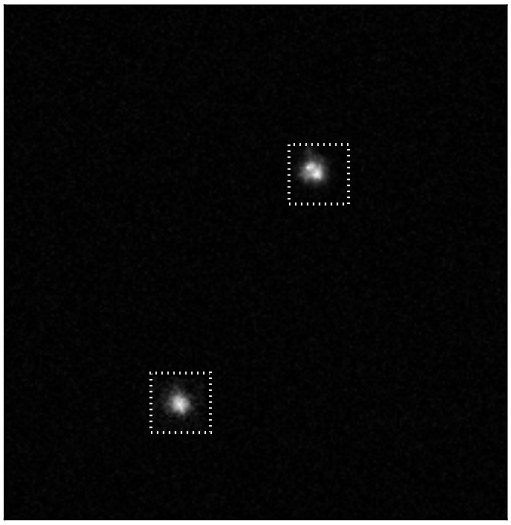

Figure 2.2: A sample frame with 2 target stars observed on 6 April 2015. The object on top-right side (HR4414) has apparent magnitude $m_v = 6.5$ and bottom-left side (83 Leo B) has $m_v = 7.6$. The angular separation between two stars is $28.5''$. The dotted squares indicate the ROI window around each target.

should be bright enough to have sufficient signal to noise ratio (SNR), pair should be spatially resolved and fall within the CCD frame. Thus, multiple pair of stars with magnitude up to $m_v \approx 8$ and on-sky angular separation ranging from $6.4'' - 212''$ were chosen. The target objects are listed from Harvard revised bright star catalogue (Hoffleit 1964). The list of observed objects (brighter companion in each pair) is compiled in Table 2.2.

The observations made on selected targets were carried from evening to midnight. The reason for restriction post midnight is the unprecedented rise in relative humidity (RH) greater than 90%. High RH could cause irretrievable damage to the optics and electronic systems of the telescope. Thus, the observations were confined to below 85% of RH.

The short exposure images of individual stars within CCD FoV were acquired using ROI technique as illustrated in Figure 2.2. The ROI size was varied from 30×30 pixels to 45×45 pixels. This varied size was chosen to confine the image motion within the specified ROI window. This of course depends upon the prevailing seeing conditions and duration of each observa-

Table 2.2: List of observed stars with varying angular separation. In this table, 'Dec' is declination of the object, 'RA' is right ascension,'m_v' is apparent magnitude, 'Δm_v' is magnitude different between two objects and 'sep' is angular separation between the objects in arc seconds.

Object	Dec	RA	m_v	Δm_v	Sep($''$)
HR4414	02 55 39	11 26 45.3	6.5	1.1	28.5
HR3174	-09 17 25	08 06 27.4	6.23	1.7	30.8
HR3428	19 37 50	08 40 20.7	6.44	1.3	63.2
HR4752	25 49 26	12 28 54.7	5.29	1.4	145.4
HR4884	17 00 33	12 52 12.2	6.32	0.6	196.5
HR5010	19 48 03	13 16 32.1	6.49	1.9	203
HR4085	02 18 10	10 24 13.0	6.32	0.3	212
HR4128	-15 15 43	10 47 37.9	6.67	1.2	74.7
HR4193	04 44 52	10 43 20.9	5.79	1.1	6.7
HR4259	24 44 59	10 55 36.7	4.5	1.9	6.5
HR4677	-03 57 14	12 18 09.2	6.99	0.4	20.1
HR7593	-08 13 38	19 54 37.7	5.71	0.8	35.7
HR7672	17 04 12	19 51 17.7	5.8	0.9	203.7
HR7705	20 53 48	20 09 56.6	6.48	0.6	83.9
HR7830	-18 35 00	20 29 53.9	5.94	0.8	21.9
HR7840	11 15 39	20 31 13.1	7.11	0.3	16.7
HR8265	06 37 06	21 37 43.6	6.18	1.5	39.5
HR8619	-28 19 32	22 39 44.2	6.31	1.3	86.6
HR9002	-18 40 41	23 46 00.9	5.29	1	6.6
HR9044	-27 02 32	23 54 21.4	6.35	0.7	6.4
HR310	21 28 24	01 05 41.0	5.34	0.3	29.9
HR313	01 92 24	01 05 49.1	6.35	1	33
HR545	19 17 45	01 53 31.8	4.83	0.1	7.8
HR765	24 38 51	02 37 00.5	6.5	0.6	38.3
HR1065	27 34 19	03 31 20.8	5.96	0.4	11.4
HR1212	-01 12 15	03 54 17.5	4.79	1.5	6.8
HR1322	02 51 62	04 15 28.8	6.31	0.6	64.7
HR1460	-09 44 12	04 35 14.1	6.37	1	12.8
HR1505	-08 47 38	04 43 34.7	6.82	0.1	9.3
HR1600	14 32 34	04 58 59.4	6.09	1.5	39.3
HR1610	03 36 58	05 00 33.9	6.66	0.4	21.3
HR1619	01 36 32	05 02 00.0	6.24	1.3	14.2
HR1753	-18 31 12	05 19 17.4	6.36	0.2	39.3
HR2174	02 29 58	06 08 57.8	5.73	1.2	29.3
HR2356	-07 01 59	06 28 48.9	4.6	0.5	7.1
HR2948	-26 48 07	07 38 49.3	4.5	0.2	9.9
HR3010	-14 41 27	07 45 29	6.07	0.8	16.8
HR3028	-16 00 52	07 47 45.2	6.43	0.1	130.5

tion run. The exposure time is 8-25 ms and each target pair was observed for 10000-100000 frames over $\approx 4 - 25$ minutes.

All our observations were confined to R-band of peak at ≈ 600 nm. The observation details are summarized in Table 2.3.

2.2.3 Data analysis

The raw data from CCD is in *.spe* format. It is a binary data format with distinct sections of header, data and footer. The header contains offset locations of data, time and duration of observation, ROI position on CCD frame, ROI window size, target of observation etc. Each observation of a target is placed in a single binary data file. Prior to data processing, all the image frames needs to be unstacked.

A code was developed in Python software to unstack each of the image frames. As initial step it could read the number of frames, the offset position, dimensions and number of ROIs. The unstacked frames are available for data processing.

Each of the data frame is cleaned prior to analysis. For this, early sky flats have been captured once in a month to know the QE of the CCD pixels known as flat frames. From the available flat frames we used median count to construct the master flat frame. Dark frames were taken for each observation of the target. A master dark frame was created by finding the median of dark frames. Even though the dark noise was minimum, the bias has a significant counts. To minimize the effect of bias and dark noise, master dark frame was subtracted from each data frame and divided by master flat frame. Thus the resultant data was cleaned from bias and flat field errors.

2.2.4 Centroid estimation

Stellar image motion is estimated by using its centroid. The centroid region was limited to a window of 10 x 10 pixels surrounding the maximum intensity pixel and intensity thresholding was applied. The image is distorted and was

Table 2.3: Observation details

Parameter	Value
Wavelength	near R-band (Peak at 600 nm)
ROI size	30×30 to 45×45 pixels
Exposure time	8-25 ms
Magnitude	$m_v < 8$
Hour angle	± 1 hour
Declination	$\pm 30^{\circ}$
Air mass	≤ 1.34
Duration per target	$\approx 4 - 25$ min.
Frames per target	10000-100000
Number of nights	29
Total number of observations	248

randomly moving. The maximum intensity pixel position was continuously traced and an intensity thresholding was applied around the maximum intensity pixel. For short exposure images, the image counts were close to bias counts. To minimize the effect of bias, the dynamic thresholding was fixed as fraction (0.7-0.9 times) of the maximum intensity pixel. This fraction was carefully chosen to avoid bias effect for centroid estimation. This dynamic windowing exercise was aimed at minimizing the effect of noise and effectively track the centroid (Yin et al. 2009). This method of centroid estimation was well suited for closed loop adaptive optics systems for high speed tracking. The first order intensity weighted method was used to estimate the centroid of the clean data.

$$X_c = \frac{\sum W_i x_i I_i}{\sum W_i I_i}, Y_c = \frac{\sum W_i y_i I_i}{\sum W_i I_i}, \tag{2.2}$$

$$\sigma_x = \sqrt{\frac{\sum (X_c - \bar{X_c})^2}{n}}, \sigma_y = \sqrt{\frac{\sum (Y_c - \bar{Y_c})^2}{n}}, \tag{2.3}$$

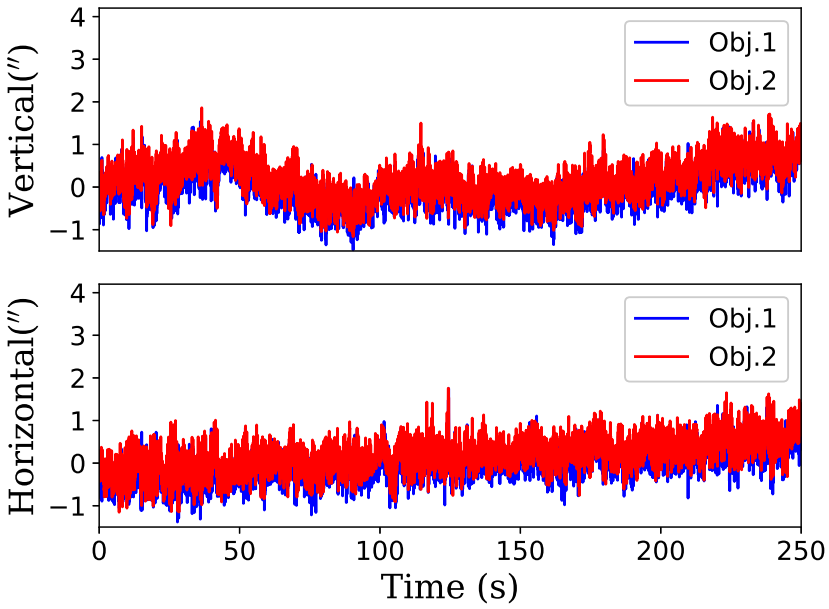

Figure 2.3: Absolute motion of image centroid along horizontal axis (H) and vertical axis (V) of the CCD for object 1 (HR4414) and object 2 of the target pair. In this image X-axis is duration of the observation in seconds and Y-axis is centroid motion of the objects in arc seconds (″).

where X_c, Y_c the estimated centroid coordinates of an image, $I_{i,j}$ are pixel intensities, W_i is the threshold intensity, $x_{i,j}$, $y_{i,j}$ are coordinates of pixels, $\bar{X_c}$, $\bar{Y_c}$ mean value of centroids and σ_x, σ_y are the rms error in centroids.

In Figure 2.3, the centroid motion of star 1 (HR4414) and star 2 along horizontal axis (H) and vertical axis (V) of the CCD is plotted. Both objects were observed simultaneously.

2.3 Estimation of seeing

The Fried's parameter r_0 is a single parameter used to represent the turbulence strength (Fried 1966). It is defined as the spatial scale at which the *rms* phase variation is one radian in the distorted wavefront. It is dependent on the refractive index structure constant of turbulent medium, wavelength and zenith angle of the observations. Refractive index structure constant is integrated over multiple layers of the atmosphere and it varies randomly with time. This causes the continuous random fluctuations in r_0. Instantaneous

variations of this parameter causes the random motion and blurring of the image. In practice, the image resolution is expressed as λ/r_0, also known as the *seeing*.

2.3.1 Seeing from *rms* image motion

We estimated the *seeing* from the motion exhibited by a burst of short exposure images. Essentially, r_0 was estimated from the images using Equation 2.4 (Martin 1987).

$$\frac{r_0}{1m} = \left[\frac{0.0431}{\sigma}\frac{\lambda}{0.5\mu}\left(\frac{d}{1m}\right)^{-\frac{1}{6}}\right]^{\frac{6}{5}}. \tag{2.4}$$

Here, σ is root mean square of the image motion, estimated over 10 s interval of data. As a result,this expression gives r_0 for every 10 s and mean r_0 is calculated for the entire duration of each observation. The estimated r_0 (cm) is converted to atmospheric seeing ($''$). In Figure 2.4, the estimated seeing for object HR4414 is plotted. The mean seeing measured from this observation is $1.49'' \pm 11\%$.

2.3.2 Seeing from FWHM

The mean seeing measured from the aforesaid method is compared with the full width half maximum (FWHM) of the long exposure image. In this case the long exposure image is obtained by co-adding the short exposure images as they have negligible time interval between them. The FWHM of a long exposure image is a standard estimation of atmospheric seeing conditions. Assuming negligible tracking errors within a time span of 10s, one can estimate FWHM every 10 seconds and hence the mean seeing for full length of the observation. The FWHM is related to r_0 as $0.98\lambda/r_0$ and r_0 (cm) is converted to seeing ($''$). The measured seeing for the object HR4414 is $1.54'' \pm 9\%$, on the night of 27 April, 2015.

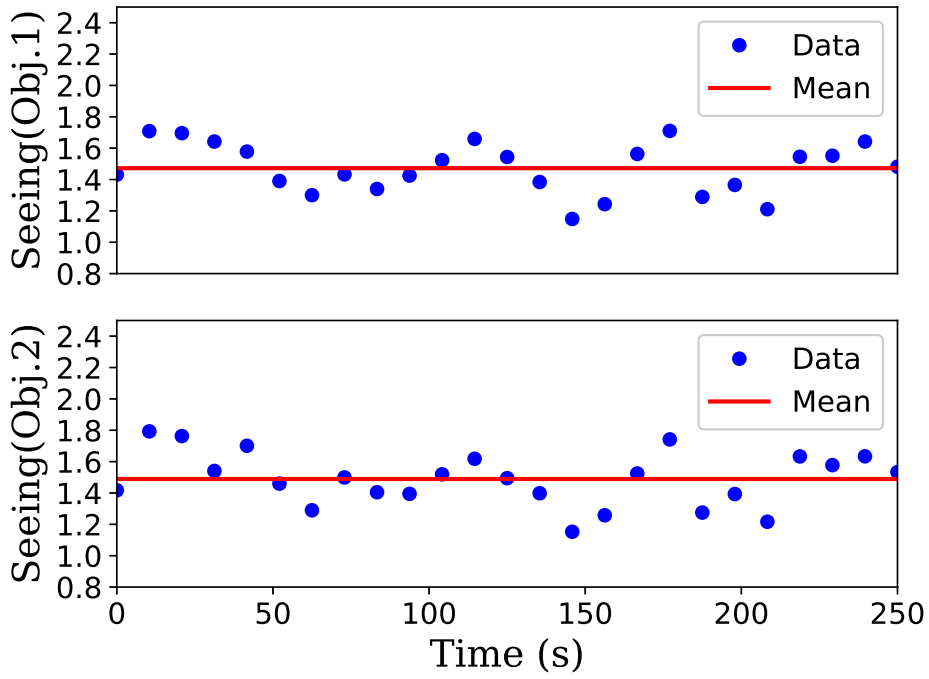

Figure 2.4: Atmospheric seeing measured from the root mean square (*rms*) data of the centroids of HR4414 object 1 (top) and object 2 (bottom). Seeing ($''$) is measured over every 10 seconds. The bold line is the mean seeing. The measured mean seeing is $\approx 1.49'' \pm 11\%$ for both objects.

2.3.3 Seeing from spectral-ratio

Estimation of r_0 using the spectral ratio method was formulated by Von der Lühe (1984). In this method the squared modulus of ensemble averaged Fourier transform of an image ($S_i(\bar{q})$) is divided by the ensemble averaged power spectrum of that image. The observed radial profile is compared with theoretical model to estimate r_0. The expression for the spectral-ratio method reads as follows:

$$\varepsilon(\bar{q}) = \frac{|\langle S_i(\bar{q})\rangle|^2}{\langle |S_i(\bar{q})|^2\rangle} \tag{2.5}$$

$$E[\varepsilon(\bar{q})] = \frac{E[|\langle S_i(\bar{q})\rangle_{SE}|^2]}{E[\langle |S_i(\bar{q})|^2\rangle]} \tag{2.6}$$

In Equation 2.6, E(...) denotes an ensemble average.

The radial profiles obtained from observational data and theoretical model have been over plotted to estimate seeing. The model is simplified and it is

expressed in terms of q and α, where q is wave number and α is modified Fried's parameter. The wave number is defined as the ratio of spatial frequency and theoretical cut off frequency of the telescope $f_c = \frac{D}{\lambda R}$, whereas D is diameter, R is focal length of the telescope and λ is light wavelength. The modified Fried's parameter α is given as r_0/D.

$$\alpha = Aq^B \; \forall \; \alpha \leq 0.3 \tag{2.7}$$

The coefficients A and B have been chosen such that the falling end of the radial profiles of the observational and theoretical models will coincide. The r_0 from observational data is obtained by finding the better represented theoretical radial profiles (Von der Lühe 1984).

We estimated r_0 using this method after incorporating the following two changes: First, we estimated the library of short exposure transfer functions and the speckle transfer functions numerically for our annular aperture geometry (c.f. Figure 2.5) assuming Kolmogorov turbulence model atmosphere. We then estimated the spectral ratio constants A & B using the numerically simulated spectral ratio.

After estimating the theoretical spectral ratio constants for our annular aperture, we used them to estimate r_0 for our observed data. For the object HR4414 the mean was found to be $1.71'' \pm 13\%$.

2.3.4 Comparison of r_0

The seeing estimated using the image motion method, the FHWM and the spectral ratio methods have been compared and the results obtained from these methods are shown in Figure 2.6. It is observed that the seeing estimated from the aforesaid methods has correlation of $\approx 86\%$ (mean of the three correlations). Our observation is that the r_0 estimated from the image motion is higher than that from the spectral ratio method and it is consistent with what has been reported in the literature elsewhere (Goode et al. 2000). However, the exact ratio in our case is 1.14 and it is less than that reported

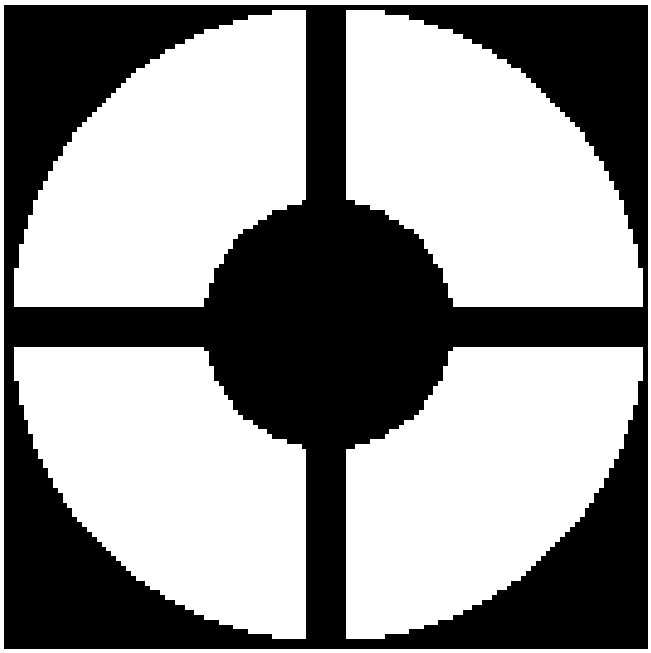

Figure 2.5: The aperture geometry used in simulating the theoretical transfer functions and estimating the spectral ratio constants. The black regions indicate central obscuration and spiders holding the secondary. The white region indicates the useful aperture area.

by Goode et al. (2000). As there is good correlation between the values estimated from different methods, hereafter we refer to the value estimated from the *rms* image motion in our discussions.

2.3.5 Measurement of r_0 over long-term

In Figure 2.7, seeing estimated from *rms* image motion is plotted against the day of observation. It contains mean seeing from 248 observations on more than 50 targets (including the list shown in Table 2.2) observed over 2 years. The vertical line along any night shows the temporal variation of the seeing over the time period of observations. This is because the atmospheric turbulence causes temporal fluctuations in r_0. It varies with time, position of the target and depends on several observational conditions. The mean seeing of the telescope site is evaluated as the statistical average of the estimated seeing over the entire duration of observations. It is estimated as $1.89'' \pm 11\%$. The probability density of observed seeing is plotted in Figure 2.8. The normalized distribution of the data is plotted over the histogram. The median

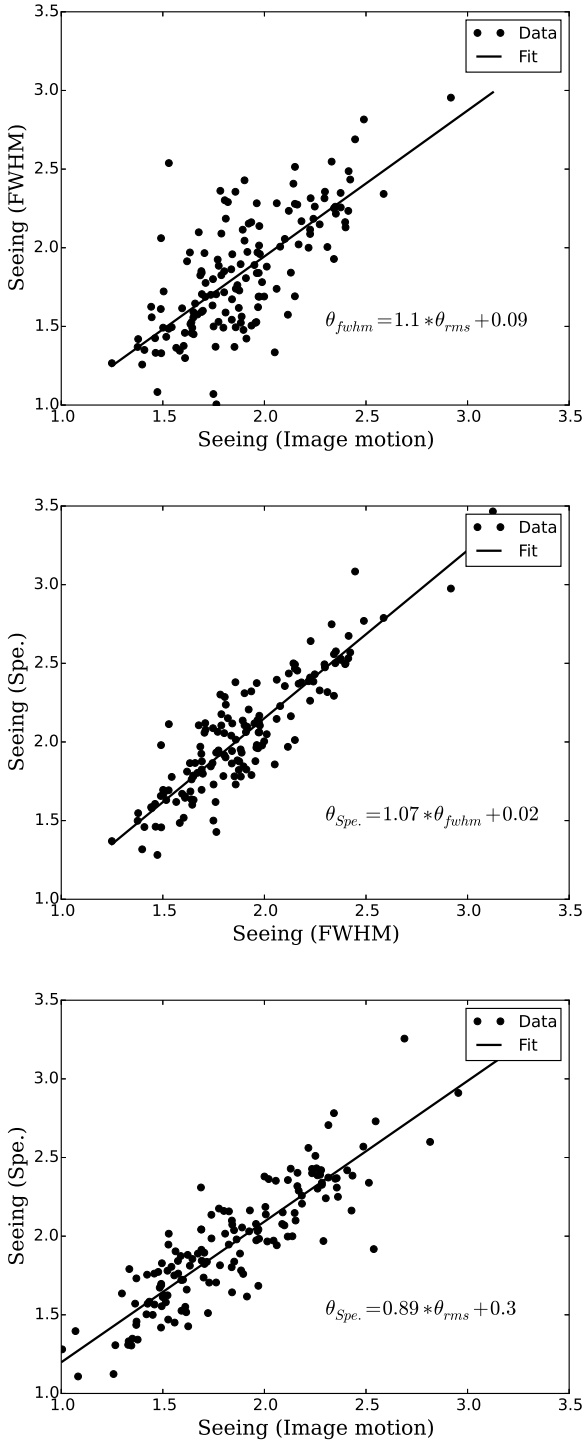

Figure 2.6: Seeing measured from centroid motion of object (*rms*), FWHM and spectral ratio (Spe.) methods has been compared. The units of the axis are in arc seconds. The data points in this plot are seeing measured for the targeted objects. The solid line is the approximated relation between seeing measured from both methods. A linear model has been fit into the data obtained and relation between them is shown in the plot.

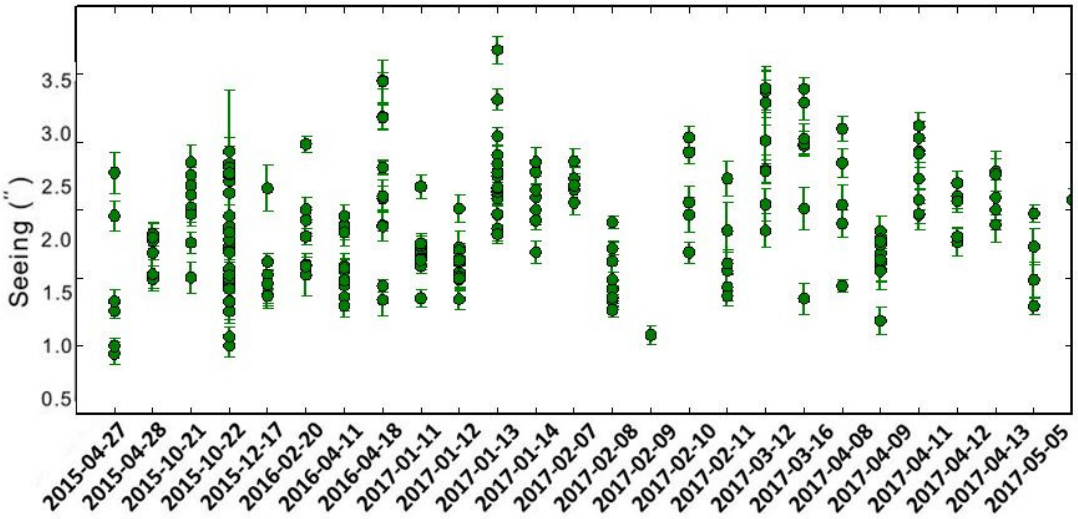

Figure 2.7: Each of the data point with error is mean seeing (″) estimated for each observation. The plot is the result of 248 observations of more than 50 targets observed in 29 nights over a period of 2-years. On average the error in each estimation is $\approx \pm 11\%$. The vertical projection of data points is the mean seeing of the observations during same night. The projection is as high as 1.5″.

seeing at the telescope site is found to be $\approx 1.85''$

2.4 Estimation of tilt-anisoplanatic angle

To estimate θ_0, several pair of stars separated by an angle θ, at the image plane, have been considered. Table 2.2 indicates the targets selected for the estimation. Each of the star pair with ROIs is observed simultaneously with an exposure time of 25 ms. The upper limit on exposure time is due to minimum time required to readout CCD frame (2 ROIs with 40×40 pixels). The duration of observation of each target is $\approx$ 4 minutes, and it corresponds to about 10000 frames. To quantify the relation in their image motion, the centroids of the images are correlated. An expression that is used for the measurement of correlation coefficient (ρ) is shown in Equation 2.8. This parameter is measured for several pair of stars with different angular separation.

$$\rho_x = \frac{\sigma_{x1x2}}{\sqrt{\sigma_{x1}\sigma_{x2}}}, \rho_y = \frac{\sigma_{y1y2}}{\sqrt{\sigma_{y1}\sigma_{y2}}}. \tag{2.8}$$

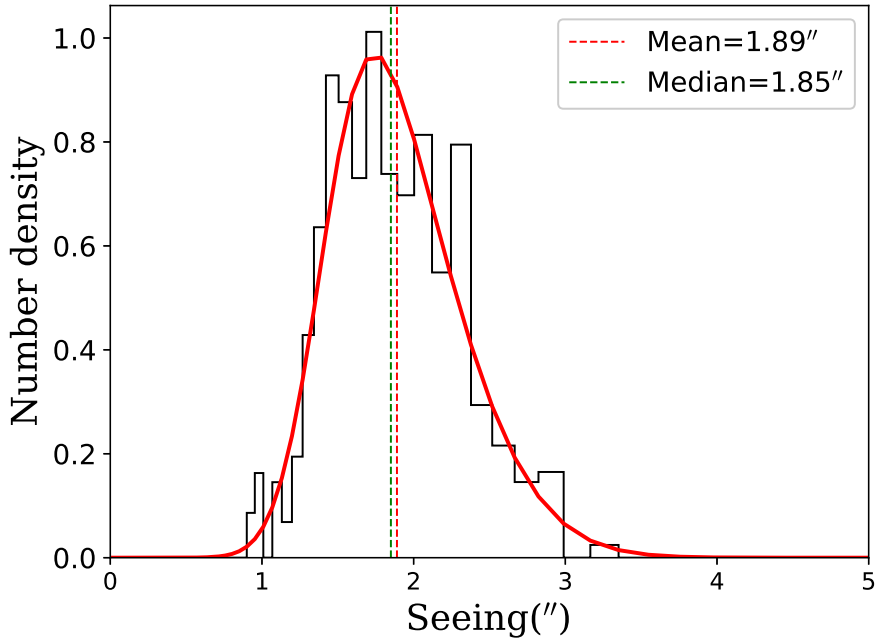

Figure 2.8: Probability density of seeing values and log-normal distribution. The mean and median seeing observed from the data are $1.89'' \pm 11\%$ and $1.85''$ respectively.

In the above equation σ_{x1x2}, σ_{y1y2} is the covariance of the image centroid motions of object 1 and object 2 along H and V axis respectively, σ_{x1},σ_{x2}, σ_{y1}, σ_{y2} are image motion variance (same as Equation 2.3) of object 1 & 2 and ρ_x, ρ_y are correlation coefficients of the image centroid motion along the two orthogonal axis. The estimated ρ is the mean of ρ_x and ρ_y.

The observational data is shown in the Figure 2.9 where ρ is plotted against the θ. It is evident that the ρ is inversely related to θ. Even though image motion correlation is largely dependent on θ, it is also influenced by seeing and wind speed during the observation and zenith angle of the target. The effects of these parameters on the measurement of ρ have been present in the image centroid motion. Thus the measured value of ρ is not purely due to θ rather it is the integrated effect of all these parameters.

$$\rho = a_1 + a_2 \exp[-(\theta/\theta_0)^{5/3}]. \tag{2.9}$$

The θ_0 is obtained from an empirical relation derived from the statistical relation between ρ and θ. To obtain such relation, an analytical expression

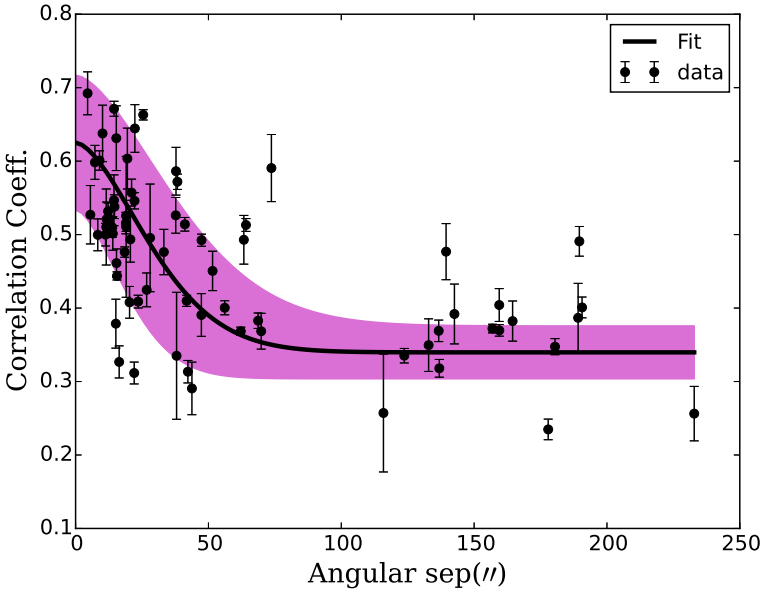

Figure 2.9: The relation between the image motion correlation between stars of a target with respect to the angular separation between them. The plot has 73 observational data points. The X-axis and Y-axis are the angular separation in arc seconds (″) and correlation coefficient respectively. The data has an estimated error as high as ≈ 21%. Approximately, 60% and above of correlation is present at angular separation of 12″. Thick band in orchid color is 5σ level of error estimation. The empirical relation between ρ and θ is mentioned.

(Equation 2.9), based on Kolmogorov turbulence model, has been fit to the observational data. In Equation 2.9, ρ is correlation coefficient, a_1, a_2 coefficients and θ, θ_0 are angular separation and isoplanatic angle respectively. A least square approximation model is fit to the data to estimate these parameters. From this approximation it is estimated that $a_1 \approx 0.34$, $a_2 \approx 0.29$ and $\theta_0 \approx 36''$.

The fitted data plot is shown in solid black line in the Figure 2.9. The thick band in orchid color shows the 5 sigma level of error estimation. Most of the data fall within this limit. The figure shows the image motion correlation between two objects has declining trend with increase in angular separation. Approximately, 60% of correlation has been observed down to angular separation of 12″. The correlation coefficient has reached ≈ 44% at the separation of ≈ 36″.

2.5 Estimation of coherence time

We adopted the following procedure to estimate the atmospheric coherence time (τ_0) from the series of short exposure images. The general idea is to extract a series of phase-fronts from the series of short exposure images.

We make use of the Fourier transform relationship between the image plane the telescope pupil plane and apply the Gerchberg-Saxton algorithm (Gerchberg and Saxton 1972) to recover, iteratively, the complex phase distribution in the pupil plane. We then extract the phase from this complex distribution using phase-unwrapping algorithm. The iterative procedure is shown in Figure 2.10.

The *rms* phase variations of the pupil plane phase ϕ corresponding to each frame is estimated. We define temporal phase structure function D_ϕ as given in Equation 2.10 and model the same as in Equation 2.11.

$$D_\phi(\tau) = \langle |\phi(t) - \phi(t+\tau)|^2 \rangle, \tag{2.10}$$

$$D_\phi(\tau) = \left(\frac{\tau}{\tau_0}\right)^\beta, \tag{2.11}$$

where the angular brackets indicate ensemble average, τ is time to acquire an image, τ_0 is the coherence time and β is a constant.

To simplify the model fitting, Equation 2.11 is rewritten in logarithmic scale. The resultant linear equation is given below.

$$\log[D_\phi(\tau)] = \beta[\log(\tau) - log(\tau_0)]. \tag{2.12}$$

Both β and τ_0 are estimated from the data.

The theoretical value of β is 5/3 for Kolmogorov Turbulence. β & τ_0 estimated for a few representative cases, by fitting the model to the estimated structure functions (Figure 2.11) are provided in Table 2.4. It indicates that the coherence time is varying between 1.5 ms and 3.5 ms and β is varying between 1 and 1.4.

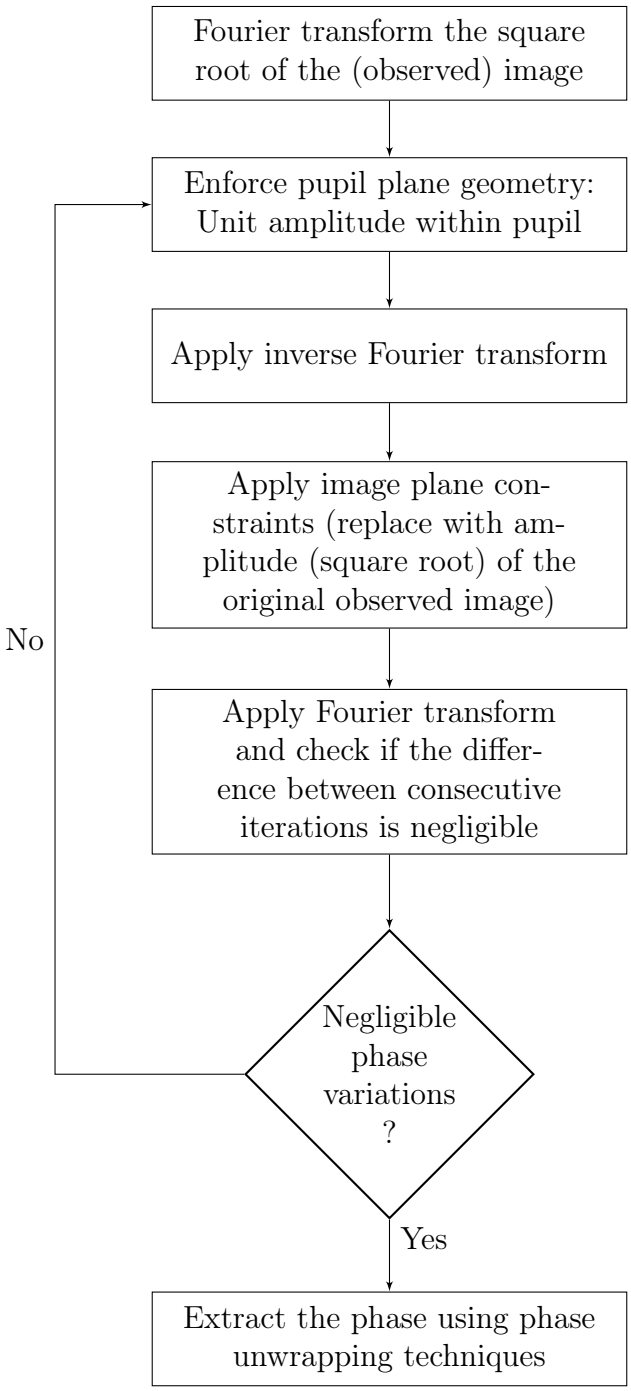

Figure 2.10: Flow chart to extract phase-fronts from observed images.

2.6 Discussions

We have estimated a median atmospheric seeing of $\approx 1.85''$, tilt-anisoplanatic angle of $\approx 36''$ for 44% image motion correlation and a mean coherence time of ≈ 2.4 ms. In what follows, we shall discuss how these values play a decisive

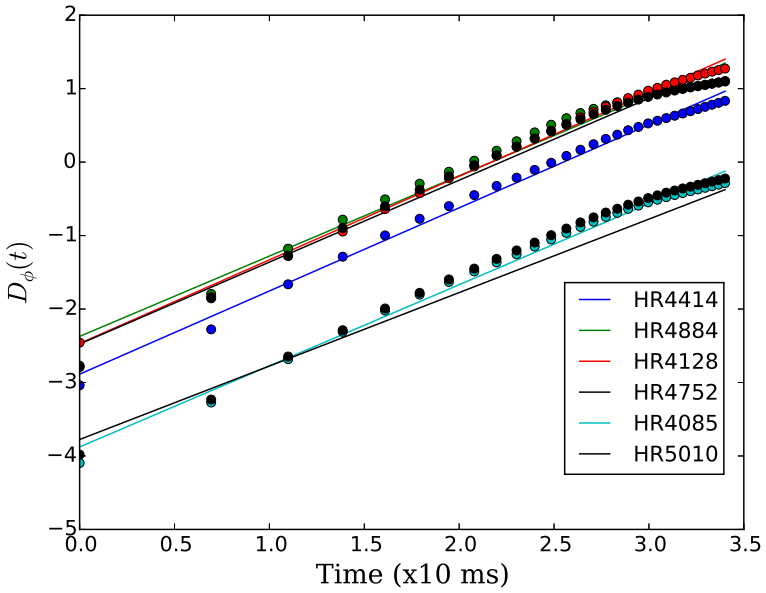

Figure 2.11: Log amplitude of temporal phase structure function. It is ensemble average of the rms phase variations of star images with time. The X-axis is time and the Y- axis is log amplitude of the structure function. The data points in the plot are obtained the observational data and the solid lines are model fit to the structure function.

Table 2.4: Turbulence coherence time estimation. It is measured for different target during the same night. The presented data is of the observation conducted on 27 April 2015. The data contains the power value of the structure function and the coherence time. The mean coherence time is ∼2.4 ms

Object	β	τ_0 (ms)
HR4128	1.13	1.49
HR4414	1.10	3.54
HR4752	1.14	2.53
HR4884	1.12	2.47
HR4085	1.10	2.42
HR5010	1.02	1.90

role in designing AO system for our 1.3 m telescope at VBO. Particularly, we will discuss how the knowledge of these parameters helps to specify the stroke needed for the deformable mirror, the temporal frequency required for the data acquisition and the effectiveness of the AO correction from the lock position.

We shall arrive at the stroke required, assuming that the AO system should lock when r_0 is as low as 5.5 cm. The residual *rms* wavefront error at 600 nm in the instantaneous wavefront (i.e. excluding the tip & tilt) is shown in Equation 2.13 (Tyson 1998).

$$\sigma = 0.366\frac{\lambda}{2\pi}\left(\frac{D}{r_0}\right)^{5/6} = 0.512\mu m. \tag{2.13}$$

Assuming a 5-σ level for the instantaneous wavefront, the peak wavefront error is 2.56 μm. It should be noted that with the reflective geometry, the actual stroke needed will be half of this value. Thus, a deformable mirror with maximum stroke of $\sim$ 3 μm should be conservative upper limit. If we specify 0.1 Strehl ratio at 600 nm, the residual mean square wavefront phase error is 2.3 radian^2. Assigning 1/3 weight to the wavefront fitting error, we arrive at the number of actuators N using the expression given by Hardy (1998).

$$\sigma_{fitting} = 0.3N^{-5/6}(D/r_0)^{5/3}. \tag{2.14}$$

Substituting the values, we get N$\sim$183. Thus, we would require about 180-200 actuators in our system.

The wavefront correction needs to be applied within one coherence time τ_0. The closed loop correction bandwidth is $\sim \frac{1}{2\pi\tau_b}$ where τ_b is the time gap between the wavefront sensing and the wavefront correction. Assuming a factor of six to ten times the closed loop correction bandwidth is required for the AO loop, we arrive at the loop frequency (LF) of $\sim$ 400-600 frames per second. At this frequency the wavefront correction process is executed in a closed loop. This includes the processes of image acquisition, image

processing and correction.

Tilt-anisoplanatic angle (θ_0) is an important parameter for natural guide star AO systems. As discussed in the introduction, the better choice of reference object is its proximity to target, so that the AO system performance will be effective. Thus it limits the effectively corrected field of view for observations. In our case, when we use a bright reference object nearby our target of interest, their angular separation should be less that $36''$ so that at least the tilt component of the wavefront correction will be effective.

2.7 Summary

1. We have estimated r_0 (alternatively the seeing) from 248 distinct observations spanning over 29 days between April 2015 and April 2017. Short exposure images were used to measure r_0 from angle of arrival fluctuations. We compared the estimated values of seeing from three different methods and found that the values match with 14% uncertainty.

2. With the limited data, the median seeing at 600 nm is found to be $1.85''$, the tilt-anisoplanatic angle θ_0 is $36''$ for 44% correlation, and the atmospheric coherence time, estimated for six different observations, is found to be ~ 2.4 ms.

3. The estimated parameters should be considered preliminary, as the values are likely to change with atmospheric conditions at the site. Nevertheless, it helps in fixing the design parameters of the adaptive optics system to be built for this telescope in future.

4. The observed values reinforce the need to build an adaptive optics system for achieving diffraction limited resolution. An infra-red AO system will be preferable as the coherence time is likely to be better than what has been observed in the R-band.

In this chapter, the methodology of measurement of the turbulence parameters by using the short-exposure images was discussed. The AO system input requirements regarding the wavefront sensor and the deformable mirror and the closed-loop frequency of operation for effective correction of the wavefront were approximated. In the following chapter, the optomechanical design of the tip-tilt AO system designed for the JCB telescope at VBO is discussed.

Chapter 3

Opto-mechanical design and control software

3.1 Introduction

The tip-tilt instrument is simplest part of adaptive optics system. As discussed earlier, this instrument compensates for the image motion induced primarily by the atmosphere. The development of such instrument includes design of an optical system, a mechanical interface unit that houses the subcomponents and development of a control software. The optics is designed to enhance the system resolution. The mechanical design of the instrument is crucial to house all the sub systems and needs to be robust to minimize external disturbances. The software should control the camera to acquire images, measure the shift in image and control the tip-tilt stage to correct the image motion in real-time.

In this chapter, the optical, mechanical design of the instrument and the control software are discussed.

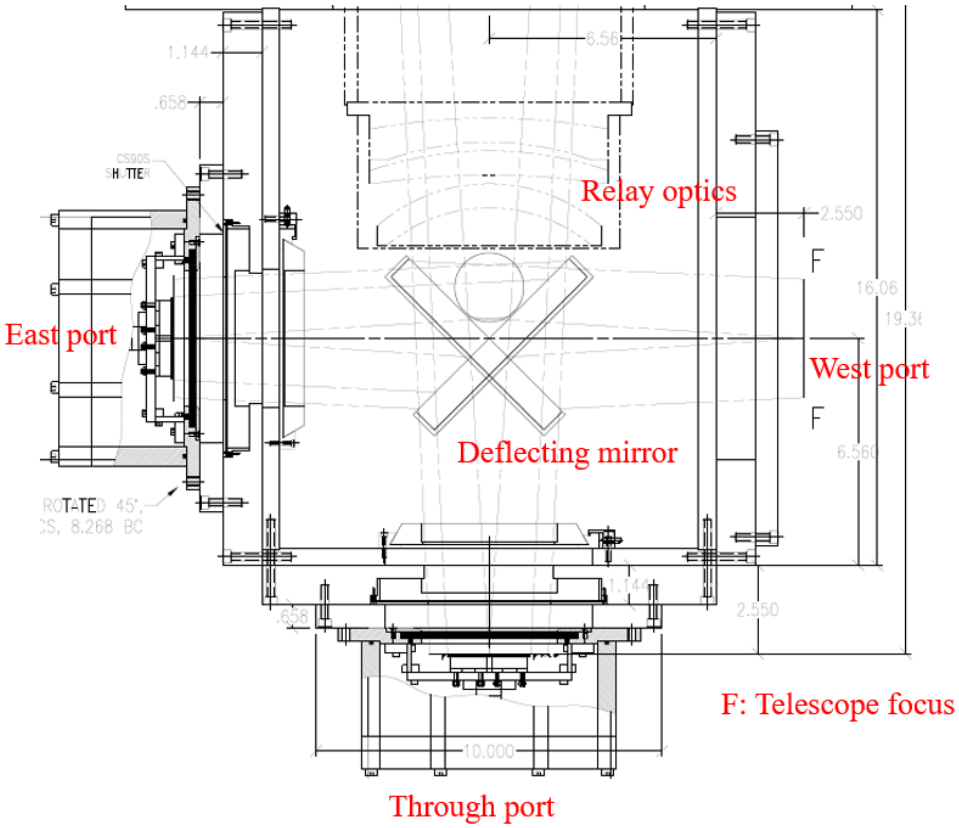

Figure 3.1: Layout of instrument interface unit of JCB telescope. Tip-tilt instrument was designed for the West port.

3.1.1 The telescope

The tip-tilt system was designed for 1.3 m telescope, Vainu Bappu Observatory. At the Cassegrain focus the telescope produces a F8 beam. This is the input beam to tip-tilt instrument.

The telescope has an instrument interface unit (IIU) mounted on it. In this unit various sub-components, namely deflecting mirror to steer light beam, optical filters and relay optical elements are placed. The IIU has three ports to mount auxiliary instruments for astronomical observations. These ports are dubbed as East, West and central/through port. The deflecting mirror in IIU guides the light beam towards one of these ports. The IIU of the telescope is shown in Figure 3.1. The tip-tilt instrument was designed for the West port of the IIU.

Before discussing the design of optical system, sub-components of the tip-tilt instrument namely, tip-tilt stage, image motion sensing camera and the imaging camera are briefly described. The physical dimension and weight of these sub-components also guide the design.

3.1.2 Sub-components of the instrument

A brief description of essential sub-components of tip-tilt instrument is as follows:

- **Tip-tilt stage**: We used a fast steering tip-tilt stage from *Physik Instrumente*[1] (Model: S-330). It is a Piezo-based actuator system with two orthogonal axes. Each axis has two actuators that work on the opposite polarity of an applied voltage. These axis are able to deflect the light beam with 0.5 μrad resolution over a 10 mrad tilt angle. The tip-tilt stage has one-inch diameter platform to mount a mirror that steers the light beam projected on to it. The stage is driven by *Physik Instrumente* E-517 control system that has proportional, integral and differential (PID) internal voltage controller to provide a position accuracy of 0.5 μrad in a close-loop operation. In Figure 3.2, the schematic of the tip-tilt stage is shown. The stage has four Peizo actuators, two on each of the two axes. The actuators of an axis have two opposite polarities voltage to be applied. The actuators move complementary to each other. Thus they have balanced and stable motion. A platform is provided, that is connected to these actuators, to mount a mirror on it. The motion in actuators cause relative tilt in the mirror. Then, light beam projected on to this mirror will be tilted. A calibrated movement of the actuators controls the trajectory of light beam. Thus, the tip-tilt stage was used to correct the image motion. The technical specifications of the stage are listed in Table 3.1.

[1] https://www.physikinstrumente.com/

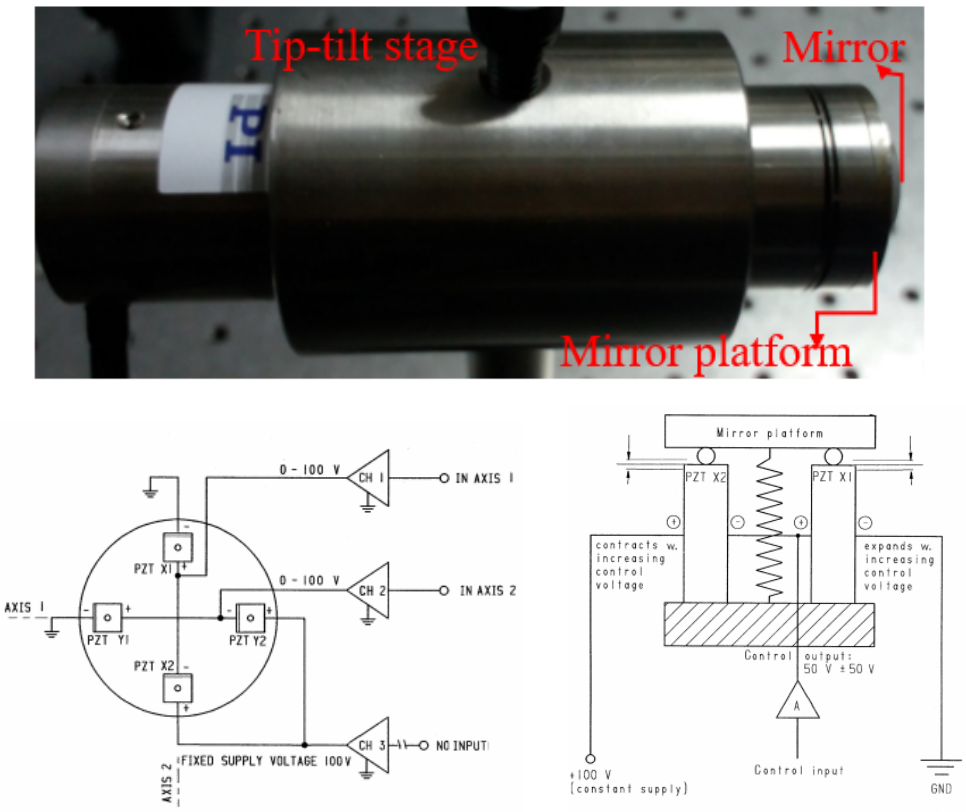

Figure 3.2: Tip-tilt stage mounted in cylindrical holder (top), Actuator system (bottom-left) and the platform to mount mirror (bottom-right).

Table 3.1: Tip-tilt stage specifications

Model	PI S-330SL
Active axis	θ_x, θ_y
Operating voltage	0 to 100 V
Closed loop angle	10 mrad
Closed loop angular resolution	0.5 μrad
Humidity (upper limit)	80%
Temperature (upper limit)	60^0 C
Mirror diameter	12.7 mm
Mirror Thickness	6 mm
Mirror weight	20 gm

- **Sensing camera**: The performance of the tip-tilt instrument depends on its ability to sense the image motion and apply the necessary correction. The sensing camera should be able to operate at high frame rate to record the random motion in the stellar images. Here, frame rate is the frequency of image frames acquired and readout by the camera. We used *Andor Neo-sCMOS* 2560×2160 format, high-speed camera[2]. For exposure time of 1 ms and frame size of 128×128 pixels, we could achieve a frame rate of ~ 300 using control software developed on LabView platform. With 6.5 μm pixel size and the magnification achieved by the relay optics, the sensing camera is able to sample the sky with $0.06''$/pixel.

- **Imaging camera**: We used *Princeton Instruments* ProEm eXcelon (1024×1024, pixel size = 13μm) EMCCD[3] for recording tilt corrected images. The CCD was used in continuous exposure mode with simultaneous read out of the data. This is a frame transfer operation. In this mode, the data in active area is vertically shifted to a masked area. This operation takes few microseconds (0.8 μsec) and enables the active area to be available for next exposure. The full frame of the CCD cover $\approx 1' \times 1'$ on-sky field of view (FoV) with plate scale of $0.08''$/pixel.

The relevant specifications of the aforesaid components have been considered to guide the optical and mechanical design of the instrument.

3.2 Optical system design

An optical system of the instrument was designed in ZEMAX ray tracing software. Several design parameters, including effective focal length and dimensions of the instrument were considered. The pixel scale at telescope Cassegrain focus is $0.26''$/pixel (pixel size = 13 μm) while the diffraction

[2]https://andor.oxinst.com
[3]https://www.princetoninstruments.com/

Table 3.2: Key specifications of tip-tilt instrument. Telescope and instrument optical system design is shown in Figure 3.3. $F/_{\#}$: F-ratio, PS: Pixel Scale.

Property	Value
Wavelength range	480-700 nm
wave-front sense plane FOV2	$40''$
Image plane FOV1	$1' \times 1'$
Telescope focus $F/_{\#}$, PS	8, $0.26''$
Sensor camera $F/_{\#}$, PS	15.7, $0.06''$
Imaging camera $F/_{\#}$, PS	22.4, $0.08''$
Size	80 cm $\times$ 50 cm $\times$ 30 cm
Weight	28.7 kg

limited resolution is $0.1''$ at 630 nm wavelength. In the optical design of the instrument, the pixel scale was reduced to half of the diffraction limited resolution. This improved the sensitivity of the telescope to measure the image motion.

The optical system design of the instrument is shown in the Figure 3.3. The instrument is shown in inset of the window. Its a post-focal system, designed for the West port of the telescope. Various elements are labelled and spatial distance between these elements are mentioned in the Figure 3.3.

The diffraction limited resolution of the telescope at the telescope focus is $0.1\,''$ in R-band the CCD pixel scale is $0.26''$. This implies that telescope point spread function (PSF) is under sampled. For high resolution imaging, the star image at the sensing arm and the imaging arm need to be finely sampled (e,g. Nyquist criteria demands 2-pixel sampling in the image plane) to detect image motion and for correction close to diffraction limited resolution. The relay optics in the tip-tilt instrument were designed such that the star image is optimally sampled. The imaging arm of the instrument was designed to have f/# of 22.4 . This gives the pixel scale of $0.08''$ for 13 μm size CCD pixel. The imaging arm has diffraction limited field of view (FoV) of $1' \times 1'$. The

Figure 3.3: Optical system design of the instrument. Optical system with the telescope (left) and tip-tilt system design(right). F1: Telescope focus, L1: Collimating lens, TT: Tip-tilt mirror, M1: Fold mirror, BS: Beam Splitter, L2: Imaging lens, F2: Sensing camera focus, M2: Fold Mirror, L3: Imaging lens, F3: Imaging camera focus. F1-L1=11.42 cm, L1-TT=4.92 cm, TT-M1=9.09 cm, M1-BS=15.31 cm, BS-L2=3.5 cm, L2-F2=9.72 cm, BS- M2=4.32 cm, M2-L3=5.24 cm and L3-F3= 17.24 cm.

sensing arm of the instrument has diffraction limited FoV of 40″ with pixel scale of 0.06″. The instrument is designed to work in visible band (480-700 nm). To analyze the end-to-end performance of the optical system design, it was integrated with the telescope optics design. Thus the instruments end-to-end optical system performance was analyzed.

After preliminary design with required specifications, we have chosen off-the-shelf optical components from vendors (*Thorlabs* and *New Port*). The specifications of these components, as shown in Figure 3.3, are given below.

- **L1 (*NewPort:PAC028AR.14*)**: This is collimating lens of size 1.27 cm diameter with focal length of 4.9 cm. The lens collimates on-axis beam size of ~ 6.1 mm.
- **L2 (*NewPort:PAC052AR.14*)**: It is imaging lens of size 2.54 cm diameter with a focal length of 9.72 cm. L2 is placed before sensing camera.
- **L3 (*NewPort:PAC061AR.14*)**: It is imaging lens of size 2.54 cm diameter with a focal length of 17.24 cm. It is placed before imaging camera.
- **BS (*Thorlabs:BS013*)**: It is a 30×30 mm^2 size caged cube beam splitter with split ratio of 50:50. It has surface flatness of $\lambda/10$ at 633 nm.
- **M1 and M2 (*NewPort:10D10AL.2*)**: These are fold mirror of 2.54 cm diameter each.

These The optical prescription of the components were loaded in the design at their appropriate location. The performance of this off-the-shelf optics was analysed in ZEMAX. The performance of the optical system is shown Figure 3.4. In this figure, two sets of images of spot diagram and encircled energy for imaging arm and sensing arm of the optical system are shown.

The spot diagram is the measure of convergence of an image of a point object. For an aberration free wavefront (ideal case), the image converges to a point in spot diagram. In reality, the spot diagram has finite size with a Field-of-View (FoV). In Figure 3.4 the spot diagram is shown for five different wavelengths within the wavelength range of from 480-700 nm. The top panel (imaging arm) has a FoV up to $1' \times 1'$, the diffraction ring of the spot image is shown in black colour. Similarly, the spot diagram for sensing arm is shown in the bottom panel of the image with diffraction ring size of $40'' \times 40''$.

As shown in Figure 3.5 the Geometric encircled energy was plotted for the imaging and the sensing arms of the optical system. In both the arms $\sim 90\%$ of the energy is concentrated within 35 μm for the wavelength range of 480-700 nm.

The analysis of the optical system has shown a satisfactory performance with components available off-the-shelf. Based on the analysis of spot diagram and geometric encircled energy of the optical system, the design was frozen for implementation on the telescope.

3.3 Mechanical design of the instrument

Our tip-tilt system is a post-focal instrument. A complete solid model of the instrument with mechanical enclosure was designed in AutoCAD software. The instrument was designed for the West port of the telescope. The port has several constraints regarding the dimensions and weight balance for the instrument. The instrument design qualifies all the requirements for proper mounting and operation. The 3D version of the solid model of the tip-tilt instrument is shown in Figure 3.6. The telescope focal plane is at 2.5 cm from the edge of IIU. A field stop was placed at telescope focal plane to block the stray light from entering into the instrument. The field stop has a 3 mm hole to allow a light within FoV of $1' \times 1'$. Other relay optics, namely

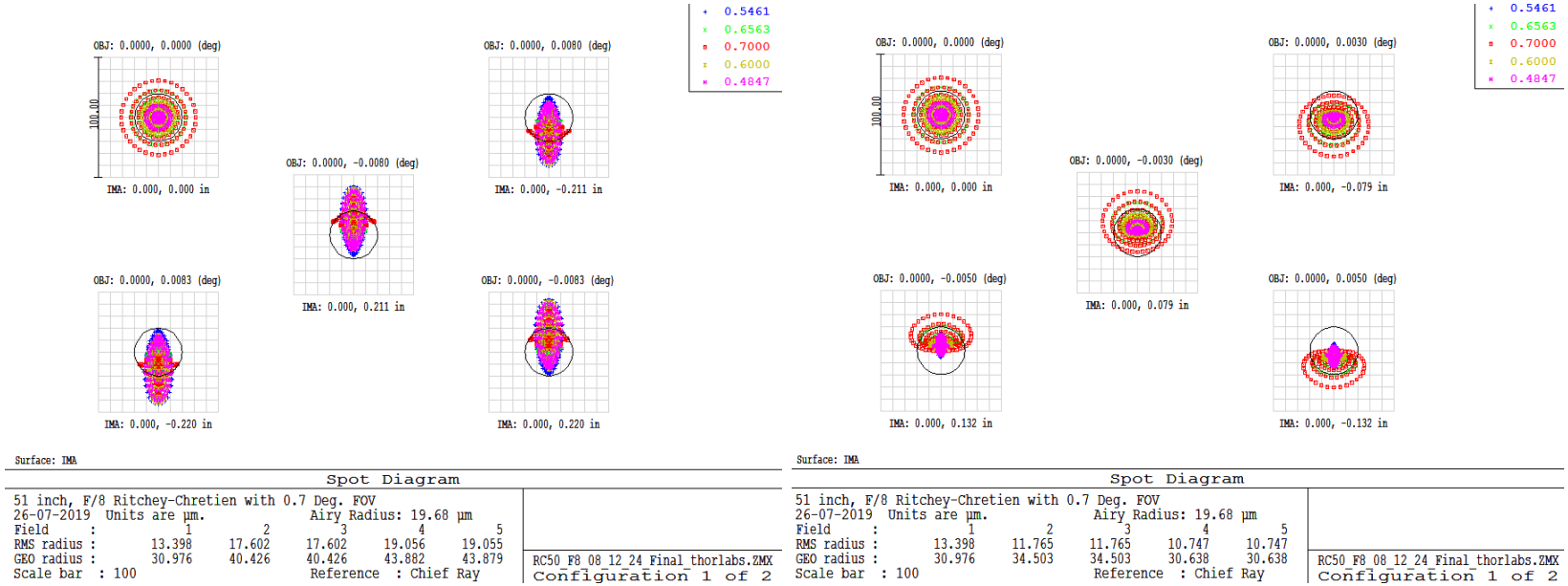

Figure 3.4: Spot diagram and encircled energy diagram. Spot diagram of imaging arm (left) and sensing arm (right). The diffraction ring is shown in black colour.

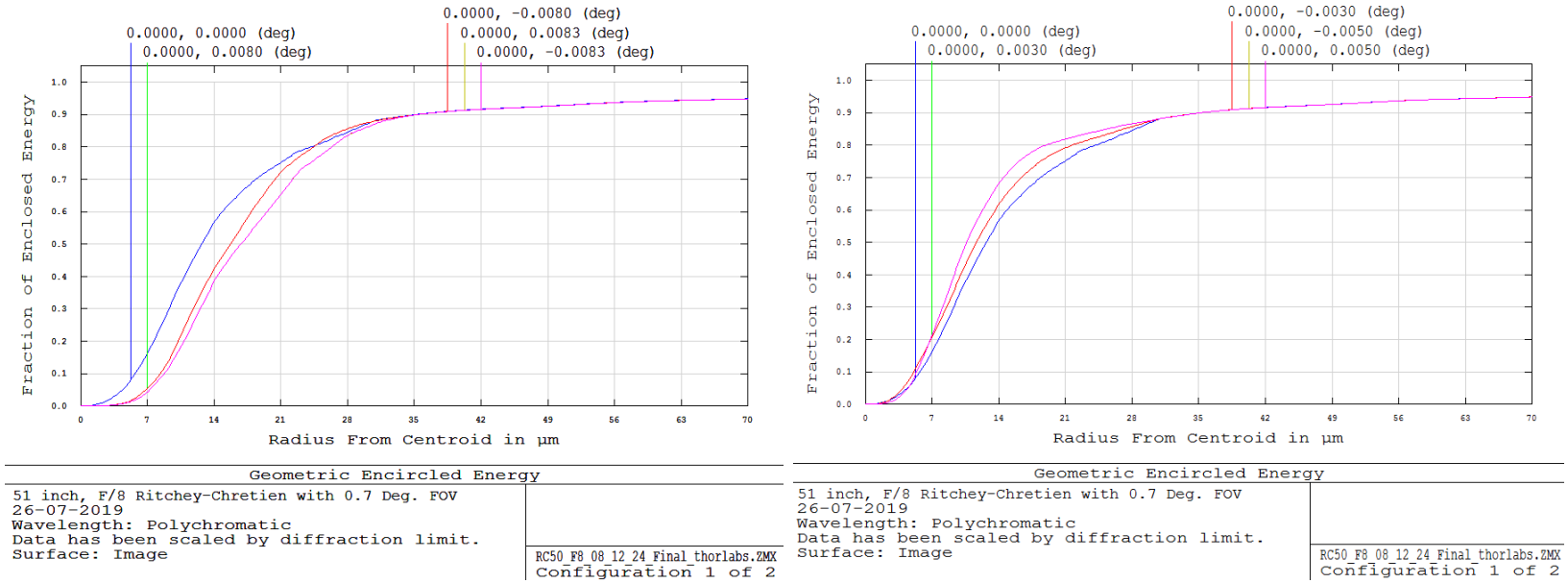

Figure 3.5: Encircled energy diagram of imaging arm (left) and sensing arm(right). Approximately 90% of energy is confined to 35 μm.

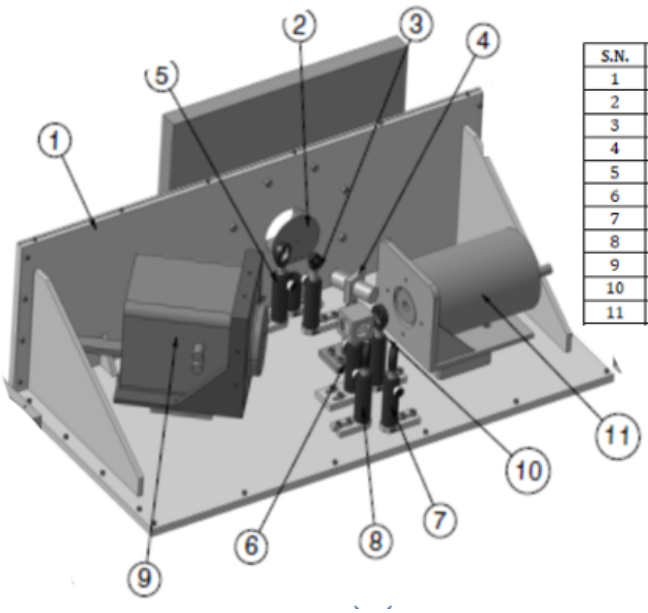

S.N.	ITEM	QTY.
1	BASE	1
2	FIELD STOP ASSEMBLY	1
3	LENSE L1 ASSEMBLY	1
4	TIP TILT STAGE ASSEMBLY	1
5	FOLD MIRROR ASSEMBLY	1
6	BEAM SPLITTER ASSEMBLY	1
7	FOLD MIRROR-2	1
8	LENSE L2 ASSEMBLEY	1
9	IMAGE CAMERA ASSEMBLY	1
10	LENSE L3 ASSEMBLY	1
11	SENSE CAMERA ASSEMBLY	1

Figure 3.6: A CAD model showing the mechanical layout and system components.

collimating lens, tip-tilt mirror, fold mirrors, beam splitter and imaging lens were fixed at their respective location based on the optical system design.

The two cameras are placed on screw gauge mounted stages. The suitable camera holders have been developed to fix the cameras on the stage. A place holder is mounted on the base plate to match the height of the camera sensor with the optical axis of the instrument. This careful design allows us to place the camera at the middle of the focal plane. These stages have a motion within range of 1 cm with resolution of 10 μm along the optical axis. The stages were helpful to place the cameras in focal plane of the image. The fold mirrors were mounted on the horizontal (H) and vertical (V) tilt correction holders. This enable us to correct for tilt misalignment. The base plate has provision to place all the sub-components in their respective positions. All the components are aligned with respect to the optical axis of the instrument.

The instrument weighs $\approx$ 28 kg and has dimensions $80 \times 60 \times 30$ cm^3. A mechanical model designed in *AutoCAD* is shown in left panel of Figure 3.6. Some key specifications of the telescope and the tip-tilt instrument are listed in Table 3.2.

3.4 Control Software

The instrument control software is crucial for inter-operation of the tip-tilt stage and the sensor camera. The software controls these two components and performs the tip-tilt operation. In this section, we discuss various commands to operate these components, the tip-tilt control functionality and the possible errors while executing the program.

Control software with graphical user interface (GUI) was developed using National Instrument's LabVIEW platform[4] to operate the instrument. The software ensures the interoperability between the sensing camera and the tip-tilt stage. The program flow of the control software is shown in Figure 3.7. As shown in the flowchart, the connectivity of the tip-tilt stage and the camera is checked during the initialization step. Subsequently, the exposure time, the number of frames to obtain are set, following which the tip-tilt actuators are initialized. To improve the system performance master slave technique is implemented in control software. The master slave loop architecture is commonly used when two or more processes need to run simultaneously but at different rates. If these processes are run in single loop, the system response gets delayed. The master slave architecture has one master loop and the remaining act as slave loops. The master loop controls all the slave loops. The program has one master loop and one slave loop where the former independently acquires the image frames, and the later process them in sequence to estimate the centroid. The independence of the master loop from its slave improves the loop frequency of the system. The tip-tilt stage corrects for each of the centroid shifts in real-time to compensate for the image motion. The software has the option to save the image and centroid data.

[4]http://www.ni.com/

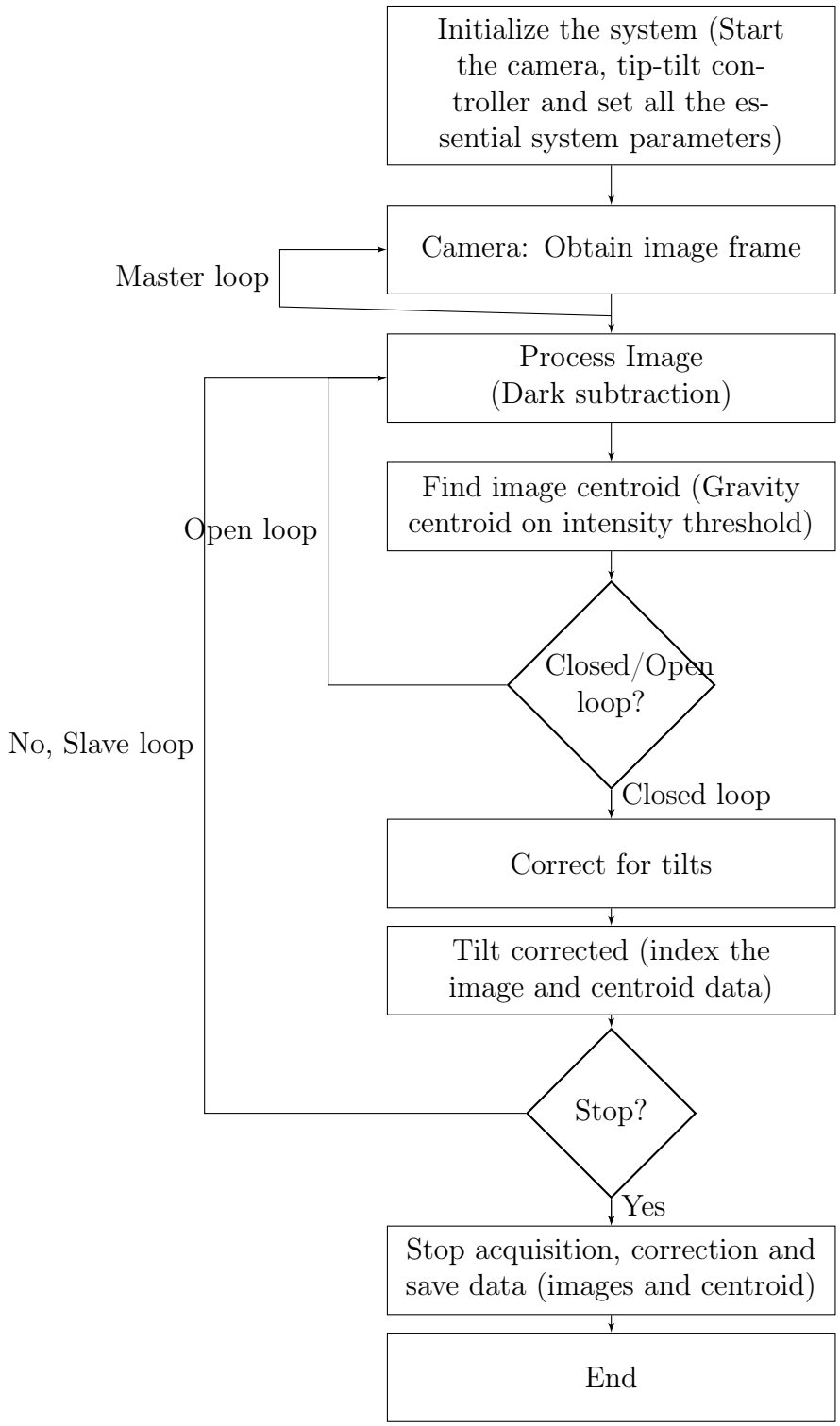

Figure 3.7: Flow chart of tip-tilt control software.

3.4.1 Control program

The control program was divided into three sections that include, the control of the tip-tilt stage, the sensing camera and the tilt correction. The software initializes the tip-tilt stage and the camera. The customized control operation is necessary to have end-to-end access to the instrument control operation and for interactive control of these sub-components. These components have initial settings which guide the control sequence of the program. In the following subsections, we discuss the necessary subroutines of the program.

3.4.1.1 Tip-tilt stage

The tip-tilt stage has several controls that need to be setup. They include the setting of the axis, the bit size and specification of the closed-loop or an open-loop operation. The tip-tilt stage has E-517 controller to operate it. This controller has USB/RS232 communication interface to connect it to computer (Dell Optiplex 7050[5]) to enable user control. The tip-tilt stage Physik Instrumente corporation provides software development libraries in LabView. These libraries have LabVIEW pallets to perform various functions to control the tip-tilt stage. Using these LabView pallets a customized control software was developed.

- **Axis to set**: The tip-tilt stage is a two-axis system, namely axis A and axis B. The axis need to be set up to match its equivalent axis with the camera.

- **Closed-loop**: This closed-loop operation initializes the internal servo of the E-517 tip-tilt controller. The internal PID controller was optimized for closed operation of the tip-tilt stage.

- **Bit size**: The digital input to drive the stage accepts 8-bit data. For high-frequency operation, the instrument needs to be given a 4-bit data

[5]https://www.dell.com

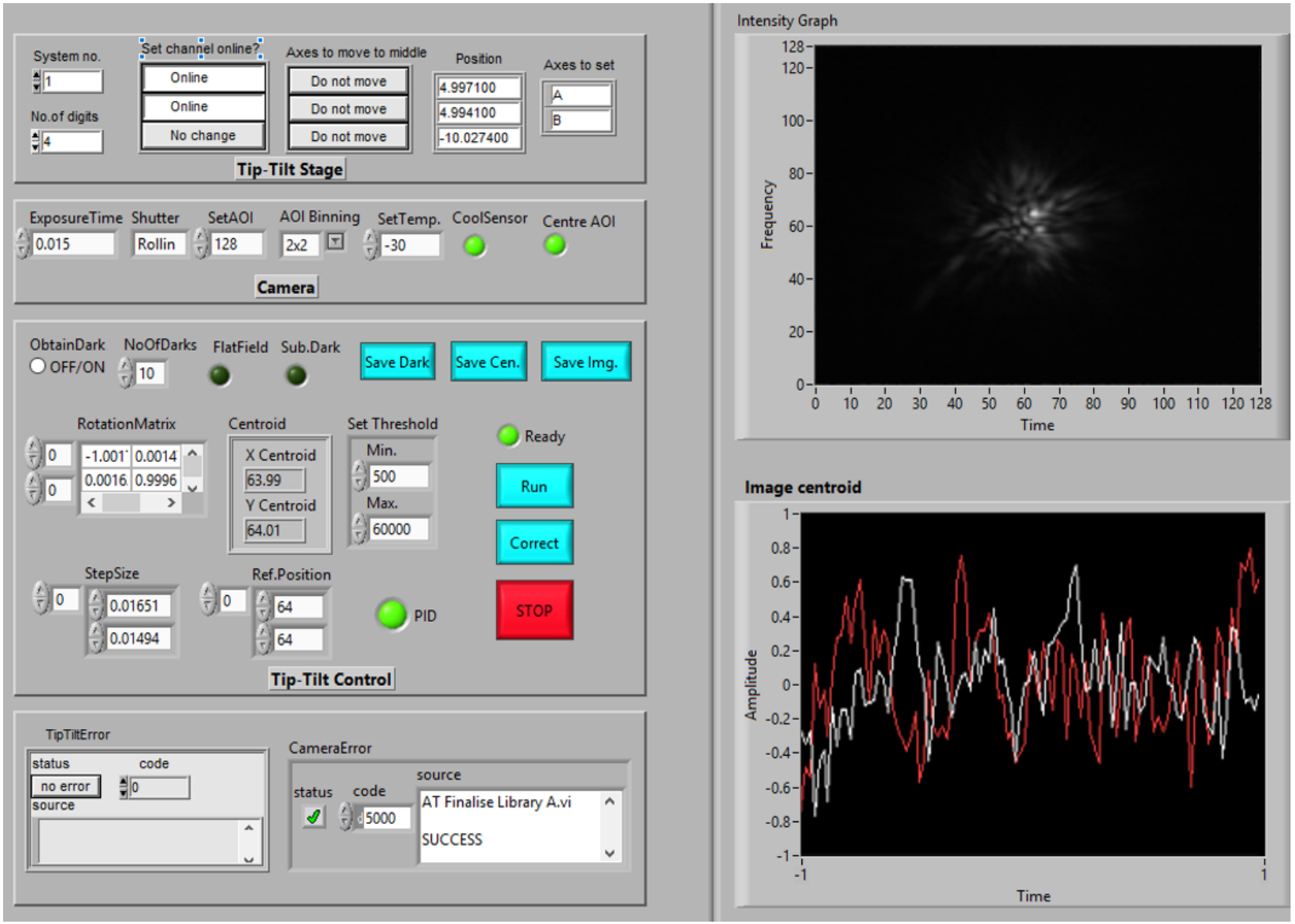

Figure 3.8: Tip-tilt instrument control program user interface.

to increase the loop frequency.

3.4.1.2 Sensing camera: Andor Neo sCMOS

The customized control of the camera software was developed in LabView by using the *System Developed Tool Kit* provided by *Andor* corporation. We used *SDK 3.0*, which is compatible with developing control software for *Andor Neo sCMOS* camera. This camera has several controls regarding the exposure time, temperature control, readout mode, binning, Area of Interest (AoI).

- **Exposure time**: Set the camera exposure time in milliseconds. It determines the output frame rate of the camera for given frame size.

- **Temperature control**: The sCMOS cameras have relatively high readout noise. The camera needs to be cooled down to negative temperatures to reduce the noise level. The camera can be cooled down to -60^0C. The RMS noise can be effectively minimized to 1 electron per count. The temperature was actively controlled by setting the cooling option.

- **Readout mode**: The camera has two software enabled types of readout modes. These modes are rolling shutter and global shutter. In rolling shutter mode, the pixel data is read row-wise while the exposure was given continuously. In this mode, the frame rate is high. In global shutter mode, the consecutive exposures will be given after a readout of the selected pixel with the area of interest. It lowers the achievable frame rate.

- **Binning**: In weak signal conditions the binning will help by cumulative additions of the camera pixels. It is post readout binning with 2×2 up to 8×8. Essentially it is to read out the pixels by combining them in a defined bin size.

- **AoI**: This selects the area of interest (AoI) specified by the user. The AoI was chosen around the object in the field. The selection of AoI will minimize the readout time of the frame, hence, improves the frame rate. For high-speed operation, the selection of AoI is essential. The position of the AoI in the camera frame also influences the frame rate. The centre portion of the camera could give maximum frame rate. Thus, it is always advisable to align the object at the centre of the camera and set the AoI choice as centre using the control.

3.4.1.3 Tilt correction

This is the core part of the tip-tilt control program. After the images have been acquired, they are processed to find the centroid shift and estimate the amount the input voltage that needs to be given to the tip-tilt stage. In this process of the correction, the following controls are essential.

- **Set rotation matrix**: It is a 2x2 array for axis rotation that was aimed at the aligned movement of the tip-tilt stage axis. These elements of the matrix are obtained by calibrating the instrument, which is discussed in the next chapter. The rotation matrix is multiplied with the centroid to map the correction required to apply to the tip-tilt stage. This value multiplied with step size, give the final value of the shift. It is converted to voltage to apply to the tip-tilt actuators.

- **Step size**: This is the amount of axis movement that needs to be set to cause a pixel shift. It is measured during the calibration of the instrument.

- **Dark subtraction**: By setting this, the camera obtains dark frames with the shutter closed. The number of dark frames can be selected. After the acquisition, these frames are saved in a specified location. If the dark subtraction was chosen to process the image data, a median

dark will be generated, and it will be subtracted from the image data. This minimizes the effect of bias and also dark noise on the estimation of the centroid shift of the image.

- **Choice of reference position**: The reference position for image motion correction should be selected. The shift in image centroid is measured with respect to this position. Two options are included, one to choose the centroid position of the first frame, and the other, to select the centre of the frame as a reference. The is set to the centre of the frame as a reference. The user input reference position should be within the AoI size.

- **Centroid**: This is the output value of the image position within the frame. This is calculated using the intensity weighted centroid calculation. The weight is based on the threshold of the intensity of the image. The threshold level is chosen slightly above the noise level in the image frame. The centroid coordinates of the image are also displayed in real time.

- **Software PID control**: A software PID control loop was generated for an estimated shift that needs to be taken as input to move the tip-tilt stage actuators. This is discussed in the next chapter. The PID coefficients can also be set up by careful tuning of the operation.

- **Save data**: The control software is programmed to save two sets of data specified by the user. The option include saving the X/Y centroid value of each image or saving the image data directly.

- **Display**: Two graphical windows are provided for live monitoring of the control operation. These windows display the images with specified regular intervals. By default, it was one in 10 frames. The second window displays the live tracking of the centroid of the image. Here, two sets of data plots related to their respective centroid can be seen. The

horizontal axis of the plot window shows the number of data samples and the vertical axis shows the image centroid shift in pixels.

Several output values regarding the loop frequency, *rms* value of the centroid motion, number of frames to read out, control on a closed-loop and open-loop of the operation, etc., are incorporated in the software. The execution of the program is streamlined for its smooth functioning. During the performance of a task, all other user inputs are disabled to avoid the conflicting operation.

3.4.1.4 Possible errors

The software display the errors that can occur during the execution of the program. These errors are broadly divided into initialization errors and operational errors.

The initialization errors can occur either with a camera or the tip-tilt stage, which will be displayed in the error window. The connections to these two systems need to be checked thoroughly before the execution of the program. It is always suggested to switch on these two systems before starting the program and make sure that these are appropriately connected. It is recommended to restart the program if initialization errors (i.e. before applying the correction) have occurred.

The operational errors can occur during the operation of the tip-tilt correction either in an open-loop or in closed-loop operation. One such mistake can be overreaching the minimum or maximum movement of the tip-tilt stage. The minimum and the maximum tilt range in an axis is zero mrad and ten mrad. Any applied movement beyond this range could trigger an error. This error can occur with a miscalculation of the centroid, or if the correction range breaches its limits. It is recommended to stop the program and re-execute if this error has occurred.

3.5 Summary

In this chapter, the design of the optical system of the instrument and its mechanical interface unit were discussed. The instrument was designed as a suitable unit for interfacing with the telescope. The tip-tilt stage, sensing camera and the imaging camera were described. The control software and its execution were explained. Various control inputs and possible errors and their solutions were highlighted. The characterization of the instrument in the laboratory is discussed in the next chapter.

Chapter 4
Characterization of the instrument in laboratory

In this chapter, the characterization of the tip-tilt instrument in the laboratory is discussed. The sub-components of the instrument were aligned on an optical breadboard. The instrument was tested for its performance by artificially creating random image motion. The calibration of the instrument, estimation of image motion, the methodology adopted to induce image motion, and the performance of the tip-tilt operation are described in the following sections.

4.1 Concept of tip-tilt correction

The tip-tilt correction was performed in a closed-loop operation. The schematic of the laboratory set up is shown in Figure 4.1. The tip-tilt stage and the sensing camera were interfaced with a computer, i.e. loaded with tip-tilt control software with a user interface. As discussed in the previous chapter, the software performs the operation of tip-tilt correction in real-time.

The light from laser source was spatially filtered to produce a point source. The tip-tilt mirror was placed in the collimated beam path before the image

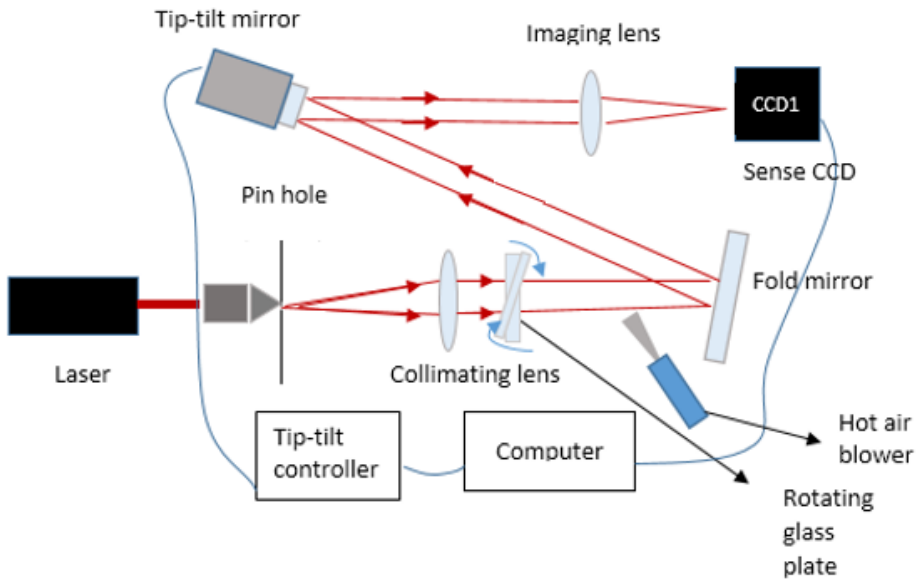

Figure 4.1: Initial phase: Laboratory setup. A point source was created using a 50 μm pinhole. A wedged rotating glass plate and tip-tilt mirror were placed in collimated beam path. The hot air was blown in the path of the light beam. The sensing camera acquired the images.

motion-sensing camera. Randomly induced tilts in the collimated beam path cause shift in images on the camera. The sensing camera continuously captures these images. The image motion is tracked by estimating the centroid of each image. A relative centroid shift between two successive images is calculated, and a necessary amount of tilt is applied to the tip-tilt stage. The mirror mounted on the tip-tilt stage compensates for the tilts to arrest the image motion. Thus image motion is expected to be stabilized. The end-to-end operation of tip-tilt correction is discussed in the following sections.

4.1.1 Estimation of image motion

The sensing camera was operated in high-speed mode ($\sim$ 300 fps) to acquire short exposure images. These images were used to estimate the image motion using a centroid tracking method (Close and McCarthy 1994; Golimowski et al. 1992). The bias counts in the images affects the accuracy of centroid tracking. The images are dark subtracted (which automatically removes bias)

to minimize the effect of bias counts on centroid tracking. The software has the option to acquire the number of dark frames specified by the user. The master dark was obtained by taking the median of the dark frames (10 frames were used) before each experiment. This frame was used for dark subtraction.

The centroid estimation should be faster to minimize the time delay between the sensing of the motion and the correction. For this experiment, we have chosen an intensity thresholding centroid technique. In this method, a threshold slightly above the pixel noise level is applied to the image. Here, we set this threshold as a factor ($\sim$ 0.7-0.9 times) of the peak intensity of the image. The method minimizes the noise by assigning zero counts to pixels below the threshold. The resultant image centroid was measured using the weighted average of the intensities, as shown in Equation 4.1. To estimate the performance of the tip-tilt correction, the root mean square (*rms*) of the residual centroid motion was measured using Equation 4.2:

$$X_c = \frac{\sum x_i I_i}{\sum I_i}, Y_c = \frac{\sum y_i I_i}{\sum I_i}, \tag{4.1}$$

$$\sigma_x = \sqrt{\frac{\sum (X_c - \bar{X_c})^2}{n}}, \sigma_y = \sqrt{\frac{\sum (Y_c - \bar{Y_c})^2}{n}} \tag{4.2}$$

where X_c, Y_c are the estimated centroid of the image, $I_{i,j}$ are pixel intensities, $x_{i,j}$, $y_{i,j}$ are pixel coordinates, $\bar{X_c}$, $\bar{Y_c}$ are mean centroids and σ_x, σ_y are associated standard deviations.

4.1.2 Power spectral density

The power spectral density (PSD) is the measure of energy distributed over a frequency range when the measurements were made within a finite time window (Welch 1967). In this thesis, the PSD of the centroids of tilt uncorrected and corrected images were measured. The comparison between the PSD help in determining the correction bandwidth of the tip-tilt instrument. The correction bandwidth was defined as the least frequency at which the

ratio of the PSD of the uncorrected and corrected data sets falls to unity, i.e., 0 dB.

$$\widehat{x}(f) = \frac{1}{2\pi\sqrt{T}} \int_0^T e^{-2\pi i f t} x(t) dt \tag{4.3}$$

$$S(f) = |\widehat{x}(f)|^2 \tag{4.4}$$

The power spectral density $S(f)$ over limited time interval $[0, T]$ of centroid data $x(t)$ is defined in Equation 4.3, 4.4. Where, $\widehat{x}(f)$ is the Fourier transform of centroid data with temporal frequency f.

4.2 Instrument calibration

The calibration is necessary to accurately map the image wandering on the CCD to the input control voltage that drives the piezo actuators to compensate the image movement across the detector plane. This mapping is unique for each instrument as the linear beam-throw by steering mirror depends on the specific layout of the optical components. The axis of the stage has been centred around half of its maximum dynamic range, i.e. at five mrad. In laboratory a point source is generated by spatially filtering the laser beam. The spatial filter consists of a microscope objective and a pinhole. For performance analysis, the centroid motion of the point source image on the sensing camera has been observed.

4.2.0.1 Axis alignment

Ideally, the movement of the two actuator axis should be perfectly aligned with the pixel rows (horizontal) and columns (vertical) of the CCD (Figure 4.3). Initially, the axis of the tip-tilt stage was coarsely aligned by observing the spot traces in the live camera images. After making the fine adjustments, a residual deviation in alignment was measured by taking multiple images of the source on CCD while the beam was progressively steered (horizontally or vertically) in a sequence of voltage steps applied to individual actuators, one at a time. Furthermore, to minimize the alignment error, a rotation matrix

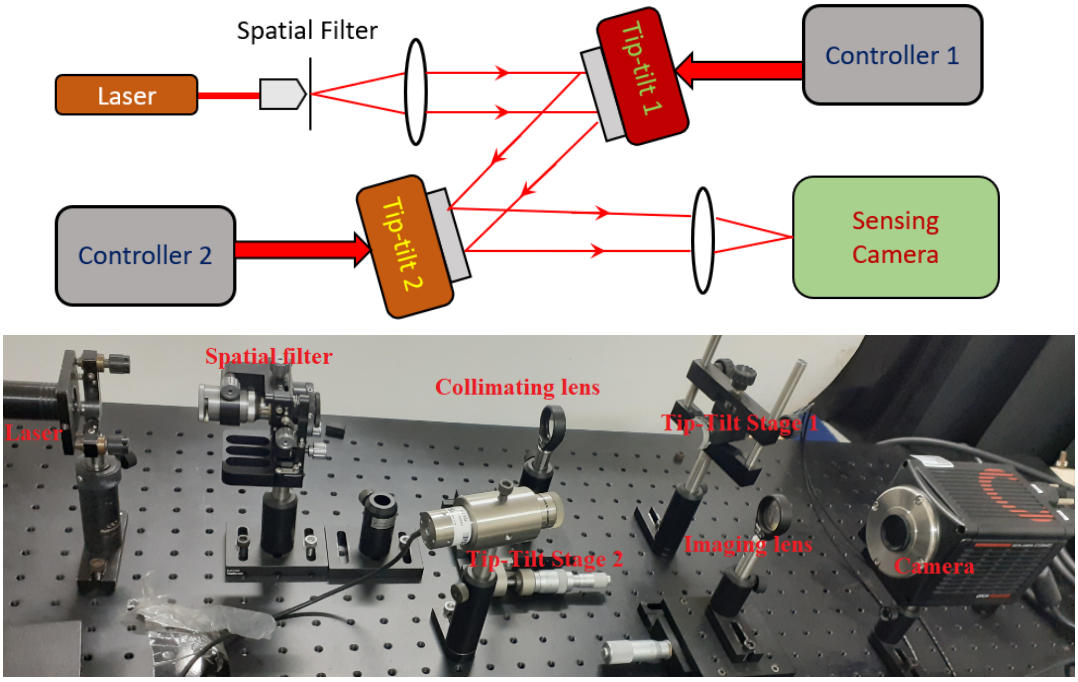

Figure 4.2: Experiment layout for the tip-tilt calibration in the lab. The tip-tilt stage TT1 was used to induce the image motion while TT2 was used to correct it. The CCD camera was used for recording the movement of the laser spot.

(Russell 1971) as shown in Equation 4.5 was generated from the obtained data. To compensate the small offset in the alignment, the shift in the image motion is multiplied with this matrix before applying the corrections in real-time.

$$\begin{bmatrix} x' \\ y' \end{bmatrix} = \begin{bmatrix} a & b \\ c & d \end{bmatrix} * \begin{bmatrix} x \\ y \end{bmatrix} \tag{4.5}$$

$$X' = AX \tag{4.6}$$

$$V = KX' \tag{4.7}$$

Equation 4.6 is the relation between the rotation matrix A and the centroid shifts. In the Equation 4.5, x and y are image centroid shift, x' and y' are centroid shift after rotation along H-axis and V-axis. In our experiment, the measured elements of the rotation matrix (A) were: $a = 1.003$,$b = 0.0013$,

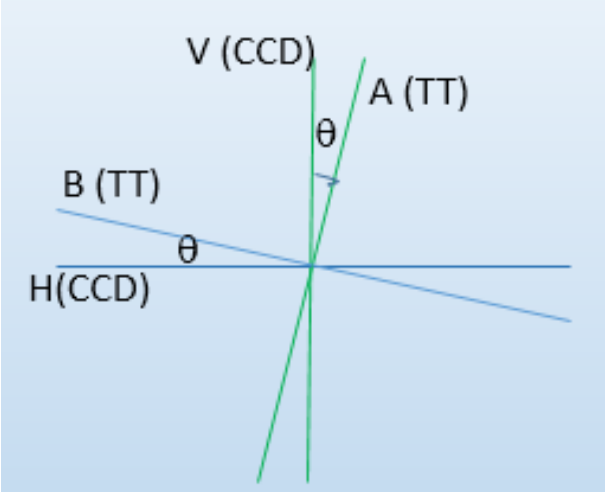

Figure 4.3: Alignment of tip-tilt stage axis with sensing camera axis. V(CCD) and H(CCD) are vertical and horizontal axis of camera, similarly, A(TT) and B(TT) are vertical and horizontal axis of tip-tilt stage. Here, θ is the misalignment angle. With careful calibration for alignment, the value of θ can be made negligible.

$c = 0.0015$ and $d = 0.9996$. These are typical values for a closely aligned system. In Equation 4.7, V is voltage applied to tip-tilt stage and K is the voltage per unit shift in the centroid.

The response of each actuator is tested independently by tilting it over a range of 3 mrad to 8 mrad with an input voltage step size of 1V. The image centroids for each input step voltage is recorded. The mean centroid shift is estimated by measuring the average difference between two consecutive centroids over the earlier mentioned tilt range. Figure 4.4 (top panel) shows the image centroid shift on the camera as a function of input voltage. The error in actuator movement is defined as the difference between two consecutive centroids with respect to the mean centroid shift. It is plotted in the Figure 4.4 (bottom panel). The estimated *rms* error in the actuator movement is less than 0.3 μm. Results of tip-tilt stage calibration are summarized in Table 4.1.

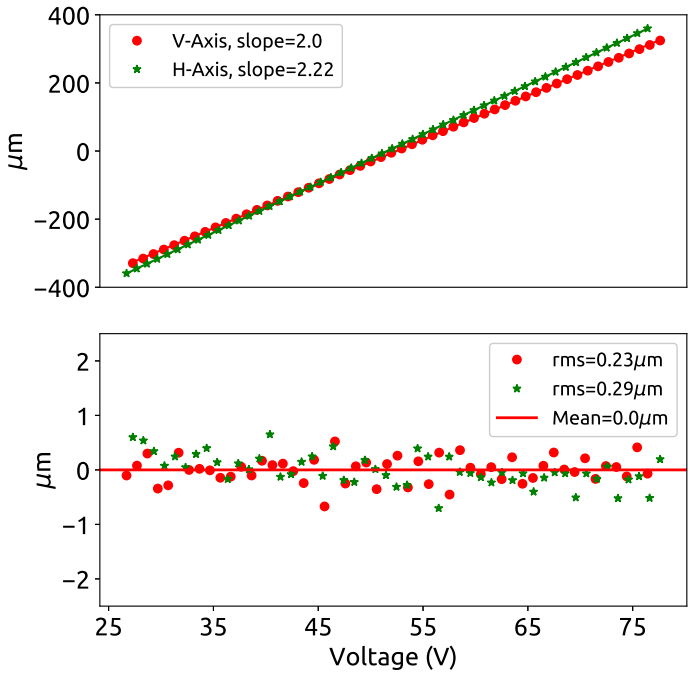

Figure 4.4: Calibration curves for two-axis tip-tilt stage. The horizontal (H-axis), vertical (V-axis) have been moved with equal step size of 1 V (top). The error in actuator movement for the fixed input voltage step size (1 V) is mentioned in bottom panel. In both axes, the rms deviation from the linear fit is ~ 0.3 μm.

Table 4.1: Tip-tilt stage axis calibration

Parameter	Value
Number of samples	51
Exposure time per sample	3 ms
Tip-Tilt range	3-8 mrad
Voltage range	24-78 V
Voltage step size	$\sim$ 1V
Linear image shift (total)	$\sim$650 μm
Mean centroid shift	$\sim$ 12 μm
rms error in movement	$\sim$ 0.3μm

4.3 Laboratory testing

The concept of tip-tilt correction was tested by creating different real-time conditions. The image motion was artificially created by two different mechanisms. At the initial phase, we used a wedged glass plate along with hot air blower to produce a random image motion. The wedged glass plate creates a periodic image motion. This method, however, doesn't quite mimic the conditions of the atmosphere.

In the second method, we obtained centroid data from a time series of (short exposure) star images observed with the telescope. This data was then inverted to piezo voltage which drives the tip-tilt stage to reproduce the image motion. For this purpose, one of the tip-tilt stages was used to reproduce image motion. The laboratory setup is shown in Figure 4.2.

In this section, the mechanism to induce image motion and the results achieved with the tip-tilt correction are discussed. The performance of the tip-tilt correction was evaluated by estimating the reduction in *rms* value of image centroid motion. The correction bandwidth was measured from using the powers spectral density of the image centroid motion.

4.3.1 Initial phase

In the initial phase, the instrument was tested by inducing image motion using a wedged glass plate in a combination of a hot air blower. In this phase, we used a Pulnix CCD as sensing camera. This camera has a maximum frame rate of 100 per second. The maximum achievable loop frequency was ≤ 100. Laboratory experiment setup is shown in Figure 4.1.

In the layout, a wedged rotating glass plate was placed in the collimated beam path, and it was mounted on a rotor stage. A rotating glass plate in the beam path induces a tilt in the wavefront. This tilt causes an image motion in the focal plane. The cyclic rotation causes a periodic image shift. The hot air blown in the beam path randomizes the image motion. A sensing

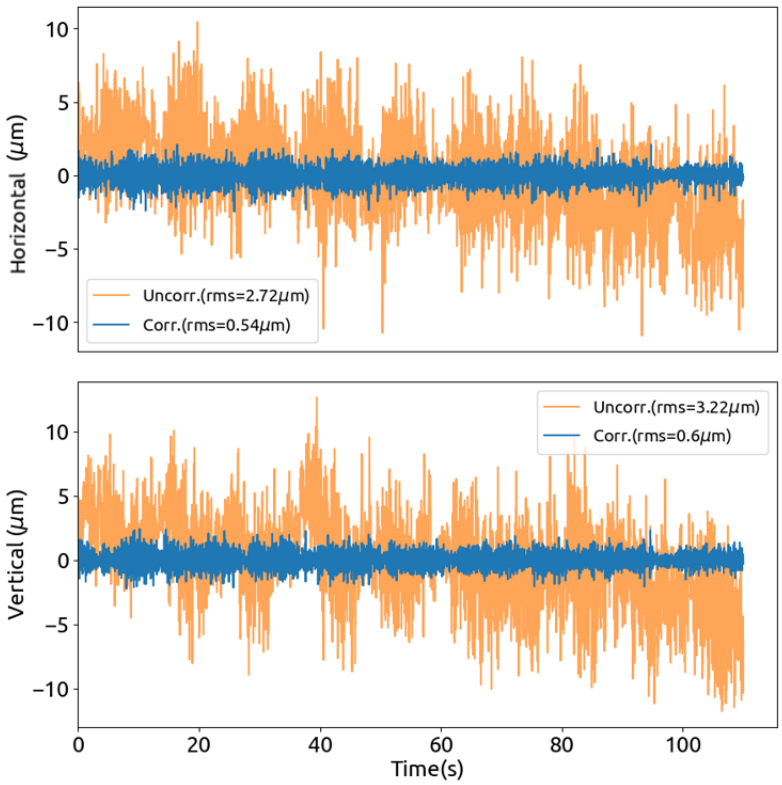

Figure 4.5: Initial phase: Image centroid motion correction for glass plate induced distortions.

camera continuously acquired the images. The control software measured the instantaneous centroid shift and applied correction using the tip-tilt stage in real-time.

Figure 4.5 show the centroid motion of tilt uncorrected and corrected images. The image motion was measured along the Horizontal axis (H-axis) and Vertical axis (V-axis) in in μm units on the sensing camera. The *rms* value of image centroid motion was reduced by a factor of ≈ 5.3. The PSD of the centroid motion is shown in Figure 4.6. The PSD was calculated for the absolute motion of image centroid. From the analysis of this data, a closed-loop correction bandwidth of ≈ 6.4 Hz was determined.

We have achieved a satisfactory performance of the tip-tilt instrument using a wedged glass plate in combination with a hot air blower. Even though it could attain anticipated performance, we thought to test the instrument on more realistic conditions by creating image motions similar to on telescope

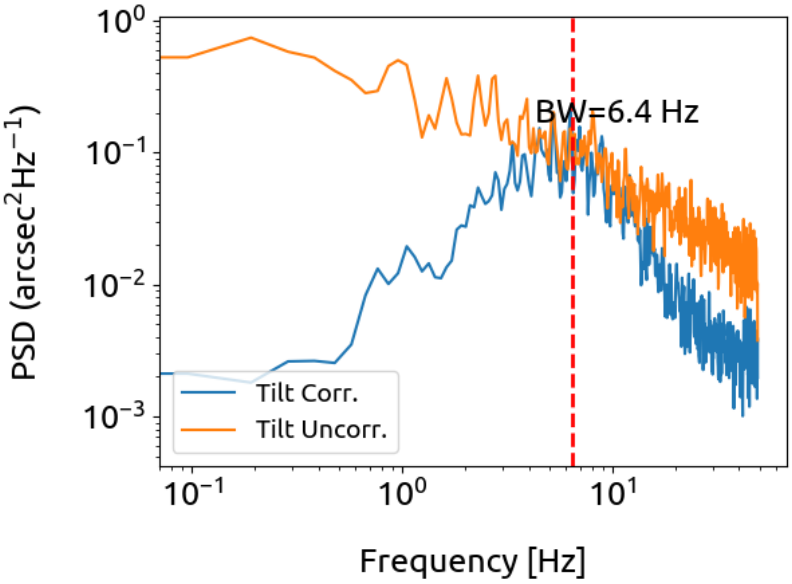

Figure 4.6: Initial phase: The power spectral density of centroid data in laboratory. The vertical line signifies the merging of the two plots. This is the 0 dB closed loop correction bandwidth (red line) of the system.

site. Again, the low frame rate of the Pulnix CCD[1] has a limitation on the loop frequency of tip-tilt operation. We addressed this problem in the subsequent phase of instrument performance analysis.

4.3.2 Using star image centroid data

The image motion recorded on the telescope site is more realistic as it contains both spatial and temporal spectral information of the turbulence. Thus it was preferable to use it for characterizing the performance of the instrument in the lab. To improve loop frequency, we used an Andor Neo sCMOS camera. This could give a maximum loop frequency of $\sim$ 300 Hz. The prototype of the instrument was set up in the laboratory, as shown in Figure 4.2. The image motion data obtained from a telescope was then used as input to one of the steering mirrors to simulate the image motion in the lab studies. For characterization of the instrument, the residual image centroid motion and the PSD of tilt uncorrected and corrected images were analyzed.

[1]http://www.ccdworld.com/products/pulnixjai-ccd/

The layout of the laboratory setup is shown in Figure 4.2. In this study, we used two tip-tilt stages -one to induce the image motion (Piezosystems jena[2], Model Number: PSH x/2); and the other to correct it. The former has the frequency response up to 3 kHz, 0.02 μrad resolution and $\pm$4 mrad dynamic range.

The centroid data (in pixels) need to be converted to the voltages which will be applied to the tip-tilt stage 1 (TT1). For this purpose, the per-pixel voltage (0.21 V for H-axis and 0.23 V for V-axis) is estimated for the TT1 system from the calibration curves. The voltages were applied to TT1 to induce the image motion at the frequency of 33 Hz. This is to maintain at least ten times the correction bandwidth (Hardy 1998) of the system. The induced image motion is tracked using the centroid estimations.

The image motion data was recorded both with and without the tip-tilt correction. Figure 4.7 shows the image centroid motion in the laboratory. The *rms* of corrected image motion is reduced by a factor of $\sim$ 12.8 in the Horizontal axis and $\sim$ 9.8 in the Vertical axis, compared to the uncorrected.

The closed-loop correction bandwidth of the system was estimated from the power spectral densities of the image motions for both the tilt uncorrected and corrected cases. The observed correction bandwidth (0 dB)is $\sim 25Hz$.

4.3.3 Effect of software PID control

For optimal performance of the instrument in closed loop, a PID controller was implemented in software. The software PID control is an addition to the in-built PID loop of tip-tilt control unit. Here, we discuss the performance of the system with respect to software PID control.

$$\Delta c(t) = K_p e(t) + K_d \frac{de(t)}{dt} + K_i \int_0^{t'} e(t')dt \tag{4.8}$$

[2] *https : //www.piezosystem.com/*

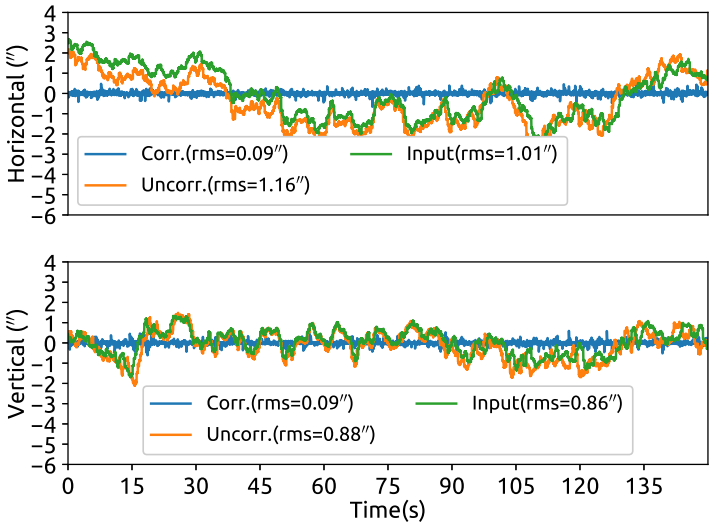

Figure 4.7: Image centroid motion in arcsec (″) along horizontal (top panel) and vertical (bottom panel) axis of the camera. The plot has three sets of data i.e. the induced image motion, the uncorrected image motion and the corrected residual image motion. The induced and the sensed image motion has $\sim 96\%$ correlation. The image shift is converted to arc-seconds by multiplying the image shift with pixel scale of the telescope (0.06″).

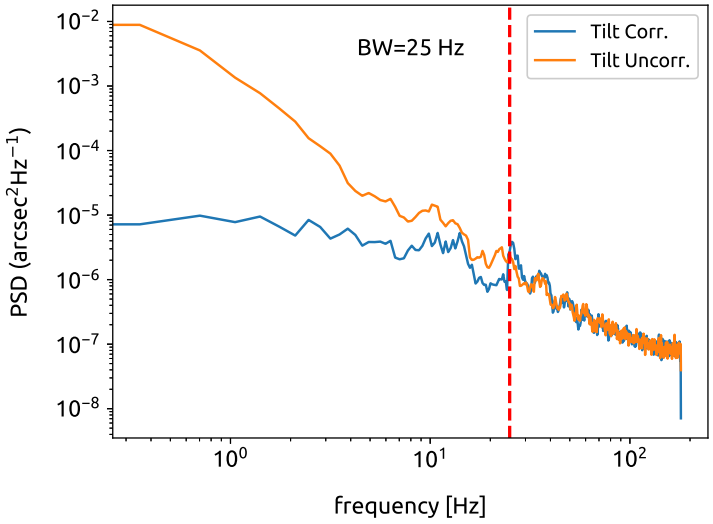

Figure 4.8: The power spectral density of centroid data in laboratory. The vertical line signifies the merging of the two plots. This is the 0 dB closed loop correction bandwidth (red line) of the system.

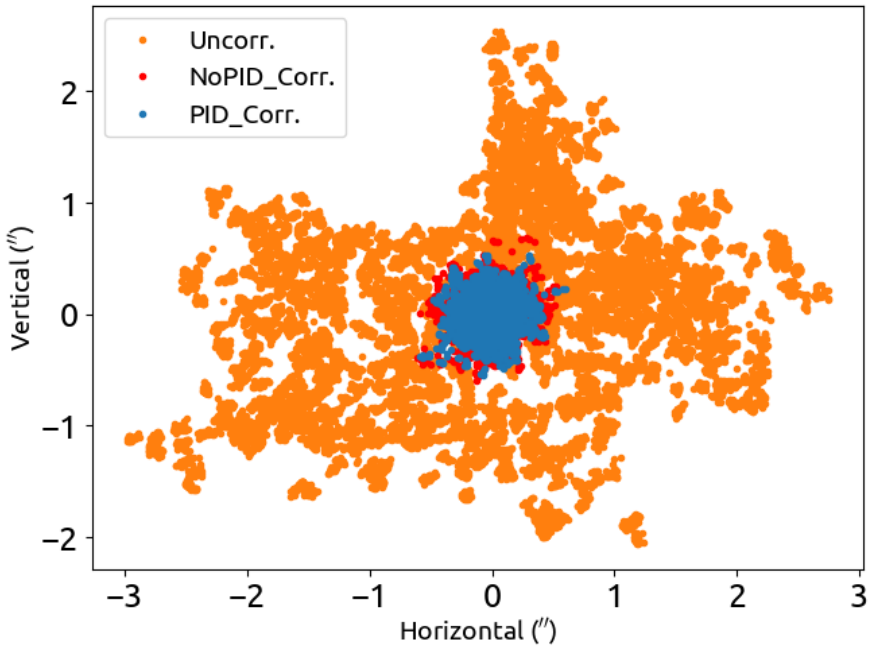

Figure 4.9: Lab: Image motion centroid scatter plot. The legends depict only software PID control.In case of *uncorr*, the tip-tilt correction was OFF. In *No_PID* case, the internal PID was ON and in case of *PID_corr* the software PID along with internal PID was ON. The PID control could reduce the *rms* centroid motion by 12%.

In the above equation, K_p, K_d and K_i are proportional, derivative and integral gains and $e(t)$ is the difference of two consecutive centroid shifts, $\Delta c(t)$ is the centroid shift estimated using the PID control. The controller gains are calculated using trial and error method by monitoring the residual image centroid motion. The estimated values for K_p, K'_d and K'_i are $4{*}10^{-1}$, $2.5{*}10^{-1}$, $2.3{*}10^{-3}$ respectively. Here, K'_d and K'_i are $K_d * T$ and K_i/T, where T is time interval between two consecutive centroids. The $\Delta c(t)$ is multiplied by voltage required to cause a pixel shift. Figure 4.9 shows the scatter plot of image centroid data. The scatter plot has image centroid data of tilt uncorrected, corrected with and without PID control. The implementation of software PID control was able to reduce the *rms* image motion by an additional $\approx 12\%$.

4.4 Summary

In this chapter, we have discussed the laboratory characterization of the instrument. The concept of tip-tilt correction is tested on two different conditions. The performance of the instrument is satisfactory with the simulated image motion in the laboratory. The *rms* value of image centroid motion was reduced by a factor of $\approx$ 12.9 in the Horizontal axis and by a factor of $\approx$ 9.8 in the Vertical axis. The instrument was then ready to be tested on the telescope. In the next chapter,the performance on the telescope is discussed.

Chapter 5

On-sky performance

After the laboratory characterization of the tip-tilt AO instrument, the system was aligned in the laboratory and commissioned on the JCB telescope at VBO. The instrument was tested on multiple targets and its performance was evaluated. In this chapter, the observation methodology, instrument performance on different targets and loop frequency are discussed. Further, the gain in angular resolution is quantified and compared with theoretical predictions.

5.1 Tip-tilt correction system

The layout of natural guide star tip-tilt correction system is shown in Figure 5.1. This system has a tip-tilt stage with a mirror mounted on it. In response to changing conditions, the tip-tilt controller commands the actuators to keep the stellar beam locked to a fixed reference position in the image plane on CCD.

Several tip-tilt systems have been developed in the past(Glindemann et al. 1997; Racine and McClure 1989). A tip-tilt system at Calar Alto 3.5 m telescope, e.g., has shown image motion reduction from $\sim \pm 0.4''$ to $\sim 0.03''$ with 30-100 Hz loop frequency (Glindemann et al. 1997). This alone could yield

a significant improvement in image resolution. A proper exposure time of a tip-tilt sensor is crucial to optimize the performance of the instrument (Martin 1987). For example, Glindemann (1997) has shown that to track/correct an image motion with 5-10 Hz bandwidth, a loop frequency of 50 -100 Hz is required. Close and McCarthy (1994) have developed a Cassegrain secondary tip-tilt AO. They have reported a three-fold reduction in image motion at 72 Hz loop frequency. Furthermore, Golimowski et al. (1992) have used an image motion compensation system for high-resolution stellar coronagraphy. The instrument is reported to have achieved a resolution gain by a factor of 2.2. It enabled the observations of two magnitudes fainter objects than what was achieved without the image stabilization.

The earlier literature emphasis on reducing *rms* image motion by improving the loop frequency of instrument operation. Natural guide star adaptive optics are light starving systems. There is an inverse trade-off between the loop frequency and the exposure time. For instance, shorter exposure require brighter targets and vice-verse. Thus, loop frequency is dependent on the star magnitude, camera readout time, data processing time etc. Our tip-tilt system could operate at loop frequency $\approx$ 300 Hz with a frame size of 128×128 pixels. Table 5.1 shows the chosen set of targets with magnitude(m_v) varying from -0.05 to 5.99 . These objects were observed with a suitable loop frequency (47-290 Hz) considering the signal to noise ratio of image on sensing camera.

In Section 5.2, the on-sky performance of the instrument is discussed. This section briefly describes observations, performance of the instrument with respect to reduction in *rms* image motion, PSD, improvement in angular resolution, improvement in peak intensity in correlation with loop frequency and comparison of angular gain between the theoretical estimation and from the observed data and the performance of the instrument on fainter targets. Finally, in Section 5.3, results are summarized.

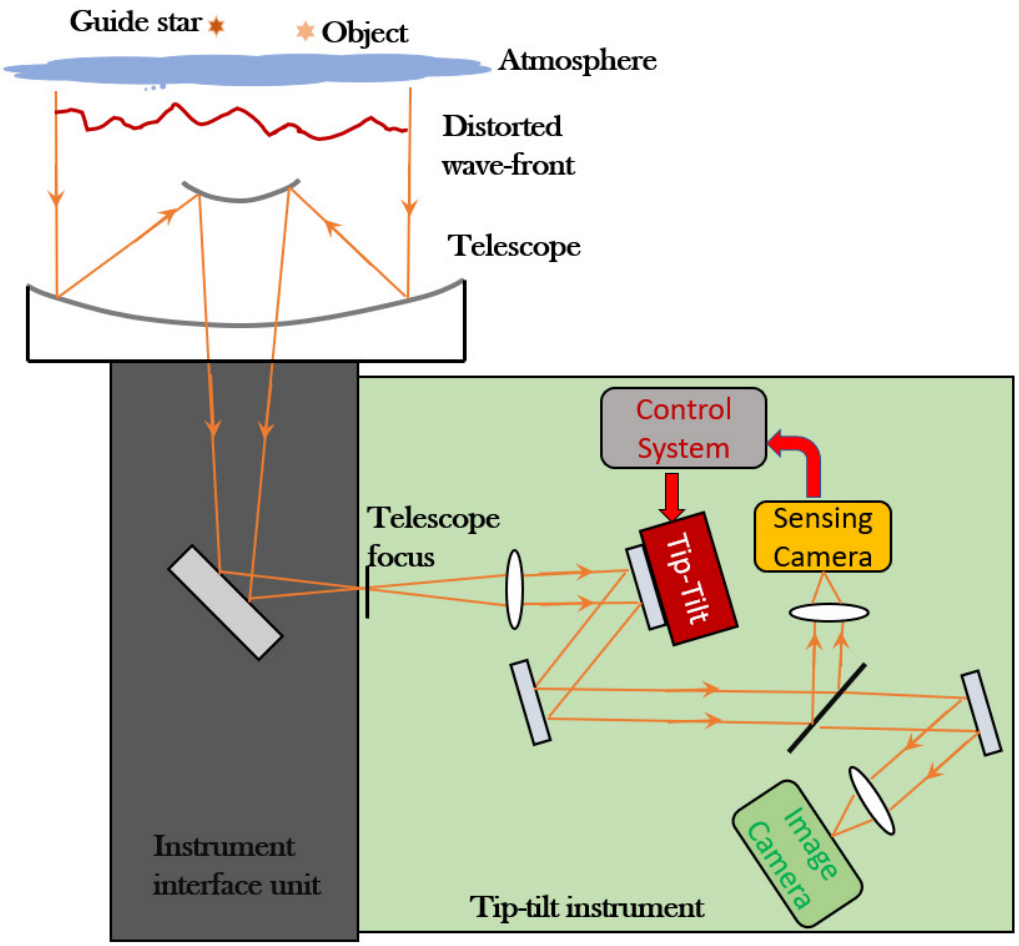

Figure 5.1: Conceptual layout of a natural guide star tip-tilt correction system. The telescope primary mirror collects the light from a target field. The light beam is directed to tip-tilt instrument. The light is divided between the sensing arm and the imaging arm of the instrument. The image motion is corrected in common path where the tip-tilt stage is placed. The corrected wave-front can be directed to imaging camera or a science instrument.

5.2 On-sky testing of the instrument

The tip-tilt instrument was carefully aligned in the laboratory before it was commissioned on the West port of the telescope (see Figure 5.2). Before starting of observation, the light beam from the telescope needs to be deflected to the West port. The offset in guiding the beam into the instrument needs to be taken care. After that, a carefully aligned sub-components guide the star light to the sensing and the imaging cameras. The cameras need to be located at their respective focal planes. Commonly occurring focus error can be corrected by adjusting the secondary mirror of the telescope. For fine-tuning of the focus, each of these cameras as placed on stage with micro actuators. These stages have a linear motion along the optical axis with a resolution of 10 μm within a range of 1 cm. After the alignment, the instrument needs to be enclosed before the observation to prevent stray light.

The on-sky performance of the tip-tilt system is described in terms of the residual *rms* image motion, correction bandwidth, full width half maximum and peak intensity of the image. Although the instrument was tested successfully in March 2018, it needed fine-tuning which we did during 2018-19. Here, we are presenting the results after a satisfactory performance has been achieved during March-May 2019 observational run.

5.2.1 Observations

The objects of visual magnitude brighter than six were chosen. These objects were observed when close to the zenith with hour angle less than one hour. Whenever possible, targets with more than one object in the field were chosen. This enables the instrument to sense the bright star with high-speed and apply the correction to the entire field. List of the targets used is given in Table 5.1.

For high-speed performance, a region of interest (ROI) has been chosen around the target image on sensing camera. This enhanced the frame rate,

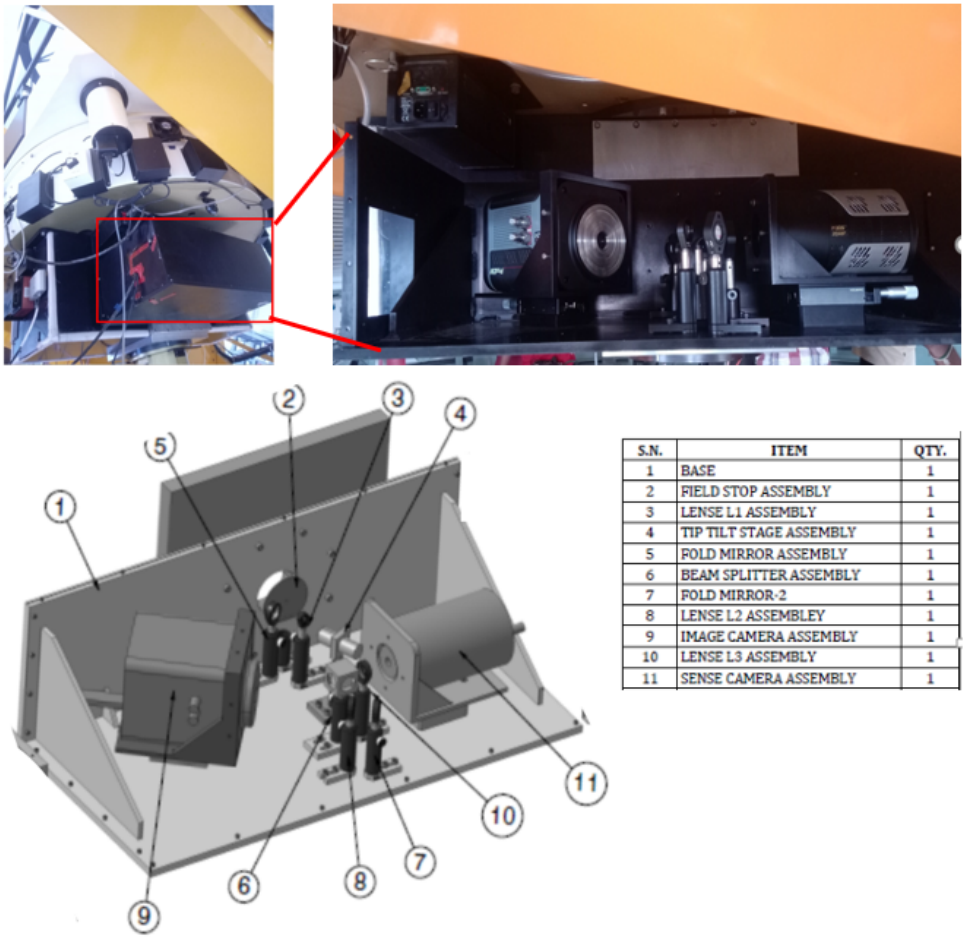

S.N.	ITEM	QTY.
1	BASE	1
2	FIELD STOP ASSEMBLY	1
3	LENSE L1 ASSEMBLY	1
4	TIP TILT STAGE ASSEMBLY	1
5	FOLD MIRROR ASSEMBLY	1
6	BEAM SPLITTER ASSEMBLY	1
7	FOLD MIRROR-2	1
8	LENSE L2 ASSEMBLEY	1
9	IMAGE CAMERA ASSEMBLY	1
10	LENSE L3 ASSEMBLY	1
11	SENSE CAMERA ASSEMBLY	1

Figure 5.2: Tip-tilt instrument mounted on telescope (top-panel). It is shown in red colour window. The bottom-panel is mechanical design of the instrument.

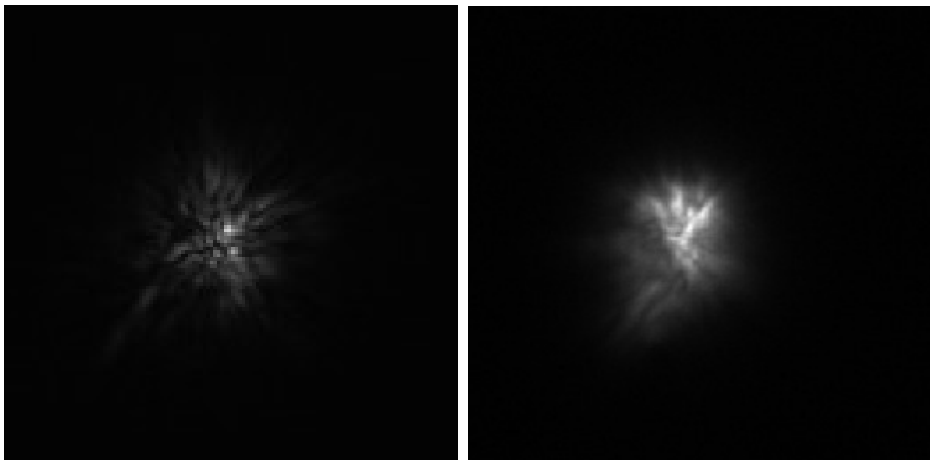

Figure 5.3: Stellar object: HIP57632. The short exposure time (3 ms) image on sensing camera (left). Relatively long exposure time (200 ms) image on the imaging camera. The frame size is $\sim 10'' \times 10''$.

and thus increased the overall loop frequency. The exposure times were selected from 3 ms to 20 ms. The longer exposure time allows us to observe the relatively fainter targets. This enables us to vary a loop frequency from $\sim$ 290 fps to 47 fps. Each data set was recorded over 150 seconds. Under poor atmospheric conditions, the binning operation was carried out in the program to enhance the signal to noise ratio. This might have reduced the accuracy in centroid estimation, but overall, it improved the correction performance.

The tilt corrected images were acquired on imaging camera. This camera was given relatively longer exposure time($\sim$200 ms). Because of a set of objects with different magnitude, we chose a fixed exposure time to avoid pixel saturation in case of a brighter object. In Figure 5.3, the short exposure image of sensing camera and the imaging camera are shown.

A total of 1000 images of each target field were acquired on the imaging camera. Every target was observed for tilt uncorrected and corrected images (closed-loop). These images were processed using a Python script. The image frames have been dark subtracted and flat fielded before the analysis. The co-added short exposure images, as shown in Figure 5.4 (top panel) will amounts to a long exposure image. Finally, these images were divided by the number of obtained frames. It will average the intensity of each frame and minimize the effect of intensity fluctuations on the estimation of the performance. In

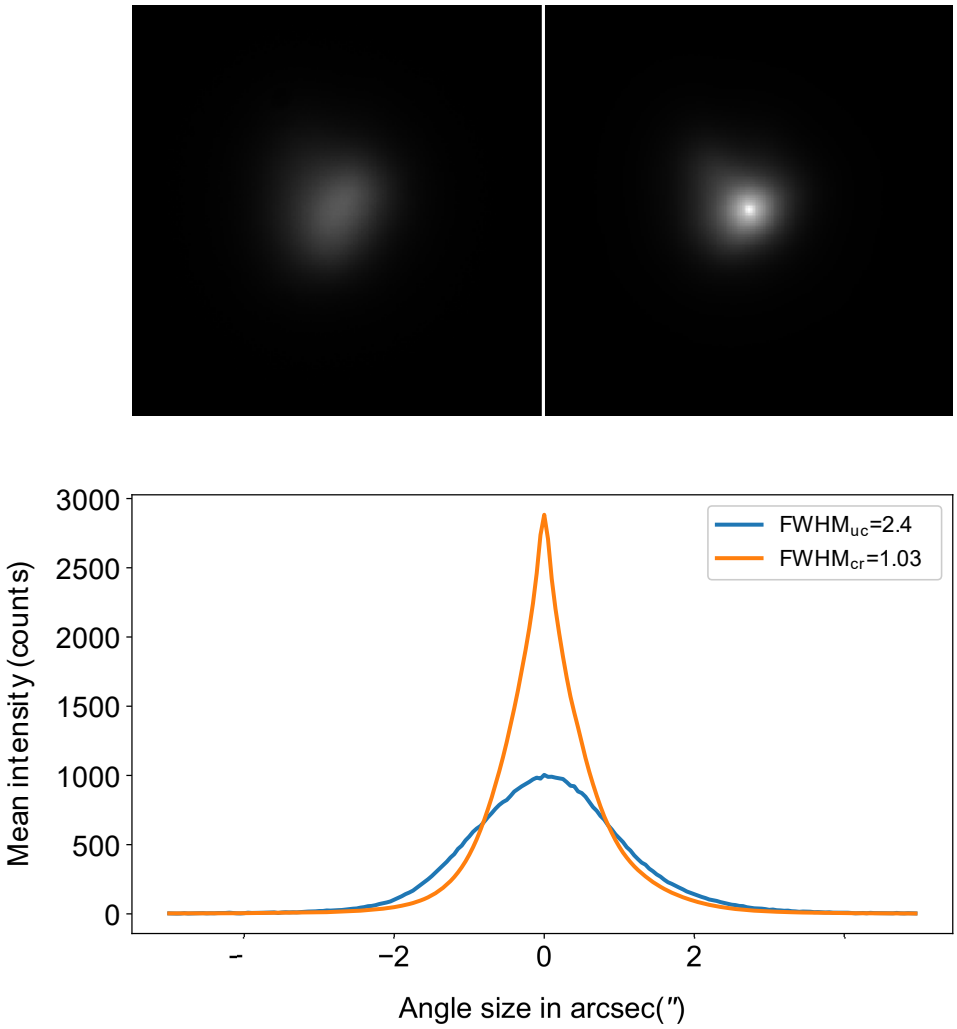

Figure 5.4: Observation of star HIP57632. The tilt uncorrected (top-left) and the tilt corrected (top-right) co-added images. The PSF of the image along the horizontal axis is shown in the bottom panel.

Figure 5.4, the plot in the bottom panel shows the horizontal line-cut of the tilt corrected and uncorrected PSF. The total star energy recorded by CCD camera (area under each curve) for a given explore remain almost same for both the cases. In case of blue curve, intensity is distributed in wings. After correction this intensity is pushed towards the core of the PSF.

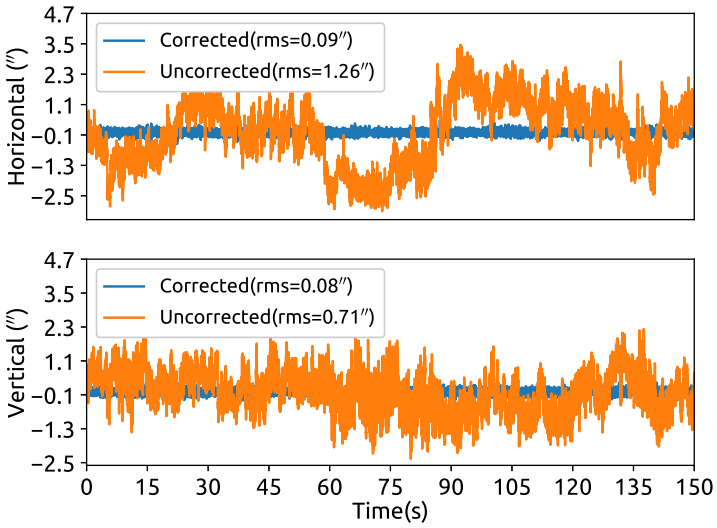

Figure 5.5: Image centroid motion of HIP57632. The rms image motion has been reduced by a factor of $\sim$ 14 in horizontal axis and $\sim$ 8.9 in vertical axis.

5.2.2 Image centroid, PSD and PSF comparison

The instrument was characterized by measuring the residual image motion. Figure 5.5 shows the tilt-corrected and uncorrected image centroids recorded consecutively by sensing camera. The rms value was reduced to $\sim$0.08″ from $\sim$1.26″.

The image motion power spectral density is shown in Figure 5.7. The correction bandwidth of the system is found to be $\sim$26 Hz, depicted with a vertical line in the figure. The temporal frequencies beyond this limit are uncorrected. The high-frequency side of PSD is noisier. The correction bandwidth of the system is computed by calculating the ensemble average of the PSD.

On imaging camera, the point spread function (PSF) is expected to be sharper with the tip-tilt instrument in operation. Figure 5.4 shows the PSF of HIP57632. The full width at half maximum (FWHM) of the PSF has improved from 2.4″ to 1.03″. The improvement in FWHM was calculated, as shown in Equation 5.1. It is a $\sim$ 57% improvement. Figure 5.6 show the scatter plot of image centroid motion along the two orthogonal axes of the sensing camera. The centroid motion is mentioned in arc-seconds. The

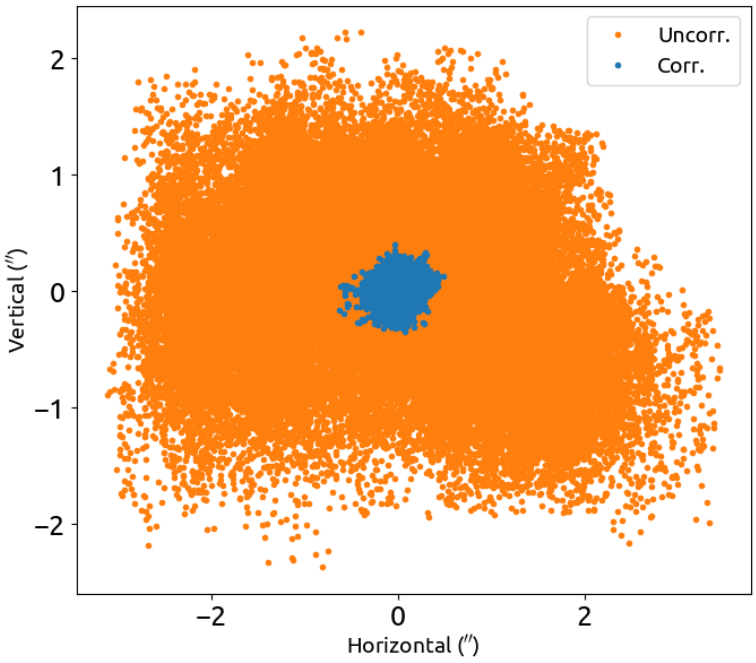

Figure 5.6: On-sky:Image motion centroid scatter plot of object HIP57632. A total of 15000 centroid data points were plotted for uncorrected and tilt corrected data.

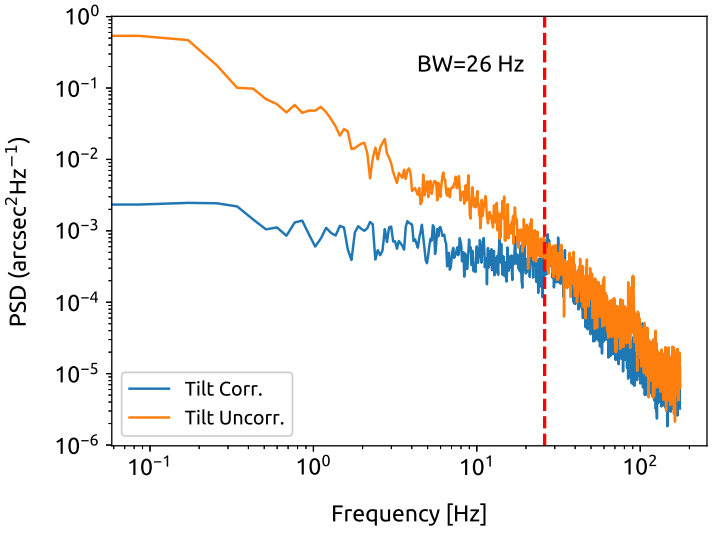

Figure 5.7: The power spectral density of the image motion for star HIP57632. Vertical dotted line demarcates the close-loop bandwidth of the system.

centroid motion of the tilt corrected images is overplotted on the uncorrected centroids. The image motion is compressed to few arc-seconds.

$$Improvement(\%) = \frac{FWHM_{uc} - FWHM_{cr}}{FWHM_{uc}} \times 100 \tag{5.1}$$

Here, $FWHM_{uc}$ is for uncorrected image and $FHWM_{cr}$ is for corrected image.

In the above case of HIP57632, the peak intensity of tilt corrected PSF has increased by a factor of ~ 2.8. It improves the sensitivity of the instrument towards the observation of a fainter object. The sensitivity was estimated by using the Equation 5.2. This equation relates to the magnitude difference of a star with a peak intensity of the tilt uncorrected and corrected images.

$$\Delta m_v = -2.512 \log_{10} \left[\frac{I_c}{I_{uc}} \right] \tag{5.2}$$

Where, I_c/I_{uc} is the ratio of peak intensities of tilt corrected and uncorrected images, Δm_v is the improvement in apparent magnitude. Here, we considered, I_c/I_{uc} as 4.3/1.49. We find that the sensitivity is improved by a factor of 1.1 in magnitude.

5.2.3 Effect of loop frequency

The optimal frame rate is essential for the active tilt correction of the images in a closed-loop operation. It is consistent with the fact that the wave-front distortions are caused by the spatial and the temporal disturbances in the atmosphere. The spatial deformities are corrected by compensating for the shift in the image centroid. But the dynamic nature of the atmosphere induces high-frequency image motion. To overcome this effect, the time delay between the instant of estimation of the shifts and the instant of the correction applied to the corrector should be kept a minimum.

To study the effect of loop frequency on the peak intensity of the tilt-corrected images, we observed HIP57632 with different frame rates. The

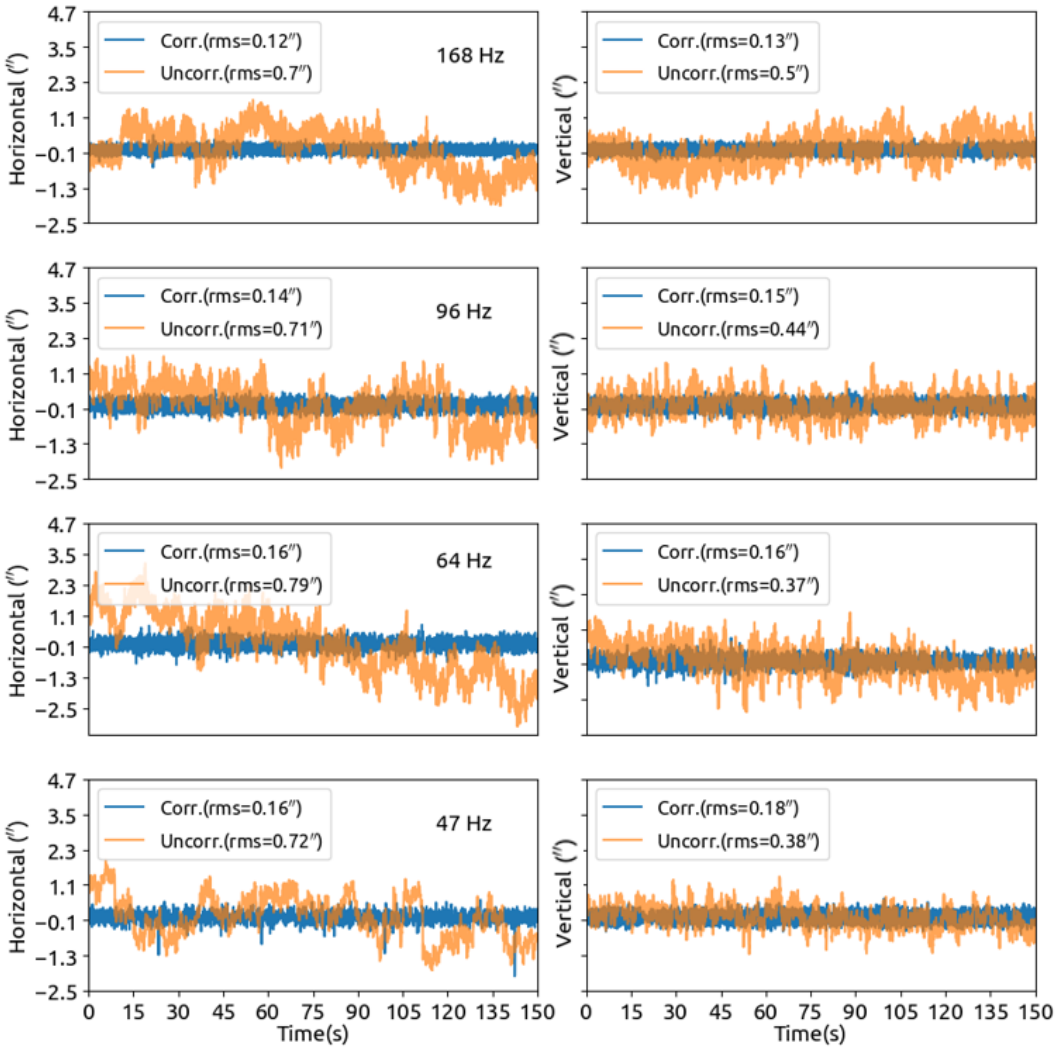

Figure 5.8: Comparison of image centroid motion for different loop frequencies. Four different loop frequencies are labelled. The image centroid motion is plotted along the Horizontal (left) and Vertical axis(right) of sensing camera. The tilt uncorrected and corrected *rms* value is labelled in respective plots.

frame rate was changed by changing the exposure time of the sensing camera from three to 20 ms, yielding loop frequencies of 290 to 47 Hz.

Figure 5.8 show the image centroid motion for different loop frequencies (LF). The LF is varied, as mentioned earlier. The observational data is obtained for star HIP 57632, and each of the observations for different LF has taken $\sim$ 10000 centroid data points. Two sets of data, one for uncorrected and the other for corrected, for the same loop frequency. The rms image centroid has been reduced significantly with increased loop frequency.

In Figure 5.9, cross-section of the PSFs with different loop frequency are

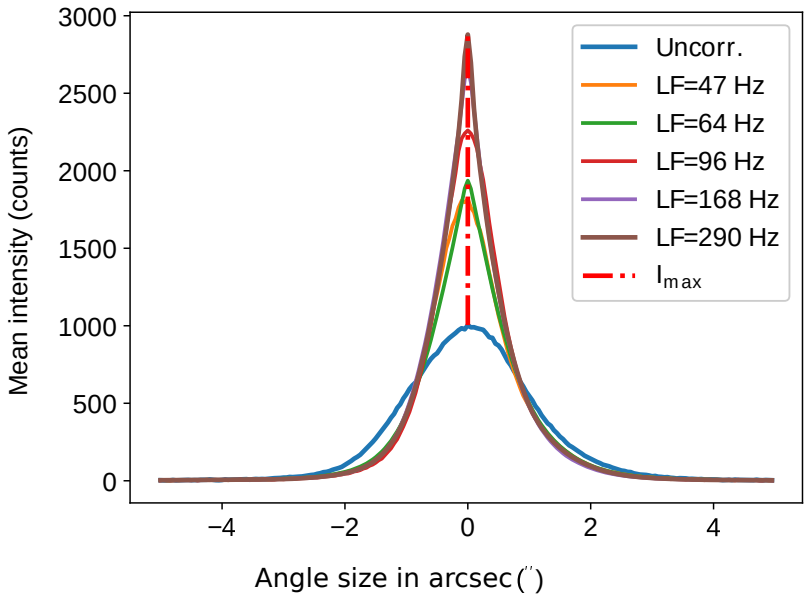

Figure 5.9: Comparison of tip-tilt corrected PSF of HIP57632 for different loop frequencies. The peak intensity is showing logistic growth with loop frequency.

plotted. The peak intensity of the PSF was increased with an increase in loop frequency, and the result is plotted in Figure 5.10. In this figure, the peak factor was defined as the ratio of the peak intensity of tilt corrected to that of the uncorrected image.

We have modeled the effect of loop frequency on peak factor with a function of the form shown in Equation 5.3.

$$I_{pf}(f) = K_1 + K_2 * (1 - e^{-f_0/f}) \tag{5.3}$$

In the above Equation 5.3, f is loop frequency, I_{pf} is peak factor and the estimated constants are K_1, K_2 and f_0 estimated to be $\approx$ 3.2, -2.2 and 52 Hz, respectively. The units of K_2 and K_1 are similar to I_{max}. Arguably, the estimated values of the constants depend on the target intensity and the atmospheric seeing conditions.

In Figure 5.11, the power spectral densities for different loop frequencies are shown. We can see that that the correction bandwidth increased to $\sim$ 26 Hz at 290 Hz from $\sim$ 4.8 Hz at 47 Hz loop frequency. On average, the

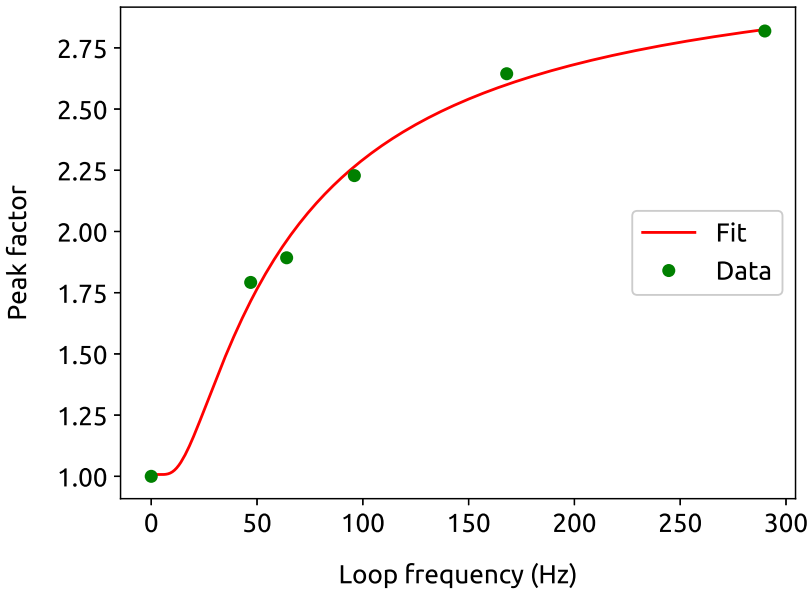

Figure 5.10: Increment in peak factor with loop frequency.

correction bandwidth is $\sim 1/10$ of the loop frequency, which is in agreement with other studies reported in the literature (Hardy 1998).

5.2.4 Gain in angular resolution

The tilt corrected images show improvement in angular resolution. The gain in angular resolution is a function of relative sizes of the telescope aperture (D) and the atmospheric coherence diameter r_0. This relation can be theoretically estimated using the formalism given by Roddier (1981a) and is shown in Figure 5.12. The gain is defined as the ratio of equivalent width (Roddier 1981a) of tilt uncorrected image and corrected images. The observed values of the gain for a set of six targets listed in Table 5.1 are overplotted on the theoretical curve. r_0 is estimated from the equivalent width of the uncorrected images (to get the D/r_0 for the observed data). The observed gain has shown a deviation of up to 24% from the theoretical gain.

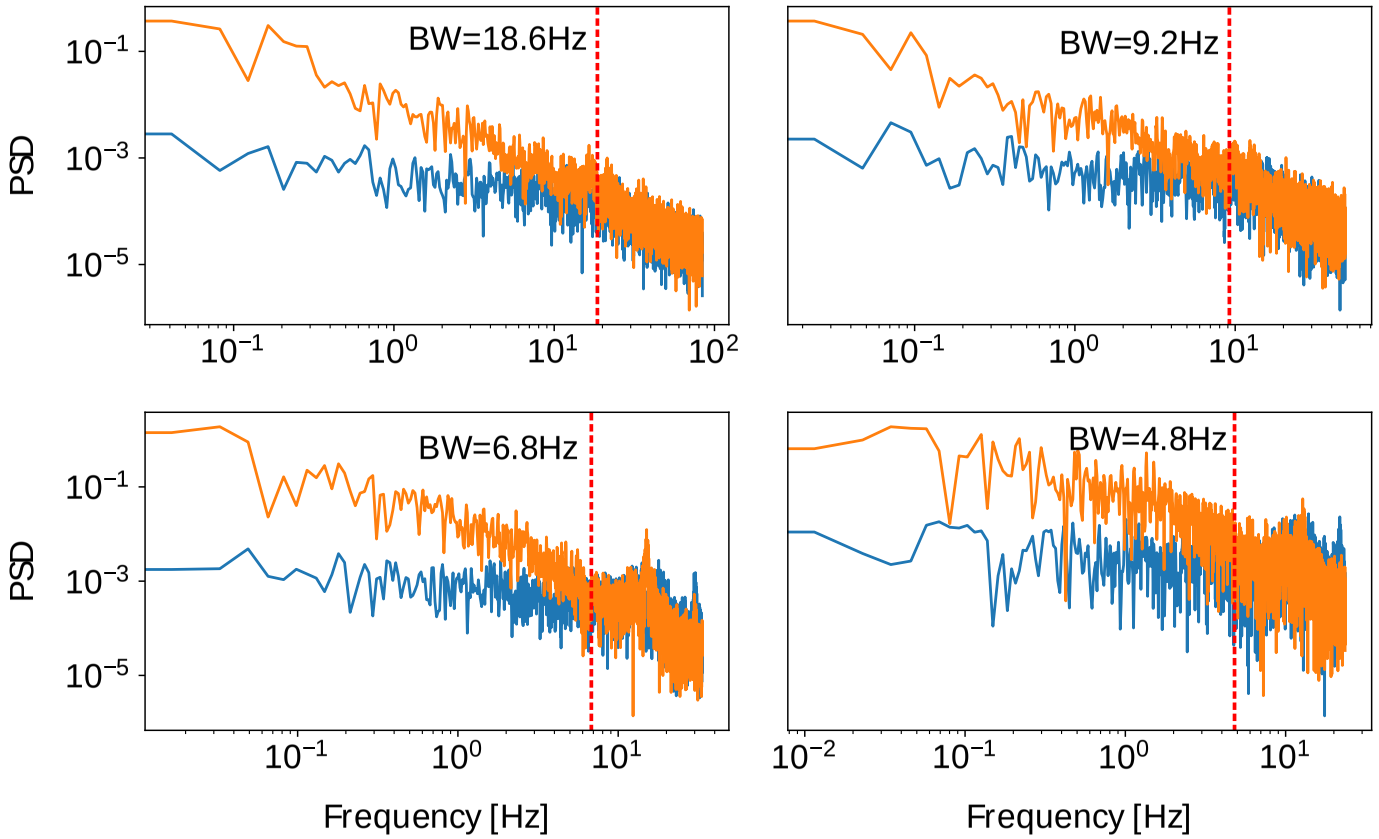

Figure 5.11: The PSD (arcsec^{2}Hz^{-1}) with respect to correction bandwidth for object HIP57632. The orange and the blue lines are PSD of tilt uncorrected and corrected centroid data. The loop frequency is 168 Hz (left) and 96 Hz (right) for top row, 64 Hz (left) and 47 Hz (right) for bottom row and their correction bandwidths (red line) are in the plot.

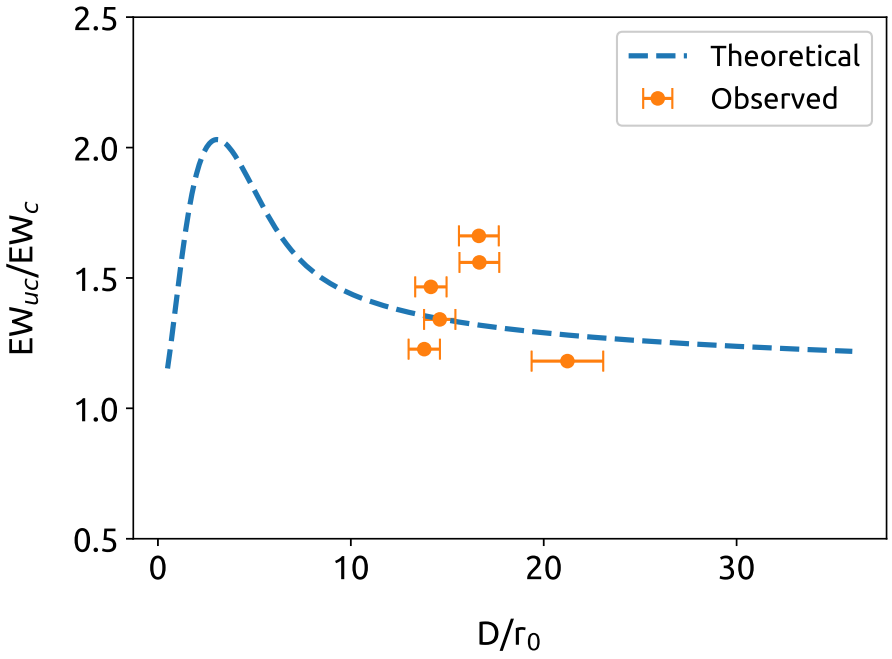

Figure 5.12: Comparison of gain in angular resolution between the theoretical and the observed data. In this figure, EW_{uc} and EW_c are equivalent widths of tilt uncorrected and corrected image.

5.2.5 Performance of the instrument on faint targets

A set of seven objects listed in Table 5.1 (objects 7-13) were observed to validate the increase in sensitivity of the instrument due to image stabilization. Usually, a bright star near a faint star was used for sensing the image motions, and the same correction was applied to the entire field. If the faint star is close enough, the corrections were similar and thus the sensitivity of the instrument on the faint star increases.

In Figure 5.13 the tilt uncorrected and corrected image of HIP50583 shown. The object has a brightness of 2.37 in magnitude with a relatively fainter object with v-magnitude of 3.47, at an angular separation of 4.63″. The correction increased the peak intensity by a factor of $\sim$ 2.5 times in brighter object $\sim$ 2.1 times in fainter object. The angular resolution (FWHM) of these objects improved by 52% and 46% respectively. Similar to this, several other objects were observed, and these results are shown in Figure 5.14

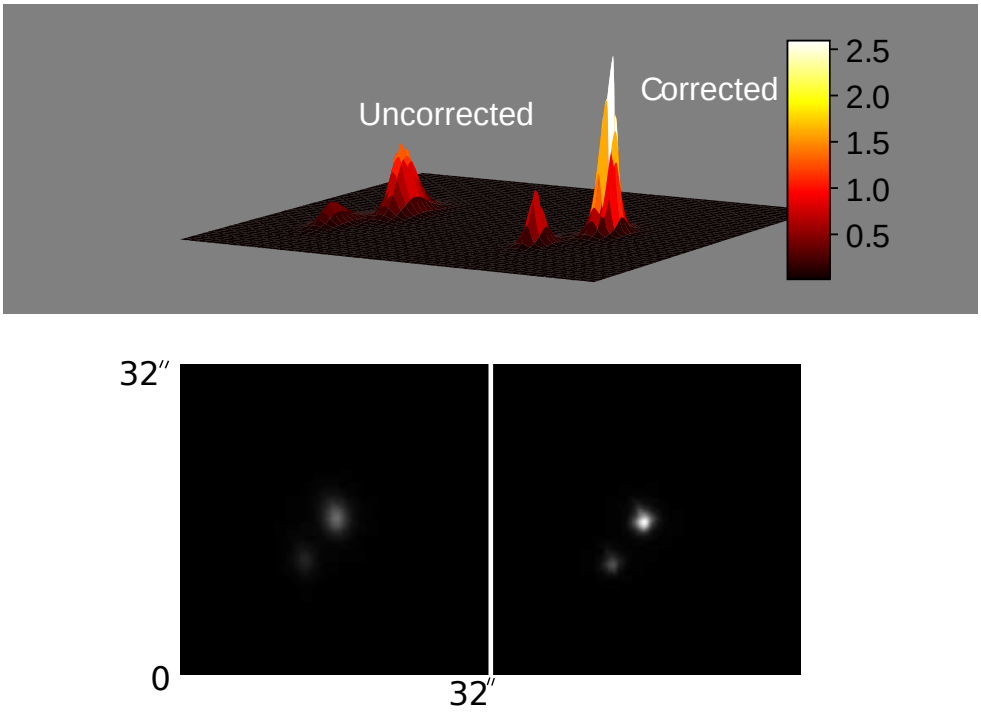

Figure 5.13: Surface plot of HIP50583, containing average tilt uncorrected and corrected image. The frame size is $\sim 32'' \times 32''$.

and Table 5.1.

5.3 Summary and conclusion

A tip-tilt instrument has been developed for the 1.3 m JCB telescope to overcome the image degradation caused by angle of arrival fluctuations. The on-sky performance of the instrument was analyzed by observing several stars of varying brightness and angular separation. The real-time correction has shown a characteristic improvement in the image quality that is consistent with previously reported studies in the literature. This study has led to the following findings and conclusions:

1. On telescope, the rms image motion was reduced by ∼14 times, and the correction bandwidth was estimated to be about 0.1 times the loop frequency, where the loop frequency was varied from 47 Hz to 290 Hz

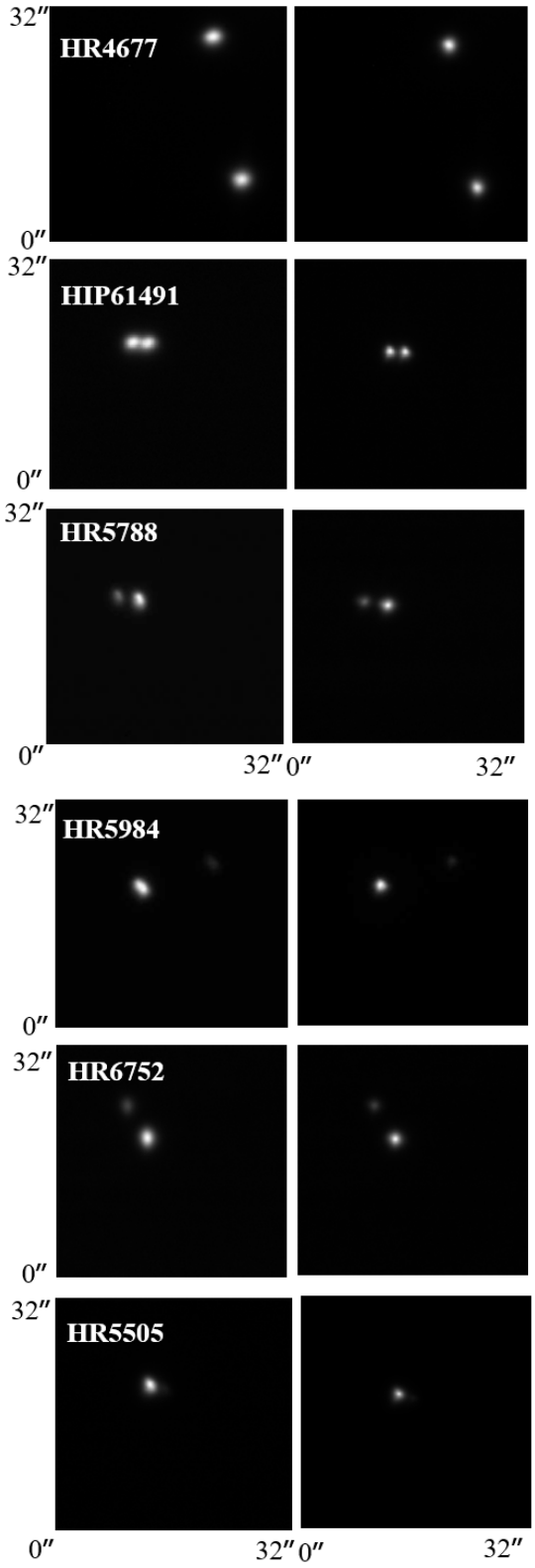

Figure 5.14: Examples: Tilt uncorrected (left column) and corrected (right column) images of various targets.

Table 5.1: List of observed stars with varying angular separation. In the table, m_v is apparent magnitude, Δm_v is magnitude different between two objects and 'Sep' is angular separation between the objects in arc-sec. Peak factor is the ratio of tilt corrected and uncorrected image and improvement in resolution (R) is similar to Equation 5.1. LF is approximate loop frequency

Sl.No.	Target	RA	Dec	m_v	Δm_v	Sep($''$)	LF (fps)	Peak factor	R(%)
1	HIP57632,–	11 49 03.5	+14 34 19.4	2.13	–	–	290	2.8,–	57,–
2	HIP54879,–	11 14 14.4	+15 25 46.4	3.35	–	–	290	2.1,–	45,–
3	HIP37279,–	07 39 18.1	+05 13 29.9	0.37	–	–	290	1.8,–	44,–
4	HIP65474,–	13 25 11.5	-11 09 40.7	0.97	–	–	290	1.4,–	32,–
5	HIP67927,–	13 54 41.0	+18 23 51.7	2.68	–	–	290	1.5,–	38,–
6	HIP69673,–	14 15 39.6	+19 10 56.6	-0.05	–	–	290	2.4,–	50,–
7	HIP50583, gam02 Leo	10 19 58	19 50 29.3	2.37	1.1	4.63	290	2.5, 2.1	52, 46
8	HIP61941, gam Vir B	12 41 39.6	-01 26 57.7	2.74	0.75	1.52	290	2.4, 2.3	51, 49
9	HR4677, HD 106976	12 18 08	-03 57 05.01	5.99	0.7	20.33	64	1.5, 1.3	36, 32
10	HR6752, 70 Oph B	18 05 27	02 30 0.0	4.03	2.04	4.91	98	1.9, 1.7	41,36
11	HR5789, del Ser B	15 34 48.1	10 32 15.9	3.79	1.4	4.1	98	1.7, 1.5	32, 33
12	HR5984, bet02 Sco	16 05 26.2	-19 48 19.6	2.5	2.3	13.64	98	1.8, 1.6	42, 36
13	HR5505, eps Boo B	14 44 59.2	+27 04 27.2	2.39	2.4	2.58	98	1.8, 1.5	43, 31

(five distinct frequencies in this range).

2. The FWHM of the image reduced from 2.4″ to 1.03″. It corresponds to 57% improvement in the image resolution.

3. The sensitivity of the instrument was found to increase by a factor of 1.1 magnitudes (corresponding to the increase in the dynamic range, peak intensity ratio of 2.8).

4. In the case of targets with two close-by stars in the field, the FWHM of the individual PSF decreased, and the peak brightness increased depending on the magnitudes. For example, in the case of HIP50583 with separation of 4.63″ and magnitude difference of 1.1, the FWHM of the bright star increased by 52%, and that of the faint star increased by 46%. The peak brightness of the bright star increased by a factor of ~ 2.5, and that of the faint star increased by a factor of ~ 2.1.

In the next chapter, the thesis is summarized, and present prospects on adaptive optics system development are discussed.

Chapter 6

Conclusion

As a part of AO development program, the tip-tilt adaptive optics system was designed developed and tested for its performance on 1.3 m telescope at Vainu Bappu Observatory (VBO). The thesis consists of, the measurement of turbulence parameters, design and development of the tip-tilt adaptive optics system, and on-sky test of the instrument on 1.3 m JCB telescope, VBO. An instrument control software was designed along with a user interface. The performance of the instrument was evaluated initially in the laboratory and finally on the telescope. Thus, the objective of this thesis has been fulfilled. In this chapter, the thesis is summarized, and future prospects are discussed.

6.1 Thesis summary

The project of adaptive optics system was driven by the necessity for improving the performance of the existing astronomical telescopes and acquiring the capacity to develop such systems for upcoming National Large Solar telescope and National Large Optical telescopes in India. The development of the tip-tilt adaptive optics system is part of achieving in-house adaptive optics capabilities at IIA. We fulfilled this objective by designing, developing and demonstrating the tip-tilt instrument successfully on the telescope.

For a holistic understanding of adaptive optics, we have started with the understanding the causes of the wavefront distortions and its quantification, i.e. by measuring the atmospheric turbulence parameters by using short exposure images acquired by the telescope. We also summarised the design parameters of the AO system that were based on the measured turbulence parameters. The instrument was developed and tested on several pairs of stars, and it has significantly improved the angular resolution of the images, and its performance is on par with similar systems existing elsewhere.

The thesis is summarised as follows.

- The turbulence parameters for the design and development of an adaptive optics system have been successfully measured using short exposure images. The on-site measurement of such parameters gives more reliable input for designing the adaptive optics system. The measured turbulence parameters, median atmospheric seeing, tilt-anisoplanatism and coherence time are 1.85″, 36″ and 2.4 ms, respectively. It was estimated that for a full-fledged adaptive optics system with moderate Strehl, a deformable mirror with 180 to 200 actuators would be required. For optimal performance, the instrument needs to work with a loop frequency of 400-600 Hz. It was found that the faint star should be within 36″ so that at least the tilt component of the wavefront can be corrected effectively.

- The concept of tip-tilt adaptive optics system was successfully tested in the laboratory using induced image motion. In the laboratory, we artificially produced image motion using two different mechanisms. In the first case, the wedged glass plate with hot air blower produced a periodic image motion. The tip-tilt correction has reduced the *rms* image motion by a factor of 5.3. The power spectrum of image centroids has shown a correction bandwidth of $\sim$ 6.4 Hz. In the second case, we induced image motion by using image centroid data obtained from the telescope. The tip-tilt correction has reduced the image motion by a

factor of up to 14 times. The power spectrum has shown a correction bandwidth of $\sim$ 25 Hz.

- An optical system of the tip-tilt instrument was designed using ZEMAX ray-tracing software. The design was optimized to achieve a pixel resolution close to the diffraction limit of the telescope. The imaging arm of the instrument has a diffraction-limited FoV of $1'$. Over 90% of the geometrical energy was confined within a circle of 35 μm diameter. Based on these specifications, the optical design of the instrument was qualified to be sufficient enough to go ahead with the implementation (manufacturing, integration and demonstration).

- An instrument interface unit was designed and developed in AutoCAD to house all the sub-components. The provisions to place all the elements on the base plate were carefully designed based on the optical design. The fabricated instrument was qualified to be integrated with the telescope.

- A tip-tilt control software with a graphical user interface has been developed in LabView. This software coordinates between the til-tilt controller and image motion sensor. A software module was designed to calibrate the axis alignment and its step size. A rotation matrix was generated to minimize the effect of axis misalignment. The control software was developed by incorporating a master loop and a slave loop. The farmer will acquire images continuously, and the later will measure the shift in the image motion and enable the tip-tilt stage for correction. This mechanism helped in improving the frequency of the control loop.

- The instrument was successfully interfaced with the telescope. It was tested on several targets to evaluate its performance. It was checked for *rms* image motion reduction, correction bandwidth and the improvement in FWHM of point-spread-function. On telescope, the *rms*

image motion reduced by a factor of 14, the correction bandwidth was measured $\sim$ 26 Hz, and the FWHM was improved up to $\sim$ 57% at a closed-loop frequency of 290 Hz. The FWHM of the image reduced from 2.4″ to 1.03″.

- The sensitivity of the instrument was found to increase by a factor of 1.1 magnitudes (corresponding to the increase in the dynamic range, peak intensity ratio of 2.8).

- In the case of targets with two close-by stars in the field, the FWHM of the individual point-spread-function decreased, and the peak brightness increased depending on the magnitudes. For example, in the case of HIP50583 with separation of 4.63″ and magnitude difference of 1.1, the FWHM of the bright star increased by 52%, and that of the faint star increased by 46%. The peak brightness of the bright star increased by a factor of $\sim$ 2.5, and that of the faint star increased by a factor of $\sim$ 2.1.

This thesis involves the measurement of turbulence parameters, design development and demonstration of tip-tilt image motion compensation system for stellar imaging. For the first time, a tip-tilt instrument has been designed and developed in IIA and demonstrated on a stellar telescope in India. The instrument performance is in good agreement with results obtained elsewhere. Measurement of atmospheric turbulence parameters namely, r_0, tilt an-isoplanatism and coherence time using short exposure time images of stellar objects is rare. Estimation of coherence time using Gerchberg-Saxton algorithm is distinct. The measured turbulence parameters were carefully considered for the design, development of the instrument and during the characterization of the instrument on telescope. Thus this thesis covers end-to-end procedure starting from instrument design requirements and development to its demonstration on a telescope.

To further improve the image quality to a near-diffraction-limited resolution of the telescope, the work on a high-order AO system is required.

6.2 Future Work

After achieving satisfactory results in the first stage of the AO project, next logical step would be to build a full-fledged AO system for the telescope. In this thesis the initial focus was on understanding the contribution of spatial sampling for wavefront sensing and correction at different seeing conditions. Towards this, a simulation exercise is undergoing using Python programming language. It gives an insight into the effect of various parameters on the performance of an AO system.

As a small extension of current work, I have also worked out a preliminary high-order AO design for 1.3m telescope using ZEMAX ray-tracing software. Though not the main focus of this thesis work, the higher order AO design is included in Appendix B for future reference. This design should be evaluated by experts. With suitable modifications it could be a good starting point for next level of AO technology demonstration. Details of the design are separately given in the Appendix B.

Before laboratory demonstration, the sub-components namely deformable mirror, phase screen have been calibrated for their performance by using *Zygo* interferometer. This calibration gave insights into the spatial distortions that can be induced and the limitations over the deformable mirror that can correct the wavefront. A control software was developed on LabView platform.

In the laboratory, a point source was generated by using a laser source in combination with a spatial filter. The wavefront distortions were created using the *Lexitek* phase screen. The light passing through this screen gets distorted. The distorted wavefront was sensed using a Shack-Hartmann wavefront sensor, and corrected using the deformable mirror. Initial efforts were carried out towards demonstration closed-loop AO correction. The results have shown a $\sim 37\%$ reduction in *rms* wavefront error. Experiments need to be conducted to improve the correction of the distorted wavefront in real-time. It can be done by carefully characterizing the distortions induced by

the phase screen and developing a suitable optical system for sensing them. From this, it is expected to improve the amount of correction. After achieving the desired performance of the high order AO system in the second stage, it is destined to test its performance on the telescope.

Finally, it is hoped that this thesis work will provide impetus to the future development on higher order AO at IIA.

Chapter A

Appendix: Control software

A.1 Control software

The tip-tilt control software was developed using LabView platform. It controls, the *Physik Instrumente* (PI) tip-tilt stage, *Andor Neo sCMOS* camera and tip-tilt correction operation. The software was developed by utilizing the libraries of PI, Andor SDK 3.0 and various tools of LabView. The software was developed in modules and then they are stacked as a sequence of frames. Each frame has several LabView palette function. The functionality of each palette is similar to their respective libraries. I will present all frames starting from initializing the program till stopping the program.

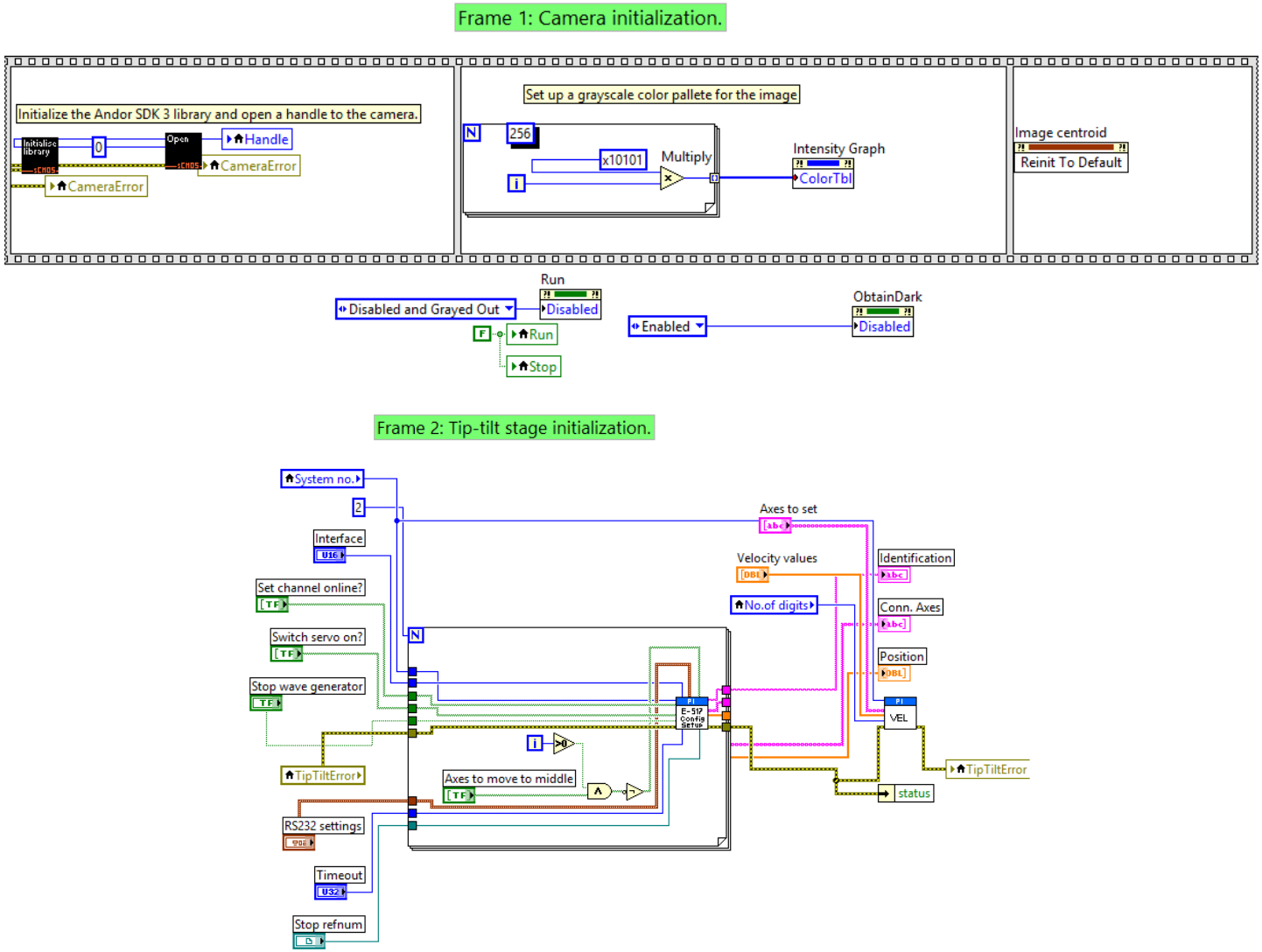

Figure A.1: Initialization of camera and tip-tilt stage.

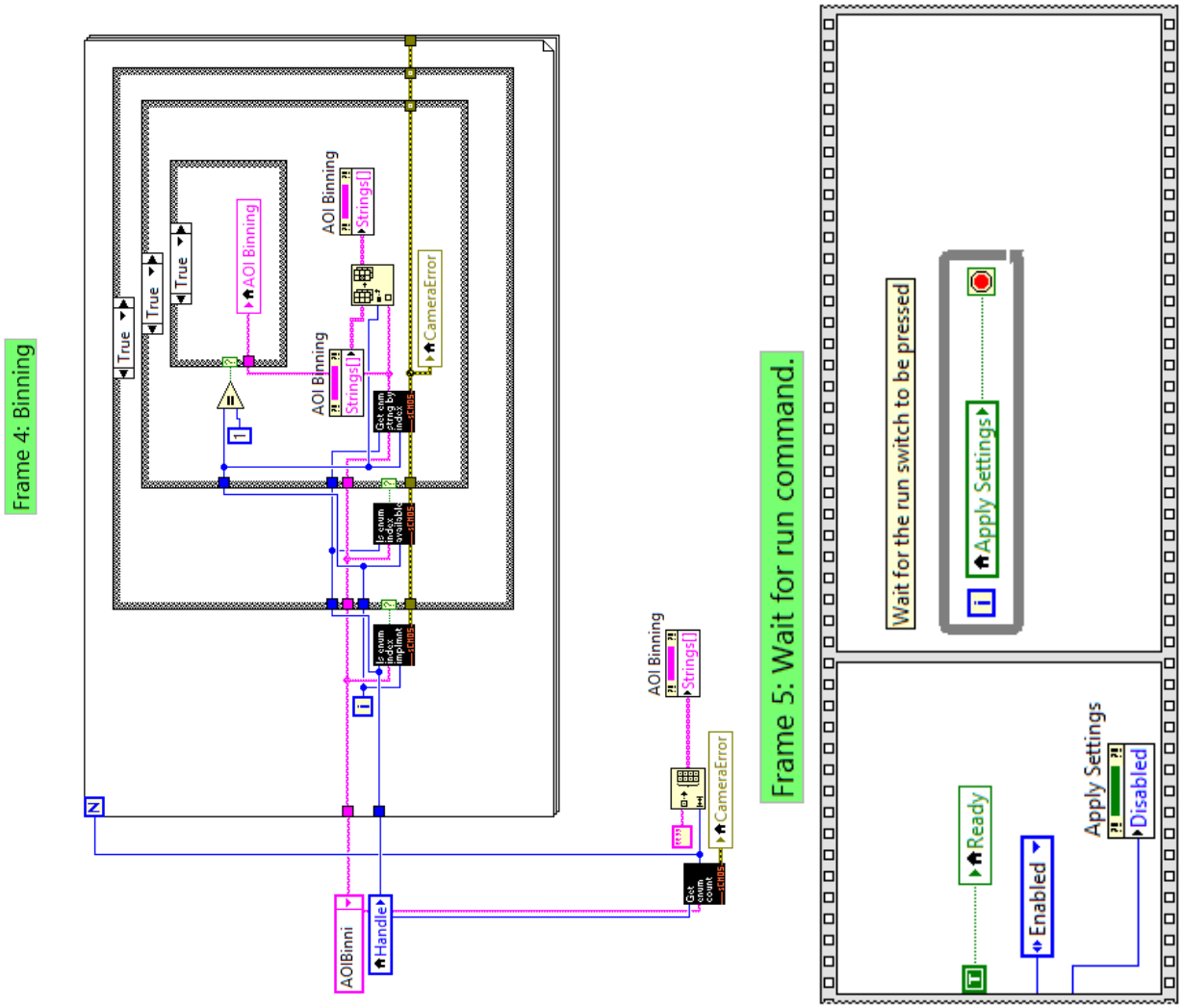

Figure A.2: Set Binning, wait for run command from user to apply settings.

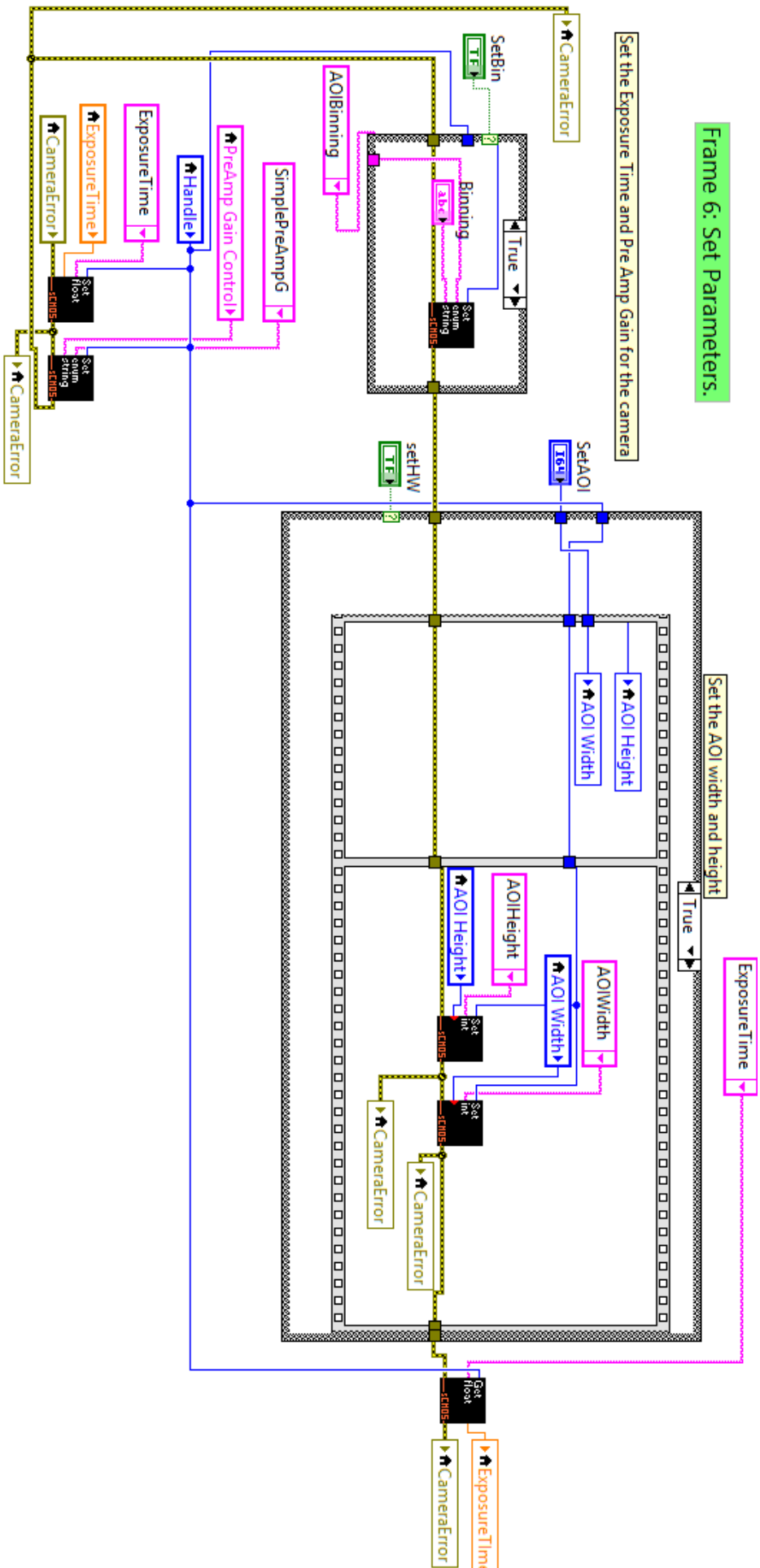

Figure A.3: Set area of interest for acquisition.

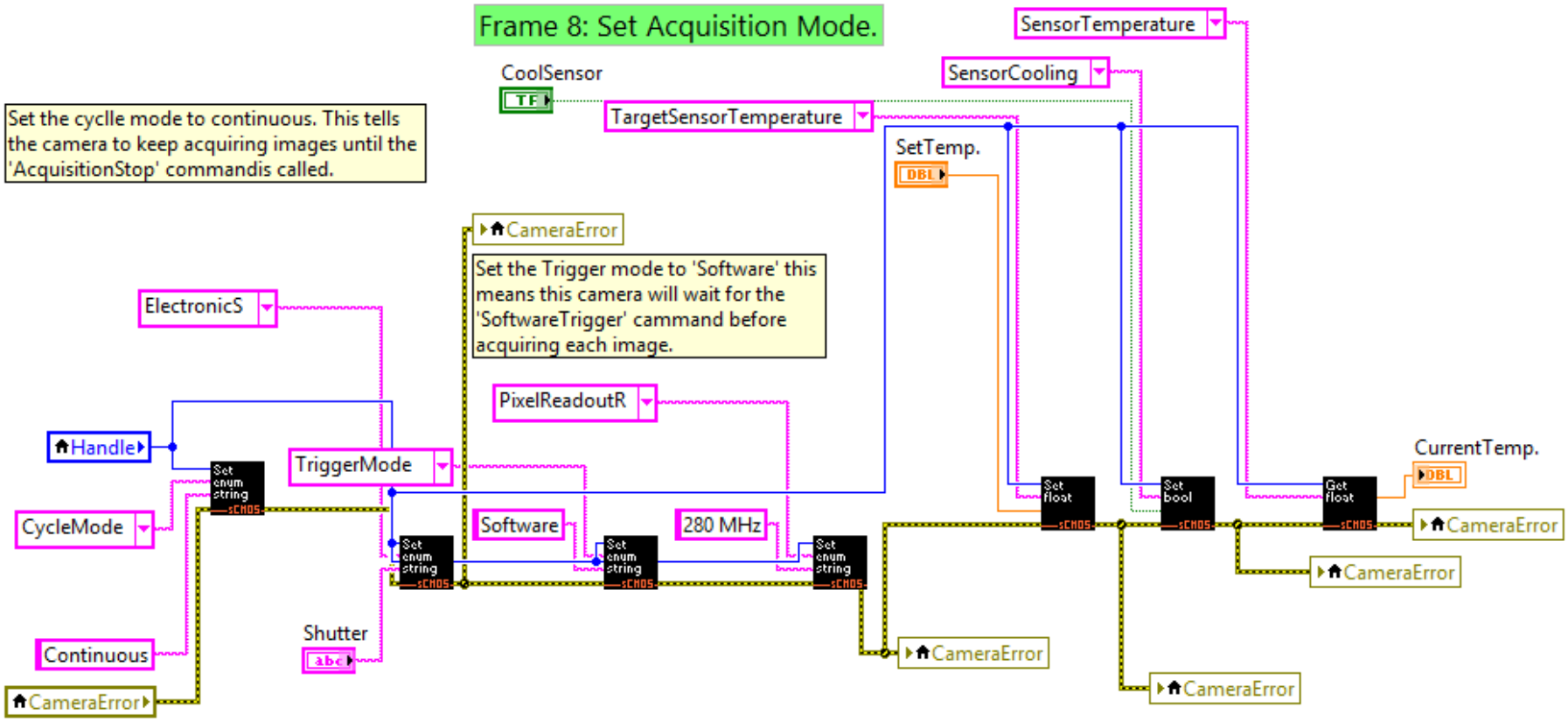

Figure A.4: Set acquisition type: Either rolling or global shutter type, readout rate (280 Hz), trigger type (software) and find the sensor temperature and exposure time etc.

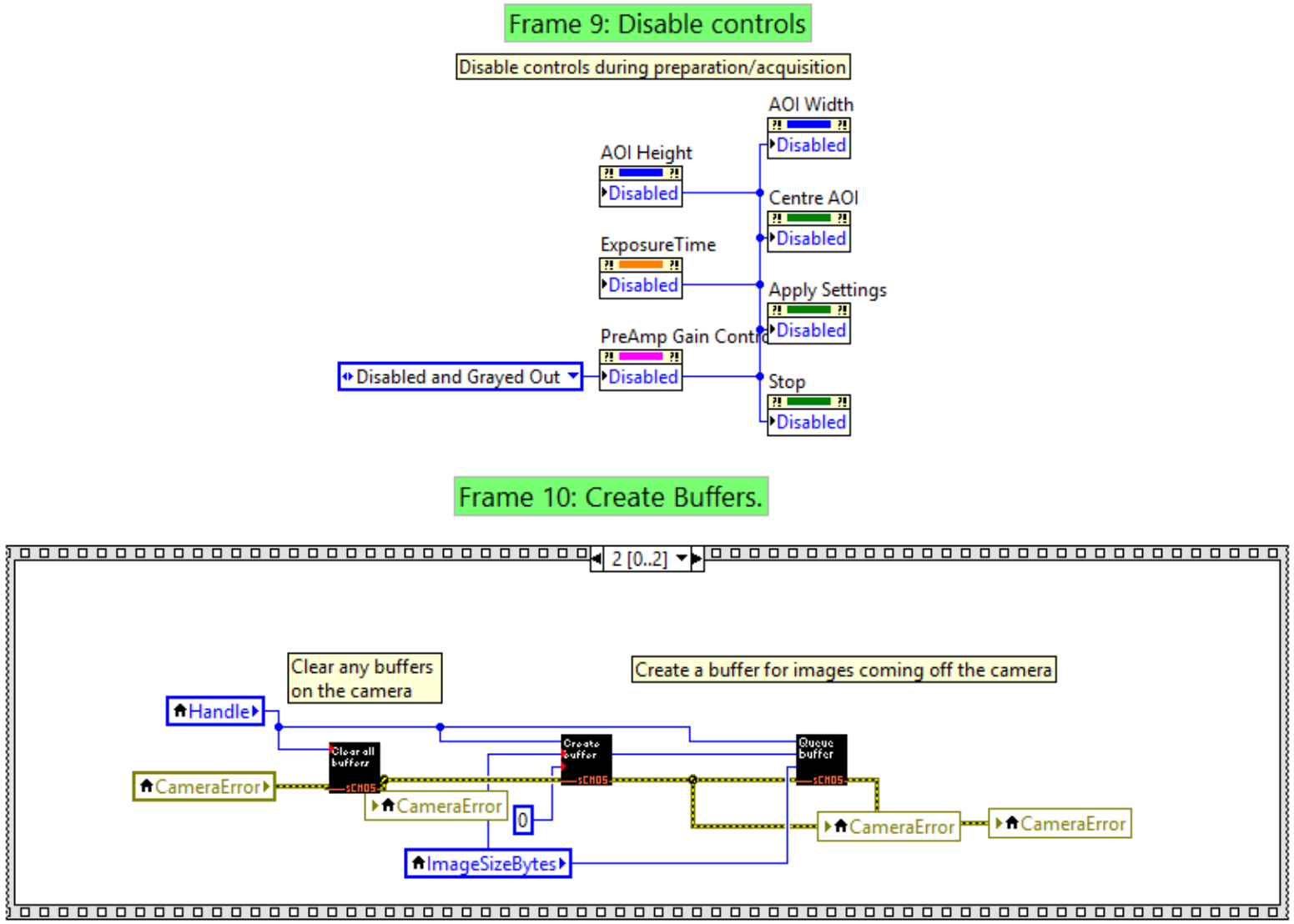

Figure A.5: Disable settings. This will avoid the conflict of multiple user inputs. Create buffer to temporarily save data which can be readout subsequently.

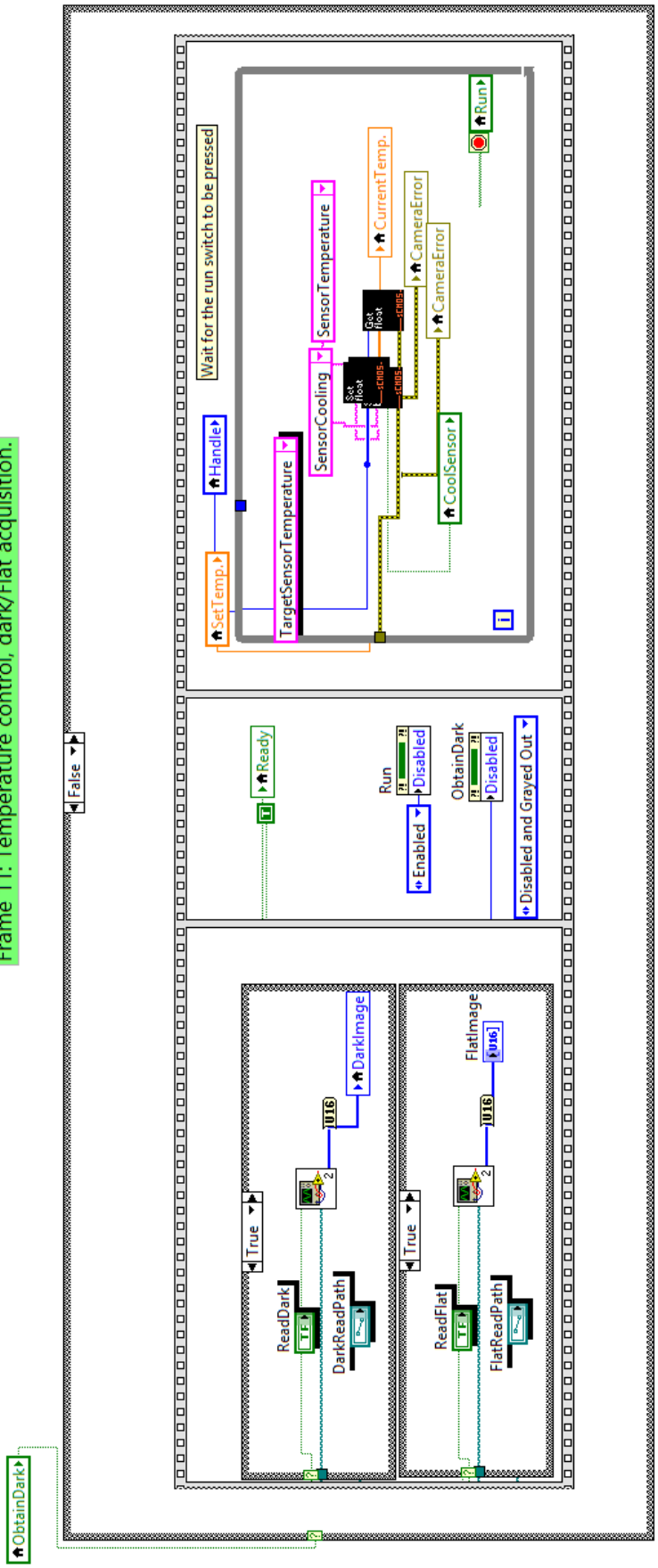

Figure A.6: Set sensor temperature to cool down. and user can set acquisition for dark/ flat frames.

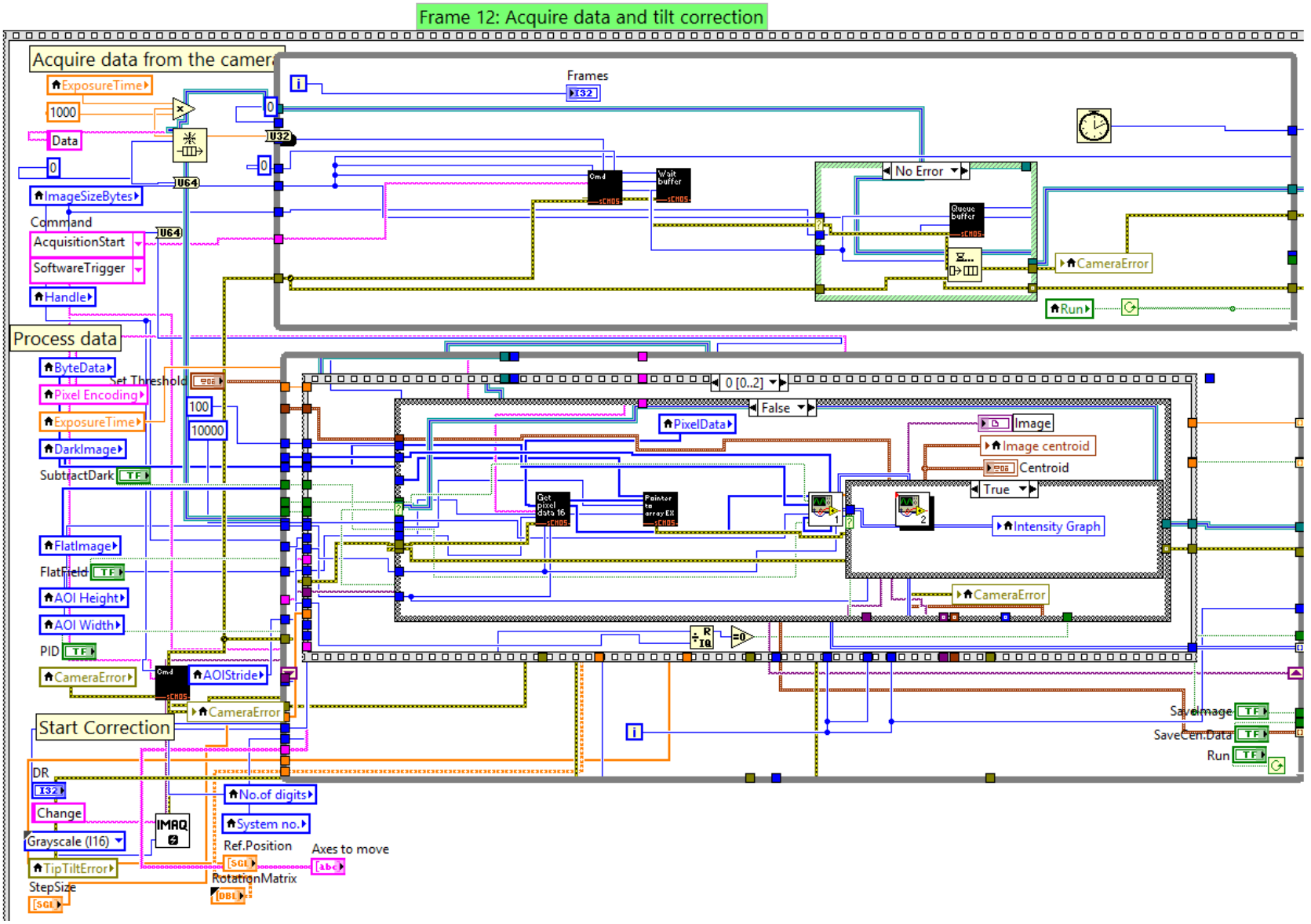

Figure A.7: The tip-tilt control operation. It has, two while loops of operation. The image acquisition loop continuously acquire the data. The second loop actively look for image data and process the image to measure centroid shift and apply correction to the tip-tilt stage. The program can be interrupted at any time during the operation by pressing 'Run' button

Figure A.8: Re-enable the user inputs

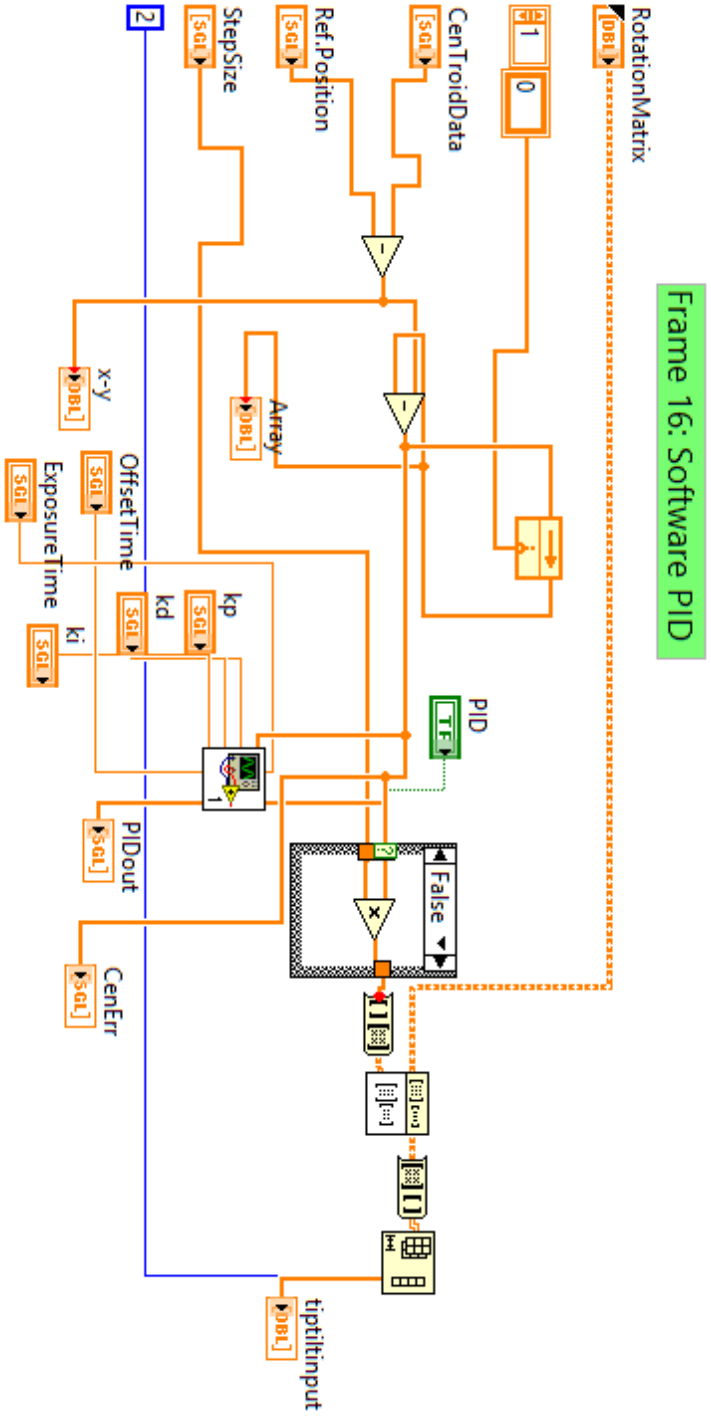

Figure A.9: Software PID control operation

Chapter B

Appendix: Optical system design of AO system

As discussed earlier in Introduction, adaptive optics development program at IIA was planned in three stages. As part of this plan, stage I and stage II were accomplished. In stage I, atmospheric turbulence parameters were measured on-site of the telescope using short exposure images. The essential input parameters similar to spatial sampling for sensing and correction of the wavefront and the loop frequency of the AO system were estimated. In stage II, a tip-tilt image motion compensation system was designed, developed and demonstrated on 1.3 m telescope at VBO. The work-related to development of natural guide star high-order AO system (also includes the tip-tilt system) under stage III is under progress. In this regard, an optical system was designed for 1.3 m JCB telescope. The design also has provision for tip-tilt correction optics that is essential to correct the global tilt of the wavefront before the high order correction.

B.1 Design of AO system

A natural guide star (NGS) AO is designed to be located at the Cassegrain focus of the telescope. Figure B.1 shows the AO design for the telescope. The instrument was designed for the West port (Figure 3.1) of the telescope. In the design, L1 collimates the $F/_{\#}$ beam of the telescope and directs it to the deformable mirror located at the pupil plane. The relay optics in the image plane beam path was designed to improve the $F/_{\#}$ to 19.4 to sample the image plane adequately. The wavefront sense plane beam path has $F/_{\#}$ 5.2 at the sense plane. In the following subsections, the optical design of the system is discussed in detail.

B.1.1 Parameters for determining AO design

In this section, we will explain about all the parameters that are essential and require attention to develop an AO system. The design was primarily driven by subsystems, namely, deformable mirror, wavefront sensor (Shack-Hartman sensor). It was also desirable to improve the spatial sampling at the image plane to attain a near-diffraction-limited resolution.

- **deformable mirror (DM)**: It is a thin frame membrane or segmented mirror which can be deformed to compensate for incoming wavefront. The DM membrane is etched with actuators placed in a square grid to push or pull the mirror. The Boston MEMES (Multi-5.5) DM is readily available in laboratory at IIA, which was considered for this design. The DM has a 12×12 electrostatic actuators with 140 active actuators (the four corner actuators are redundant) with 450 μm pitch size and has an aperture size of 4.95 mm.

- **Micro lens array (SH)**: Shack-Hartman sensors were commonly used for wavefront sensing in adaptive optics systems. The sensor has a microlens array for spatially sampling a wavefront. Microlens array

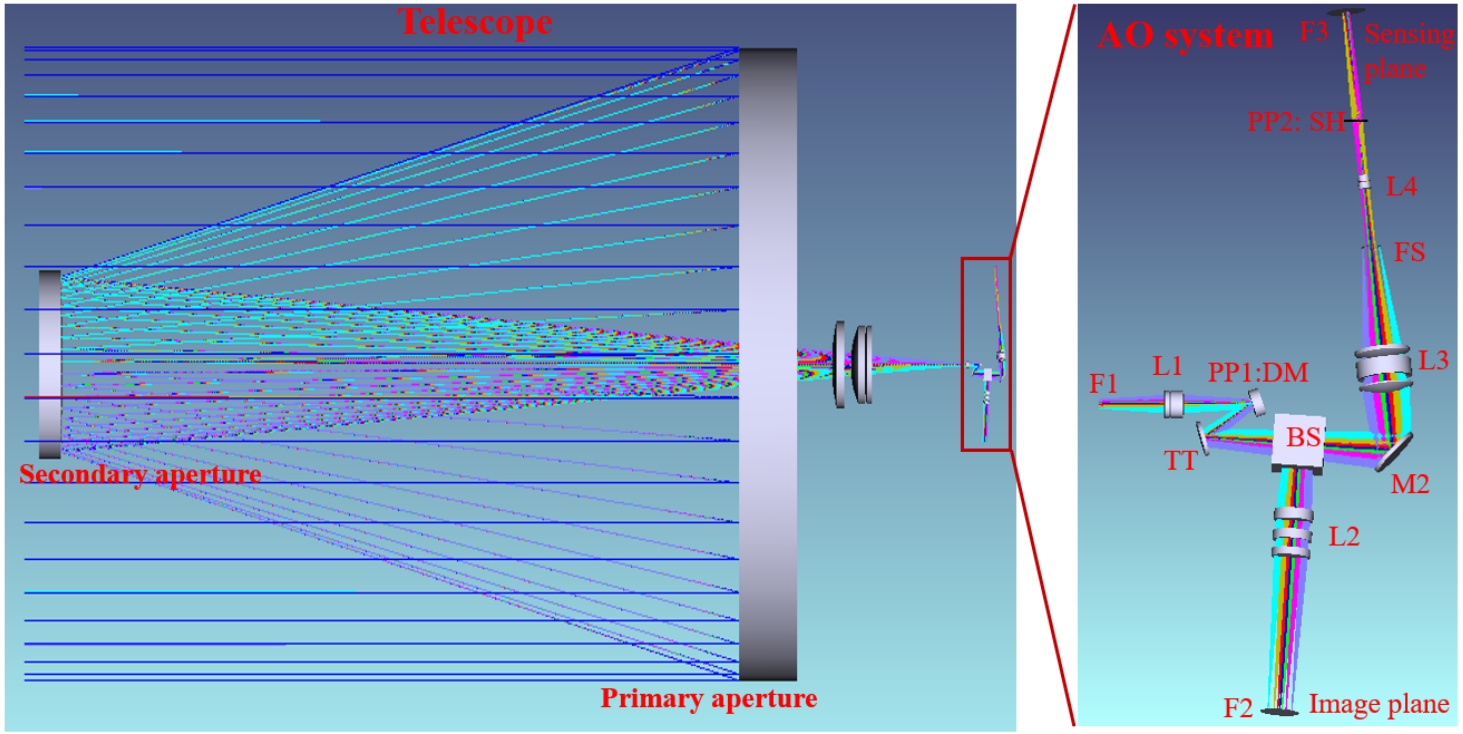

Figure B.1: Optical system design of the instrument. Optical system with the telescope (left) and adaptive optics (AO) system design(right). F1: Telescope focus, L1: Collimating lens, PP1: pupil plane 1, DM: Deformable mirror, TT: Tip-tilt mirror, BS: Beam Splitter, L2: Imaging lens, F2: Image plane, M2: Fold mirror, L3: Imaging lens, FS: Field stop, L4: Collimating lens, PP2: Pupil plane 2, SH: Shock-Hartman micro lens array, F3:SH image plane (sensing plane).

with a pitch size of 500 μm and a focal length of 24 μm was considered for the design. It would cover a $15'' \times 15''$ image field of view (FoV) on sensing camera.

B.1.2 Optical system design

A deformable mirror (DM) and wavefront sensor (WFS) are the principal components to decide on AO system. The DM and the SH determine the size of pupil planes (PP1, PP2). On DM, the pitch area covering the inner grid of 10×10 actuators was chosen for wavefront correction operation. Thus the size of PP1 is 4.5 mm. The L1 optics was designed to obtain a pupil plane size near to this. Similarly, A grid of 10×10 microlens was chosen for the spatial sampling of the wavefront. It determines the size of PP2 as 5 mm. The L4 optics was designed to attain the pupil plane size similar to this. The field stop was designed to allow a field of $\sim 15'' \times 15''$. The image plane of the AO system was designed to obtain a near-diffraction-limited image. At the F1 the image is under-sampled. To improve the spatial sampling, the imaging optics need to be designed to improve the effective focal length of the system. The L2 optics were designed to improve $F/_{\#}$ of 8 to $F/_{\#}$ of 19.4. It will magnify the image to improve the sampling by a factor of ~ 2.5.

The optical system was designed for a wavelength range of 0.55 μm to 1.15 μm with a diffraction-limited field of view of $1.5'$. Approximately 85% of geometric encircled energy is within 25 μm. The spot diagram and geometric encircled energy plots are shown in Figure B.2.

B.1.3 Summary

AO system was designed to be compatible to work with seeing conditions as low as 10 cm of r_0 in the wavelength range of 0.55 μm to 1.15 μm. We have designed WFS for FoV of $15'' \times 15''$. This is because it could be easy to select and place guide star in the field for sensing. In the wavefront sensor, each sub-aperture was estimated to occupy 20×20 pixels ($\sim 25\mu$m) array on

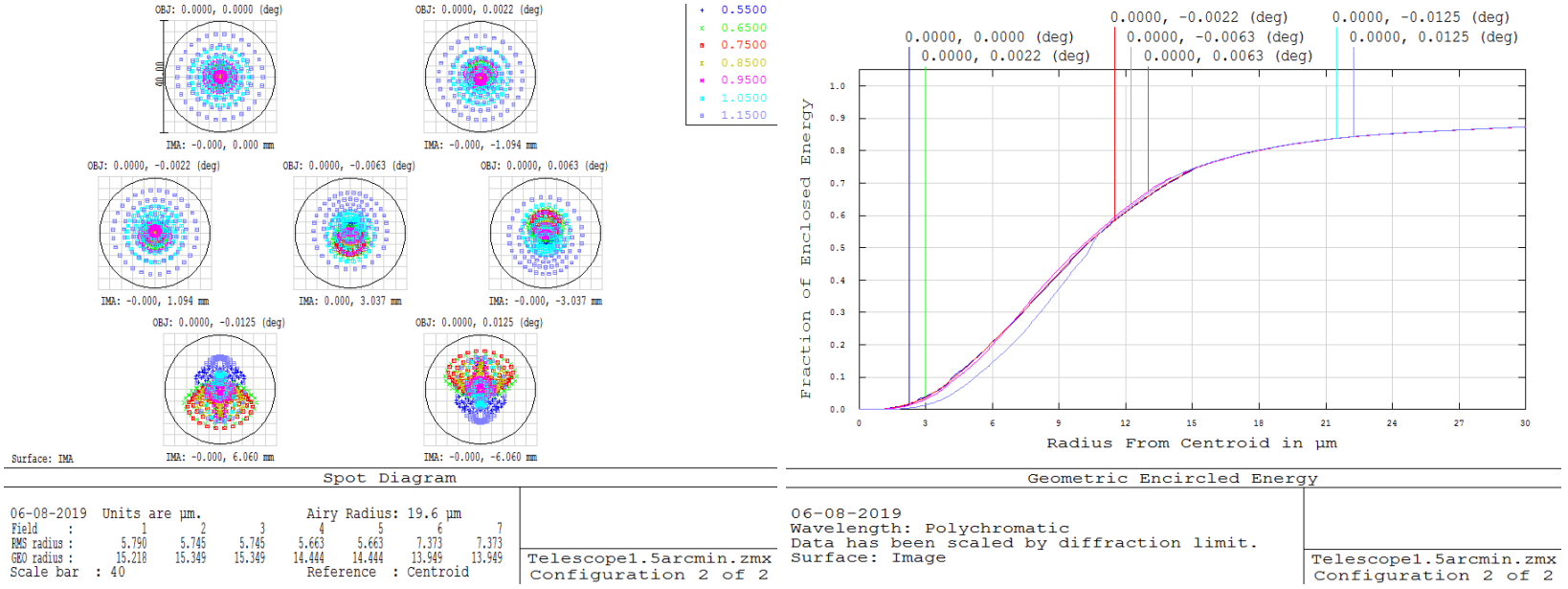

Figure B.2: Spot diagram (left). The diffraction ring with airy radius of 19.6 μm is shown in black colour. The geometric encircled energy diagram (right). Approximately, 85% enclosed energy is within 25 μm.

sensing camera. The readout time and the computation time to reconstruct the wavefront increases with high pixel sampling. But, if the sampling is reduced, results in the poor estimation of the wavefront. So, there must be a trade-off between the pixel array size and pixel scale.

This is a preliminary design of the AO system. The design can be further improved to get qualified to implement on the telescope.

Bibliography

H. W. Babcock. "The possibility of compensating astronomical seeing". *Publications of the Astronomical Society of the Pacific*, 65(386):229–236, 1953. 4

R. Barakat and P. Nisenson. "Influence of the wave-front correlation function and deterministic wave-front aberrations on the speckle image-reconstruction problem in the high-light-level regime". *JOSA*, 71(11):1390–1402, 1981. 17

A. Bayanna, B. Kumar, R. Louis, P. Venkatakrishnan, and S. Mathew. "Development of a low-order Adaptive Optics system at Udaipur Solar Observatory". *Journal of Astrophysics and Astronomy*, 29(1-2):353–357, 2008. 9

J. M. Beckers. "Increasing the size of the isoplanatic patch with multiconjugate adaptive optics". In *European Southern Observatory Conference and Workshop Proceedings*, volume 30, page 693, 1988. 5

M. S. Belen'kii, S. J. Karis, J. M. Brown II, and R. Q. Fugate. "Measurements of tilt angular anisoplanatism". In *Adaptive Optics and Applications*, volume 3126, pages 481–487. International Society for Optics and Photonics, 1997. 17

J. B. Breckinridge, editor. *"Amplitude and Intensity Spatial Interferometry II"*, volume 2200, June 1994. 18

D. Buscher, J. Armstrong, C. Hummel, A. Quirrenbach, D. Mozurkewich, K. Johnston, C. Denison, M. Colavita, and M. Shao. "Interferometric seeing measurements on Mt. Wilson: power spectra and outer scales". *Applied optics*, 34(6):1081–1096, 1995. 2

L. Close and D. McCarthy. "High resolution imaging with a tip-tilt Cassegrain secondary". *Publications of the Astronomical Society of the Pacific*, 106 (695):77, 1994. 8, 64, 78

L. M. Close, F. Wildi, M. Lloyd-Hart, G. Brusa, D. Fisher, D. Miller, A. Riccardi, P. Salinari, D. W. McCarthy, and R. Angel. "High-resolution images of orbital motion in the trapezium cluster: First scientific results from the multiple mirror telescope deformable secondary mirror adaptive optics system". *The Astrophysical Journal*, 599(1):537, 2003. xiii, 5, 6

R. Conan, A. Ziad, J. Borgnino, F. Martin, and A. A. Tokovinin. "Measurements of the wavefront outer scale at Paranal: influence of this parameter in interferometry". In *Interferometry in optical astronomy*, volume 4006, pages 963–973. International Society for Optics and Photonics, 2000. 2

J. C. Dainty, A. V. Koryabin, and A. V. Kudryashov. "Low-order adaptive deformable mirror". *Applied optics*, 37(21):4663–4668, 1998. 7

J. Davis and W. Tango. "Measurement of the Atmospheric Coherence Time". *Pub. Astron. Soc. Pac.*, 108:456, May 1996. doi: 10.1086/133747. 18

J. Davis, P. Lawson, A. Booth, W. Tango, and E. Thorvaldson. "Atmospheric path variations for baselines up to 80m measured with the Sydney University Stellar Interferometer". *Monthly Notices of the Royal Astronomical Society*, 273(1):L53–L58, 1995. 2

D. L. Fried. "Statistics of a Geometric Representation of Wavefront Distortion". *J. Opt. Soc. Am. A*, 55:1427–1431, Nov. 1965. 2, 7, 16

D. L. Fried. "Optical Resolution Through a Randomly Inhomogeneous Medium for Very Long and Very Short Exposures". *J. Opt. Soc. Am. A*, 56:1372, Oct. 1966. 2, 16, 26

D. L. Fried. "Differential angle of arrival - Theory, evaluation, and measurement feasibility". *Radio Science*, 10:71–76, Jan. 1975. doi: 10.1029/RS010i001p00071. 16

R. Q. Fugate, B. Ellerbroek, C. Higgins, M. Jelonek, W. Lange, A. Slavin, W. Wild, D. Winker, J. Wynia, and Spinhirne. "Two generations of laser-guide-star adaptive-optics experiments at the Starfire Optical Range". *JOSA A*, 11(1):310–324, 1994. 5

J. Ge, J. R. P. Angel, and J. C. Shelton. "Optical spectroscopy with a near-single-mode fiber-feed and adaptive optics". In *Optical astronomical instrumentation*, volume 3355, pages 253–263. International Society for Optics and Photonics, 1998. 6

R. W. Gerchberg and W. O. Saxton. "Practical algorithm for determination of phase from image and diffraction plane pictures". *OPTIK*, 35:237–&, 1972. ISSN 0030-4026. 35

A. Glindemann. "Relevant Parameters for Tip-Tilt Systems of Large Telescopes". *Publications of the Astronomical Society of the Pacific*, 109(736): 682, 1997. 8, 78

A. Glindemann, M. J. McCaughrean, S. Hippler, C. Birk, K. Wagner, and R.-R. Rohloff. "CHARM-A Tip-Tilt Tertiary System for the Calar Alto 3.5 m Telescope". *Publications of the Astronomical Society of the Pacific*, 109(736):688, 1997. 77

D. Golimowski, M. Clampin, S. Durrance, and R. Barkhouser. "High-resolution ground-based coronagraphy using image-motion compensation". *Applied optics*, 31(22):4405–4416, 1992. 7, 8, 64, 78

P. Goode, H. Wang, W. Marquette, and C. Denker. "Measuring Seeing from Solar Scintillometry and the Spectral Ratio Technique". *Solar Physics*, 195 (2):421–431, Aug. 2000. ISSN 1573-093X. doi: 10.1023/A:1005285314970. 29, 30

D. P. Greenwood. "Bandwidth specification for adaptive optics systems". *JOSA*, 67(3):390–393, 1977. 4

J. W. Hardy. *"Adaptive Optics for Astronomical Telescopes"*. Oxford.Univ.press, July 1998. 3, 17, 38, 73, 89

D. Hoffleit. *"Catalogue of Bright Stars"*. New Haven, Conn.: Yale Univ., 1964, 3rd rev.ed., 1964. 22

N. Jovanovic, F. Martinache, O. Guyon, C. Clergeon, G. Singh, T. Kudo, V. Garrel, K. Newman, D. Doughty, and J. Lozi. "The Subaru coronagraphic extreme adaptive optics system: enabling high-contrast imaging on solar-system scales". *Publications of the Astronomical Society of the Pacific*, 127(955):890, 2015. 5

I. W. Jung, Y.-A. Peter, E. Carr, J.-S. Wang, and O. Solgaard. "Single-crystal-silicon continuous membrane deformable mirror array for adaptive optics in space-based telescopes". *IEEE Journal of Selected Topics in Quantum Electronics*, 13(2):162–167, 2007. 6

A. Kellerer and A. Tokovinin. "'Atmospheric coherence times in interferometry: definition and measurement'". *Astron. Astrophys.*, 461:775–781, Jan. 2007. doi: 10.1051/0004-6361:20065788. 18

B. Macintosh, J. Graham, D. Palmer, R. Doyon, D. Gavel, J. Larkin, B. Oppenheimer, L. Saddlemyer, J. K. Wallace, and B. Bauman. "Adaptive optics for direct detection of extrasolar planets: the Gemini Planet Imager". *Comptes Rendus Physique*, 8(3-4):365–373, 2007. 7

H. M. Martin. "Image motion as a measure of seeing quality". *Pub. Astron. Soc. Pac.*, 99:1360–1370, Dec. 1987. doi: 10.1086/132126. 18, 27, 78

R. D. McClure, J. M. Fletcher, J. Arnaud, J.-L. Nieto, and R. Racine. "A measurement of isoplanatism with the high-resolution camera at the Canada-France-Hawaii Telescope". *Pub. Astron. Soc. Pac.*, 103:570–576, June 1991. doi: 10.1086/132855. 17

R. J. Noll. "Zernike polynomials and atmospheric turbulence". *JOSA*, 66(3): 207–211, 1976. 7

S. S. Olivier and D. T. Gavel. "Tip-tilt compensation for astronomical imaging." *Journal of the Optical Society of America A*, 11:368–378, Jan. 1994. doi: 10.1364/JOSAA.11.000368. 8

J. Paul, H. K. Das, A. N. Ramaprakash, M. P. Burse, P. A. Chordia, K. Chillal, G. Datir, B. Joshi, P. Khodade, and A. Kohok. "Design and development of an adaptive optics system in visible and near-infrared for Inter-University Centre for Astronomy and Astrophysics 2-meter telescope". *Journal of Astronomical Telescopes, Instruments, and Systems*, 5 (3):039002, 2019. 9

A. Quirrenbach. "The effects of atmospheric turbulence on astronomical observations". *A. Extrasolar planets. Saas-Fee Advanced Course*, 31(137):137, 2006. 2, 127

R. Racine and R. D. McClure. "An image stabilization experiment at the Canada-France-Hawaii telescope". *Publications of the Astronomical Society of the Pacific*, 101(642):731, 1989. 77

T. R. Rimmele and J. Marino. "Solar adaptive optics". *Living Reviews in Solar Physics*, 8(1):2, 2011. xiii, 3

F. Roddier. "V the effects of atmospheric turbulence in optical astronomy". In *Progress in optics*, volume 19, pages 281–376. Elsevier, 1981a. 89

F. Roddier. "V the effects of atmospheric turbulence in optical astronomy". In *Progress in optics*, volume 19, pages 281–376. Elsevier, 1981b. 2

M. Roopashree, A. Vyas, and B. R. Prasad. "A review of atmospheric wind speed measurement techniques with Shack Hartmann wavefront imaging sensor in adaptive optics". *Journal of the Indian Institute of Science*, 93 (1):67–84, 2013. 9

G. Rousset, J. Fontanella, P. Kern, P. Gigan, and F. Rigaut. "First diffraction-limited astronomical images with adaptive optics". *Astronomy and Astrophysics*, 230:L29–L32, 1990. 4

C. T. Russell. "Geophysical coordinate transformations". *Cosmic Electrodynamics*, 2(2):184–196, 1971. 67

M. Sarazin and F. Roddier. "The ESO differential image motion monitor". *Astron. Astrophys.*, 227:294–300, Jan. 1990. 16

A. Sivaramakrishnan, R. J. Weymann, and J. W. Beletic. "Measurements of the Angular Correlation of Stellar Centroid Motion". *Astron. J.*, 110:430, July 1995. doi: 10.1086/117533. 17

R. V. Sreekanth, R. K. Banyal, R. Sridharan, and A. Selvaraj. "Measurements of atmospheric turbulence parameters at Vainu Bappu Observatory using short-exposure CCD images". *Research in Astronomy and Astrophysics*, 19 (5):074, may 2019. doi: 10.1088/1674-4527/19/5/74. 10

R. Teoste, J. A. Daley, Jr., R. N. Capes, Jr., J. J. Alves, and M. D. Zimmerman. *"Measurements of tilt anisoplanatism at the Firepond Facility"*. Firepond Facility, Nov. 1988. 17

A. Tokovinin. "From Differential Image Motion to Seeing". *Pub. Astron. Soc. Pac.*, 114:1156–1166, Oct. 2002. doi: 10.1086/342683. 16

R. Tyson. *"Principles of Adaptive Optics"*. Chicago: CRC Press, 1998. ISBN 9780127059020. 3, 38

O. Von der Lühe. "Estimating Fried's parameter from a time series of an arbitrary resolved object imaged through atmospheric turbulence". *Journal*

of the Optical Society of America A, 1:510–519, May 1984. doi: 10.1364/JOSAA.1.000510. 28, 29

A. Vyas, M. Roopashree, and B. R. Prasad. "Dither-based sensor for improved consistency of adaptive optics system". In *Modern Technologies in Space-and Ground-based Telescopes and Instrumentation*, volume 7739, page 773928. International Society for Optics and Photonics, 2010. 9

P. Welch. "The use of fast Fourier transform for the estimation of power spectra: a method based on time averaging over short, modified periodograms". *IEEE Transactions on audio and electroacoustics*, 15(2):70–73, 1967. 65

R. W. Wilson, N. O'Mahony, C. Packham, and M. Azzaro. "The seeing at the William Herschel Telescope". *Mon. Not. Roy. Astron. Soc.*, 309:379–387, Oct. 1999. doi: 10.1046/j.1365-8711.1999.02840.x. 16

X. Yin, X. Li, L. Zhao, and Z. Fang. "Adaptive thresholding and dynamic windowing method for automatic centroid detection of digital Shack-Hartmann wavefront sensor". *Applied Optics*, 48(32):6088–6098, 2009. 25

List of corrections and clarifications

1. Pg vii, Abstract, The 1st sentence of the thesis has a typo to correct

   Typo was corrected.

   Adaptive Optics (AO) technology is a part of ground-based astronomical observatories around the world.

2. Pg 2, 1.1.1, how is the diffraction-limited resolving power of the telescope scales as D^2.

   The reference (Quirrenbach 2006) was given

   The diffraction-limited resolving power (R_{Tel}) of the telescope is proportional to the square of the size (D^2) of primary aperture (Quirrenbach 2006).

3. Pg 5, in the main text the reference to Fig 1.3 is made before the Fig 1.2

   Figures were swapped. After swapping the references are in sequence.

4. Pg 7, 1.2.3: Ambiguous statement: The tilt is dominant among aberration profile of the wavefront.

   The statement was corrected

   The global tilt is dominant among the aberration profile of the wavefront.

5. Pg 15, 1st Para before the introduction is superfluous, contains only generic statements.

   Text was rewritten.

   Atmospheric turbulence parameters namely, atmospheric seeing, the tilt-anisoplanatic angle (θ_0) and the coherence time

(τ_0), randomly change spatially and temporally. These parameters are site-dependent. They determine the specifications of AO systems designed for a telescope. Thus, an adaptive optics design should take into considerations atmospheric conditions measured at observatory site. In this chapter, the methodology used to measure the turbulence parameters at VBO and results obtained are discussed and the importance of these parameters in the design and development of an AO system is described.

6. Pg 16 2nd Para, what is the expression derived by Fried for rms angle-of-arrival fluctuations.

   The following expression was added

$$\langle \alpha^2 \rangle \approx (1.72/\pi^2)(\lambda/D)^{1/3}(\lambda/r_0)^{5/3}, \tag{B.1}$$

7. Pg 36, in the entire chapter r0 was stated in arcsecond ("). For AO design why the units were changed to cm and how the conversion was done?

   The r0 in cm is used to determine the number of actuators of the deformable mirror. As mentioned in the Equation 2.14. The equation is added in the text.

8. Pg 38, you have worked out the design parameters (# actuators, stroke, loop frequency) for higher-order AO. We know for a natural guide star, the AO correction is effective over a narrow field of view 10″. In the context of higher-order AO what is the significance of 36″ tilt-anisoplanatism?

   Tilt-anisoplanatism has significance in tip-tilt image motion compensation systems. The tip-tilt system will be integral

part of high order AO system.

9. Pg 32, the seeing data as shown in Fig. 2.7 is not numbered in a correct date sequence. This needs to be re-plotted.

   The date sequence in Figure 2.7 is corrected.

10. Pg 39, summary point 1 and 3 are ambiguous and needs to be re-written for clarity.

    Summary points were re-written.

    Summary point 1: We have estimated r_0 (alternatively the seeing) from 248 distinct observations spanning over 29 days between April 2015 and April 2017. Short exposure images were used to measure r_0 from angle of arrival fluctuations. We compared the estimated values of seeing from three different methods and found that the values match with 14% uncertainty.

    Summary point 2: The estimated parameters should be considered preliminary, as the values are likely to change with atmospheric conditions at the site. Nevertheless, it helps in fixing the design parameters of the adaptive optics system to be built for this telescope in future.

11. Pg 41, the software should ... correct the image motion in real-time. This is confusing. If the software can correct the image motion then why do we need tip-tilt system?

    The sentence was corrected.

    The software should control the camera to acquire images, measure the shift in image and control the tip-tilt stage to correct the image motion in real-time.

12. Pg 48, the size and focal length of component is given in different units of length (inch and cm). Use only one unit (e.g. cm) consistently

throughout the thesis?

The units were changed to *cm*.

13. Pg 48, explain what is 'master-slave architecture' in LabView? Text is added to explain 'Master-slave architecture'

    The master slave loop architecture is commonly used when two or more processes need to run simultaneously but at different rates. If these processes are run in single loop, the system response gets delayed. The master slave architecture has one master loop and the remaining act as slave loops. The master loop controls all the slave loops.

14. Pg 57, Why pixel binning was at 1st place if is going to impact the PSF sampling?

    The pixel binning is used in case of poor seeing conditions and in case of fainter objects. Even though binning impacts PSF sampling, tip-tilt correction can be applied.

15. Pg 58, Step size: If you are looking for sub-pixel accuracy in image centroid then step size has to be smaller than one pixel. Why was it chosen 1 pixel?

    The estimation of image centroid motion is in sub-pixel. The step size is multiplied with the amount of the centroid shift. This gives sub-pixel motion of image.

16. Pg 61, section 4.1. Again, it is not clear how the software performs the tip-tilt correction in real-time.

    The sentence was corrected.

    the software performs the operation of tip-tilt correction in real-time.

17. Pg 62, 1st Para, last sentence, Thus the output image is expected to stabilize the image motion. How an image can stabilize its own motion? Plz, explain or correct the sentence.

    The sentence was corrected

    The mirror mounted on the tip-tilt stage compensates for the tilts to arrest the image motion. Thus image motion is expected to be stabilized.

18. Pg 63, the bias current is mentioned many times but its value was never quoted. For example, how many dark frames were used for constructing median-dark? Why median and not mean was used?

    The number of dark frames (10 frames) was mentioned in text. The median dark frames are commonly used in this type of applications.

19. Pg 66, The meaning of the acronyms V(CCD), A(TT) etc. shown in Fig 4.3 is not given anywhere. It should be included in the same fig caption.

    The acronyms were included in Fig 4.3 caption.

    Alignment of tip-tilt stage axis with sensing camera axis. V(CCD) and H(CCD) are vertical and horizontal axis of camera, similarly, A(TT) and B(TT) are vertical and horizontal axis of tip-tilt stage. Here, θ is the misalignment angle. With careful calibration for alignment, the value of θ can be made negligible.

20. Pg 67, Fig 4.4 has top and bottom panels. It is not clear what is plotted in the bottom panel.

    The Fig 4.4 caption was edited

    Calibration curves for two-axis tip-tilt stage. The horizontal (H-axis), vertical (V-axis) have been moved with equal step

size of 1 V (top). The error in actuator movement for the fixed input voltage step size (1 V) is mentioned in bottom panel. In both axes, the rms deviation from the linear fit is $\sim$ 0.3 μm.

21. Pg 69, Fig 4.5, the y-axis is labelled the same 'vertical (micron)' for top and bottom panels of the figure. One of them should be 'horizontal'.

    The label, 'horizontal' was added to the Fig 4.5.

22. Pg 70-73, please define clearly the terms: frame-rate, loop-frequency and closed-loop bandwidth. At couple of places, these terms are used interchangeably and thus creating confusion.

    The terms, frame-rate, loop-frequency and closed-loop bandwidth are defined in text.

    The term frame-rate is defined in Pg 43

    Frame rate is the frequency of image frames of an object are acquired and readout by the camera.

    The term loop frequency is defined in Pg 37

    At loop frequency (LF) the wavefront correction process is executed in closed loop. This includes the processes of image acquisition, image processing and correction.

    The term closed-llop bandwidth is defined in Pg 16

    The closed loop bandwidth of a system is the frequency band of operation of a closed loop control system.

23. Pg 70, 72, Fig 4.6 and Fig. 4.8, where is the 0 dB point on the y-axis scale and how was it calculated.

    The 0 dB was defined in the text.

    The 0 dB is estimated by taking the ratio of PSD of the tilt uncorrected and corrected image centroid motion. At 0 dB, the PSD of image centroid motions are equal.

24. Pg 73, Fig.4.9, The data has three legends: *uncorr*, *No_PID* and *PID_corr*. What is the meaning of no PID correction (blue dots)? How can you make the correction without any feedback loop which does not have PID? Plz, clarify in the figure caption or in the main text.

    The figure caption was edited.

    Lab: Image motion centroid scatter plot. The legends depict only software PID control.In case of *uncorr*, the tip-tilt correction was OFF. In *No_PID* case, the internal PID was ON and in case of *PID_corr* the software PID along with internal PID was ON. The PID control could reduce the *rms* centroid motion by 12%.

25. Pg 81, Fig. 5.4, the plot in the bottom panel shows the horizontal line-cut of the tilt corrected and uncorrected PSF. The total star energy recorded by CCD camera (area under each curve) for a given explore should remain the same for both cases. But the plot clearly shows that the area under the orange curve (tilt corrected PSF) is more than the blue curve (uncorrected). This discrepancy needs to be clearly explained. Also, the y-axis in Fig 5.4 and 5.9 is labelled as mean intensity count. Since these curves are just line cut across PSF, why they are labelled as 'mean intensity count' instead of just 'pixel count'. Make this clarification in the text or in Figure caption itself.

    The area under the curve discrepancy was explained in the text.

    The y-axis in Fig 5.4 and Fig 5.9 depict mean intensity of the pixels in line cut across PSF. The area under the curve is same. In case of blue curve, intensity is distributed in wings. After correction this intensity is pushed towards the core of the PSF.

26. Pg 83, Fig 5.6. It is important to state either in the main text or in

the Figure caption: How many centroid points are there in the scatter plot (# of frames) in the uncorrected and corrected case. What is the name of the object and when (date) was it observed?

The name of the object and the number of centroid points area were added to the Fig. 5.6 caption.

On-sky:Image motion centroid scatter plot of object HIP57632. A total of 15000 centroid data points were plotted for uncorrected and tilt corrected data.

27. Pg 85, Fig 5.8, the y-axis label is missing on the plots shown in the right column.

    In Fig 5.8, the y-axis label 'Vertical' was added in the right column.

28. Pg 86: The term 'loop frequency' was used many times in Chapter 3 and 4. Why the acronym LF was used so late in Chapter 5? Also the term 'loop frequency' was not defined clearly anywhere in the thesis and used differently in different chapter. The ambiguity between loop frequency and frame rate must also be removed in all chapters by clearly stating what each term means.

    Loop frequency and frame rate were defined.

29. Pg 88: Figure 5.11, the correction bandwidth is computed where the PSD of uncorrected and tilt-corrected curves intersect. Clearly, the high-frequency side of PSD where both curves cross is noisier. SO how was this crossing point (marked by the red dashed line) determined from the high-frequency noise?

    The high-frequency side of PSD is noisier. To compute bandwidth, ensemble average of the PSDs were used.

30. Pg 89: Figure 5.12, the figure caption is confusing. The vertical axis shows the ratio of EWuc/EWc and not EWuc and EWc as the caption

seems to suggest.

The Fig. 5.12 caption was corrected.

Comparison of gain in angular resolution between the theoretical and the observed data. In this figure, $\mathbf{EW}_{uc}$ and $\mathbf{EW}_{c}$ are equivalent widths of tilt uncorrected and corrected image.